THE RADIATION RESPONSE OF FOCAL PLANE ARRAYS

By

Christina L. Howe

Dissertation

Submitted to the Faculty of the

Graduate School of Vanderbilt University

in partial fulfillment of the requirements

for the degree of

DOCTOR OF PHILOSOPHY

in

Electrical Engineering

December, 2008

Nashville, Tennessee

Approved:

Professor Robert A. Weller

Professor Robert A. Reed

Professor Daniel M. Fleetwood

Professor Ronald D. Schrimpf

Professor Senta V. Greene

ACKNOWLEDGEMENTS

Many people have played a significant role in my success as a graduate student at Vanderbilt University. I would first like to thank my husband, Josh Howe, for his never-ending support, patience, and encouragement through all of my schooling. Without him I would have never kept my sanity and drive. I also want to thank my parents Wayne and Sue Tincher, my children, Tim, Cheryl, Lance, Angie, Madeline, Makenzie, Savannah, Grandma Long, Grandpa Wayne, Grandma Jackie, Jeff, Sandy, Jake, and Daniel, for their love and support in whatever I do.

I would like to thank my PhD committee, Dr. Robert Weller, Dr. Robert Reed, Dr. Dan Fleetwood, Dr. Ron Schrimpf, and Dr. Vicki Greene, for their support and advice, both professionally and personally, while completing both my masters and dissertation work. Also, thank you to Marcus Mendenhall, Brian Sierawski, Paul Marshall, Cheryl Marshall, John Hubbs, Jonnathan Pellish, and Alan Tipton for their direct support, contributions, and discussion of this work. Thank you to all my professors at Vanderbilt University for their guidance in my academic career. I would also like to thank my friends in the Radiation Effects and Reliability Group for their help, support, and comic relief throughout my graduate school career. I would also like to thank my undergraduate advisor, Dr. Dick Blandford at the University of Evansville, Indiana, for giving me the encouragement and drive to attend graduate school.

Thank you to NASA Electronic Parts and Packaging (NEPP) program and the Defense Threat Reduction Agency (DTRA) Radiation Hardened Microelectronics Program for their financial support of this work. Finally thank you to Vanderbilt

University's Advanced Computing Center for Research and Education (ACCRE) for support of the computational portion of this work.

TABLE OF CONTENTS

Page

Chapter

Appendix

LIST OF TABLES

LIST OF FIGURES

CHAPTER I

INTRODUCTION

Hybrid focal plane arrays (FPAs) are increasingly being used in space applications because of their flexibility in infrared applications, reliability, low cost, high-density resolution, and on-chip signal processing [1]. Hybrid FPAs include an imaging array and read-out circuitry bonded together. FPAs have important applications for satellite missions such as space-borne astronomy, Earth surveillance, star tracking, digital imaging, laser communications, etc. They are often used on satellites planned for long orbits in harsh proton environments requiring exceptional reliability when exposed to radiation. Because of their high sensitivity to noise, FPAs present a unique challenge in radiation hardness.

As new, more demanding space projects are being designed and launched, more stringent requirements are being placed on detector systems [2]. NASA's James Webb Space Telescope (JWST) is a good example of these challenging requirements. Planned for a 5 to 10 year mission, this spacecraft will undergo some of the most extreme environments ever encountered and therefore has extremely tough detector requirements [2]. FPAs and other on-board circuitry must be able to withstand harsh environments for the entire life of the mission. The telescope will incorporate both near-infrared and mid-infrared FPAs.

Transient effects and displacement damage are the two main radiation effects within FPAs. This document focuses on the transient effects in FPAs from protons, the dominant particle to disturb these devices at most orbits since electrons are usually shielded by the spacecraft [3]. The number of protons and their typical energies in the space environment vary greatly with altitude and solar activity. The secondary proton environment also contributes heavily to transients within a FPA. The European Space Agency's Infrared Space Observatory (ISO) reported 80% more transients in their devices than could be accounted for by primary particles [4]. This is described further in Chapter 3.

As an ion traverses a device, its energy is transferred via direct ionization, screened scattering, and nuclear reactions. Electron-hole pairs generated along a particle's track are detected by the readout circuitry of a FPA and can be mistaken as a legitimate signal. Depending on the detector array structure and particle track, neighboring pixels can be affected as well. Radiation effects in FPAs and CCDs are enhanced due to cryogenic operating temperatures. At cryogenic temperatures, electrons become highly mobile while holes become nearly immobile in comparison [5]. The mobility in a semiconductor is dependent on the temperature, material, and doping [6], [7]. FPAs and CCDs are often cooled to cryogenic temperatures to help reduce thermal noise [8].

Materials surrounding the devices must also be considered when predicting FPA response. Secondary particles created by scatters in these materials have a direct impact on the device response, as shown in this document. By understanding how energy is deposited into FPAs, designers can choose the type of device that will best withstand the environment in which it will fly. Through modeling, the behavior of the device on-orbit can be predicted. The implications of characteristics such as size, composition, and operating temperature can be considered before lengthy and expensive fabrication and testing is performed.

Chapter 2 of this dissertation outlines necessary background regarding FPAs and CCDs. Also discussed in this chapter is the natural space environment and radiation effects on these devices including transient effects, displacement damage, and total-ionizing dose. The chapter is concluded with a discussion of energy deposition in solids and the simulation tools used throughout the rest of this document.

The motivation behind this work and a history of FPA modeling is outlined in Chapter 3. Through satellite images, the effects of radiation on imaging devices are evident by degradation of the image produced by an optical detector following a solar event.

Modeling a silicon FPA using a Monte Carlo based simulator is described in Chapter 4. Also shown in this chapter are technology computer aided design (TCAD) simulations used to determine the sensitivity of these devices to the motion of charge between pixels.

Through MRED simulations and the methodology developed in Chapter 4, it is shown that the materials surrounding a silicon diode array have a significant impact on its response in Chapters 5 and 6. It is also shown that direct ionization is the dominant mechanism for energy deposition below 300 keV, while nuclear reactions dominate at higher energies and screened scattering contributes very little. Even though direct ionization is the dominant mechanism, a constant LET and path length calculation alone does not capture the shape of the differential distribution. Finally, chapter 7 will summarize the results and discuss future work.

CHAPTER II

BACKGROUND

This chapter provides the necessary background to understand the types of devices discussed in this document and the basic radiation effects. There are many types of optical sensors used for a wide range of applications. This section outlines the most commonly used devices in space and military applications.

Optical Sensors

There are two general categories of optical sensors: active and passive systems [5]. Active systems operate by detecting reflected radiation from a target illuminated by a photon source while passive systems operate by detecting photons emitted by a target [5]. Since all objects above absolute zero emit photons, passive systems are easier to implement and therefore more commonly used. This type of system will be discussed in the rest of this document. A passive detector works by absorbing the incident radiation (photon of energy $h\nu$), which in turn generates free carriers in the semiconductor [8].

There are two ways this excitation can occur, intrinsically and extrinsically. Extrinsic excitation occurs when carriers are excited from shallow impurity levels in the bandgap as shown in figure 1(a). The cutoff wavelength is determined by the impurity level which allows for operation at longer wavelengths than possible with intrinsic excitation [5]. A disadvantage, however, is the detectors need to be cooled to temperatures below that of liquid nitrogen to increase the lifetime of the impurity

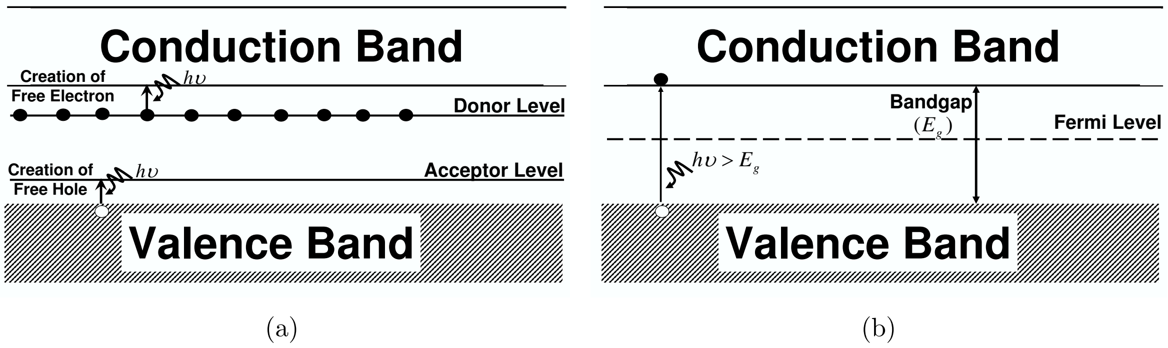

Figure 1: (a) Extrinsic and (b)intrinsic excitation (adapted from [5] and [8]).

centers [8]. Silicon is commonly used for this technology as well as germanium.

In intrinsic excitation, free carriers are ionized across the bandgap. Figure 1(b) shows that photons interacting with the semiconductor that have energy larger than the bandgap will ionize electrons into the conduction band. Those photons with energy lower than the bandgap will cause no interaction. The bandgap therefore determines the cutoff wavelength [5]. Direct energy gap materials are desirable for this type of excitation and the optical absorption is much higher than in extrinsic excitation devices. Intrinsic devices require less cooling than the extrinsic devices, making them more desirable in design [8].

Photoconductive (PC), photovoltaic (PV), and metal-insulator-silicon (MIS) detectors are the three basic types of photon detection devices [5]. A PC detector is basically a resistor made of photosensitive material. The resistivity changes as a result of incident photons, generating free carriers which are then detected by the circuit [5]. PV detectors are basically p-n diodes made of photosensitive material and they collect photo-current induced by photons at the p-n junction [5]. MIS detectors collect carriers generated by photons under the gate region changing the potential of the device, which is detected by the readout circuit. Focal plane arrays (FPAs) are either PC or PV detectors and are used for visible and infrared (IR) detection, while CCDs are MIS detectors and are used primarily in visible imaging [8]. Over the last decade, PV detectors have become more commonly used over the once dominant PC technology [9].

Attached to an optical detector array is readout circuitry. The readout circuitry must be located physically close to the detector array to minimize noise. A detector array and readout circuitry processed in the same material on the same chip are known collectively as a monolithic array [5]. Examples of these devices include silicon CCDs, charge injection devices (CIDs), charge imaging matrices (CIM), and direct-injection silicon devices [10]. In a hybrid array, the detector array and readout integrated circuit (ROIC) are formed separately and joined together with interconnects such as indium columns. Indium is a common material for the joining because it deforms easily and is compatible with photolithographic processing [5]. Common types of hybrid arrays include HgCdTe and InSb FPAs.

In addition to locating the detector array physically close to the ROIC, another method of reducing noise is to operate the detectors at cryogenic temperatures. In general, detectors operating at wavelengths longer than 3 μm are cooled to reduce thermal noise [8]. This cooling allows the detector to operate more efficiently.

Monolithic Devices

A CCD is composed of MIS gates [10]. Packets of charge are induced by incident photons on the pixels of the detector. The pixel data is then transferred to the output by a shift register and three phase clock [11]. This process can be seen in Figure 2 and a generic three phase CCD in Figure 3 [12] . Each pixel has three electrodes.

Charge is collected in potential wells in the n-buried channel by applying voltage to the electrodes. The charge in a pixel is transferred laterally to the next electrode by applying a positive voltage to that electrode and then zero voltage to the previous one. Charge is contained to a row by the channel stops. Finally, the charge packet is transferred to its neighboring pixel. This is done for the entire pixel array until all charge has been transferred to a readout register [11], [12].

CCDs are exceptional devices for time delay and integration (TDI) operation where it is desirable to have the image scanned at the same rate as the charge is clocked. Since charge must be transferred many times, especially for the pixels on the opposite end of the readout circuitry, the CCD is considered a very demanding technology [10]. The time it takes for the readout circuitry to receive and process the charge is longer when compared to other detector technologies. Also, because of the large amount of transfers, signal loss can easily occur [11].

CIDs are MOS devices that require fewer transfers than CCDs, and are therefore easier to fabricate and have a reduced readout time. In a CID, charge is transferred within a pixel and read out directly instead of being transferred among all the pixels within its row before being read out. CIM technology works similarly to a CID, however, by using off-chip integration and short optical integration times even faster readout times are achieved [10].

Hybrid Focal Plane Arrays

A hybrid focal plane array consists of a detector array and a ROIC fabricated separately and joined together with indium bumps. Figure 4 shows a typical structure. The device shown is referred to as a backside illuminated hybrid FPA where the

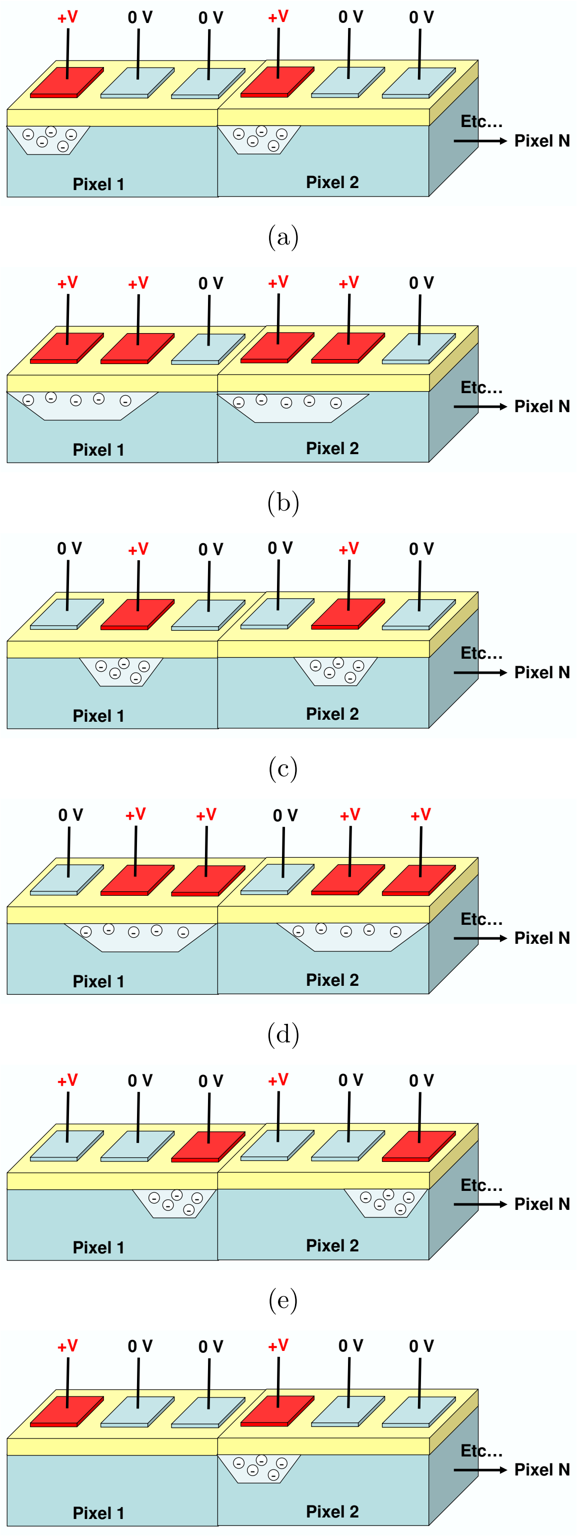

(a)

(b)

(c)

(d)

(e)

(f)

Figure 2: Basic CCD operation using a three phase clock to transfer data. Charge packets are moved from one pixel to the next, until all charge has been removed from the pixels and collected by the readout circuitry.

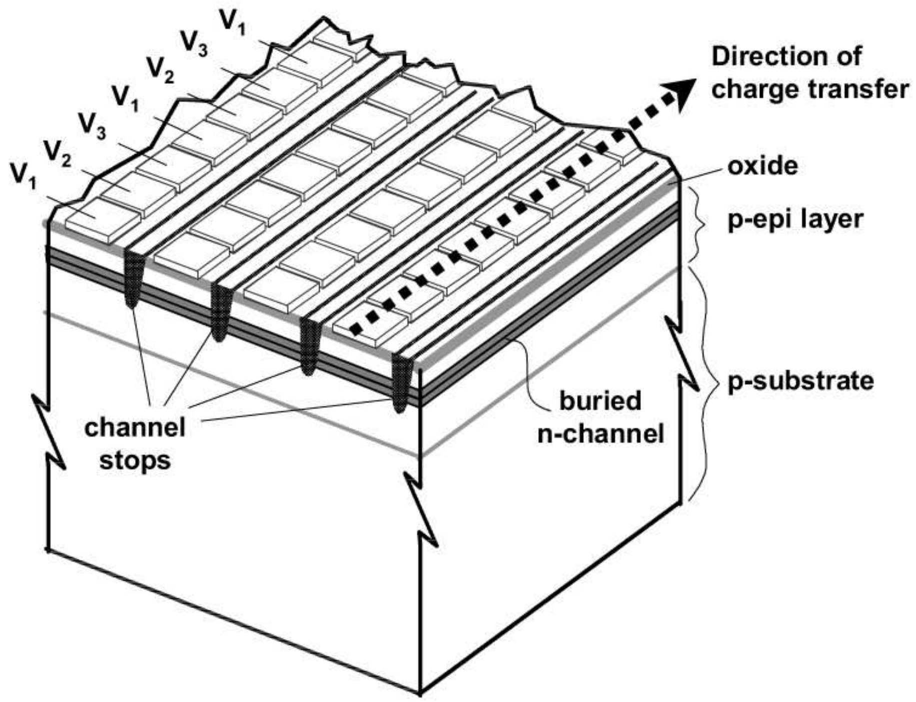

Figure 3: A three phase CCD showing the structure of the device, taken from [12].

incident radiation is incident on the detector array substrate [5]. Directly beneath the array substrate (pixels) are the indium columns used to join the array and ROIC, and then finally the ROIC. Generic operation of a FPA is shown in figure 5. Photons are collected and routed by mirrors to the detector array. The baffles control stray light, and the cold shields block black body emission.

In this type of device, each pixel can be accessed individually, eliminating the series of transfers needed in a CCD technology [11]. This results in an increase of speed and a decrease of dependence on minority carrier lifetime. The ROIC of a FPA is typically a silicon CMOS device because the micron size transistors allow for a smaller ROIC and therefore smaller pixels [9].

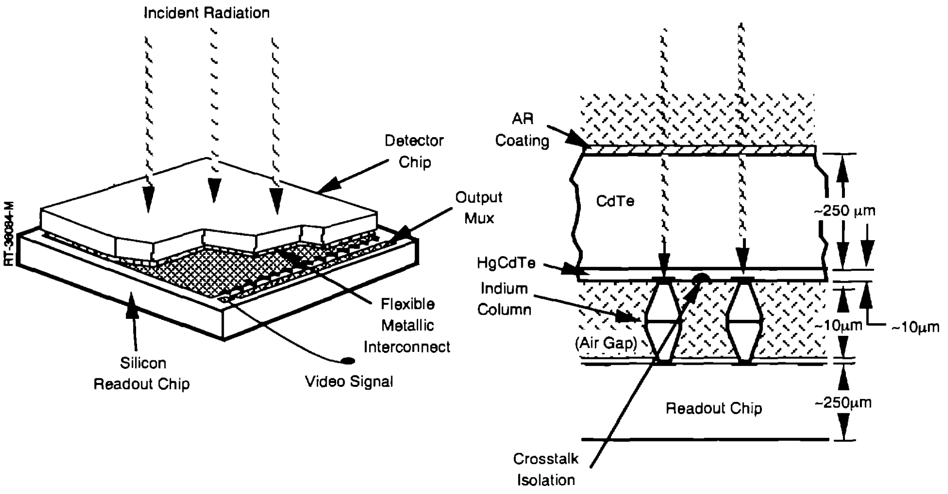

Figure 4: Generic backside illuminated hybrid focal plane array [5].

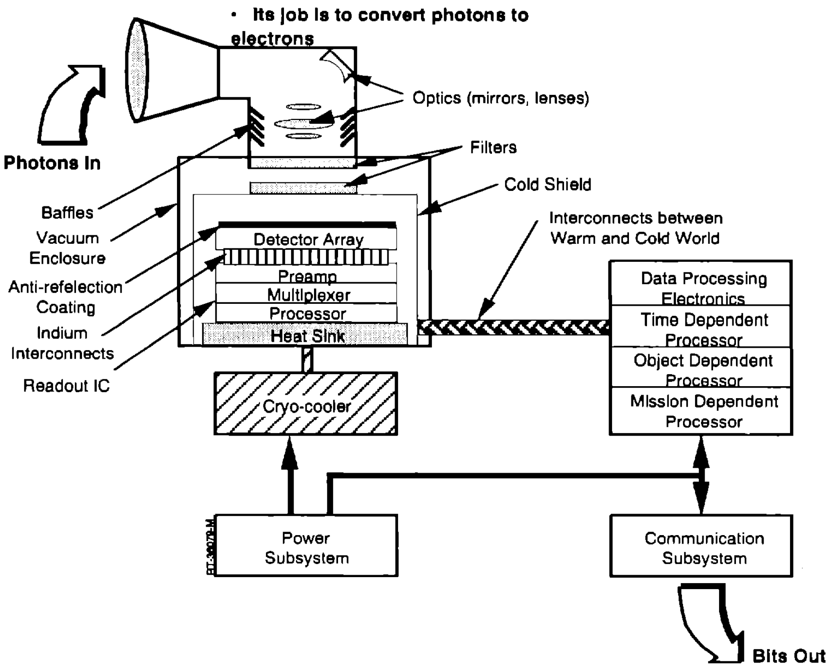

Figure 5: Generic hybrid focal plane array components and operation [5].

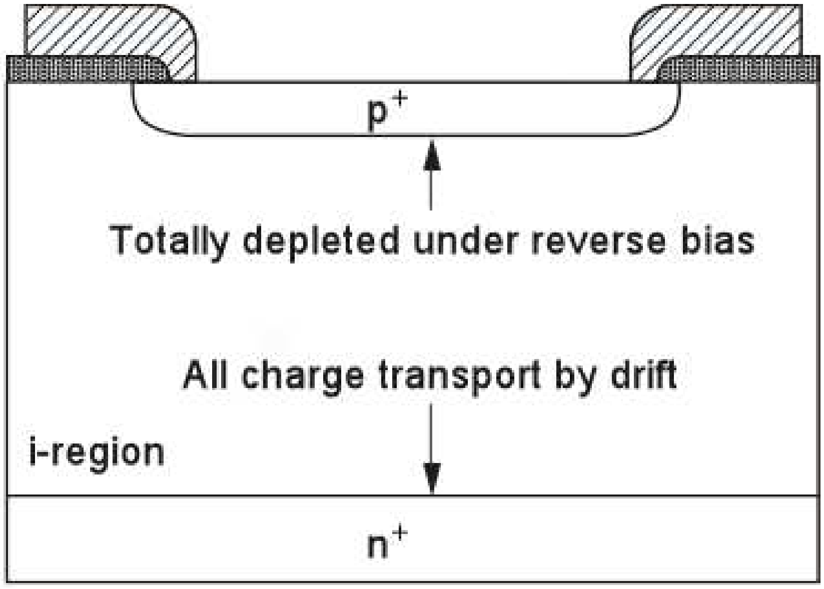

Figure 6: PIN photodiode [11].

PIN Photodiodes

A PIN photodiode is a photodiode with an intrinsic region between two doped regions of n and p type semiconductor as shown in Figure 6. The majority of photons incident on this type of device are collected in the fully depleted intrinsic region. They are then collected by drift, not diffusion, which consequently reduces response time and improves the signal-to-noise ratio [11].

HgCdTe

Over the last 48 years, a great deal of progress has been made in the development of HgCdTe detector arrays. They were originally developed for military applications [13], but over the last couple of decades have become the most commonly used devices for infrared (IR) detection [14], [15]. HgCdTe provides distinct advantages over other materials for detector arrays. These include an easily tailored direct energy gap, flexibility to obtain low and high carrier concentrations, high electron mobility, and a low dielectric constant [5], [15], [13]. $Hg_{1-x}Cd_xTe$ has a variable band gap from 0.073 to 0.748 eV, depending on the x value, and is crystallized in a zinc blend structure [13]. A zincblende lattice is similar in structure to a diamond lattice. The structure is common in III-V semiconductors such as gallium arsenide (GaAs) and gallium phosphide (GaP) [6]. Doping is typically below 10^{16} cm^3 in the base region and surface passivation is done with CdTe and CdZnTe [13]. The material is grown by traveling heater method, liquid phase epitaxy (LPE), or vapor phase epitaxy. For large area FPAs, the dominant growth technology is LPE [8].

HgCdTe detector arrays can operate from the near infrared region (NIR; starting at 0.7 μm) to the very long wavelength infrared region (VLWIR; up to 20 μm) by tailoring the band gap of the material. HgCdTe detectors operate the best at medium wavelength infrared (MWIR; 3-7 μm) and can be used for both hot and warm body detection [13]. Detectors considered “high temperature” operate at temperatures greater than 65 K, and “high performance” detectors operate between 40 to 65 K [5].

Natural Space Environment

The natural space environment consists of particles that can contribute to transients in electronic devices on satellites and other spacecraft. The number of particles and their typical energies vary greatly with altitude and solar activity. The particles are from three general categories: solar particles, particles trapped in the Earth’s magnetosphere, or galactic cosmic rays.

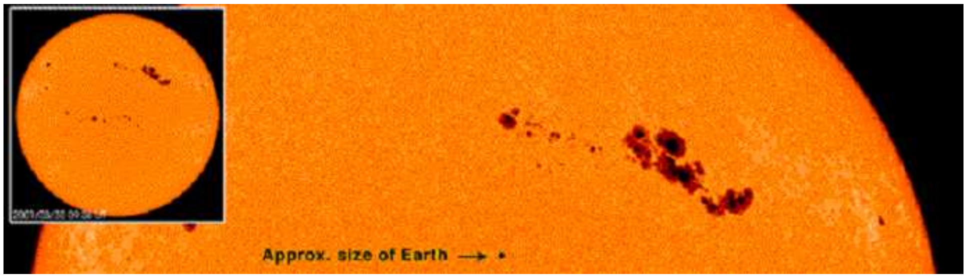

Figure 7: A cluster of sunspots shown relative with the size of Earth [17].

The Solar Environment

The Sun's outermost layer, known as the corona, has a temperature of approximately 1.5×10^6 K, which is too hot for gravity to hold onto particles [16]. Because of this, the Sun is continuously emitting protons, electrons, alphas, and some heavy ions. This continuous stream of particles is known as the solar wind and travels at speeds averaging 400 km/s (about 1 million miles per hour) [17]. The Sun also emits particles via solar flares and coronal mass ejections.

Solar flares are caused by explosions near sunspots. Sunspots are regions within the Sun's photosphere with magnetic field strengths thousands of times stronger than that of Earth. They appear as dark spots on the surface of the Sun and are 2000 K cooler than other regions. The earliest known sunspot was recorded in 28 BC, and continuous data documenting their locations exist since 1849 [17]. Figure 7 shows a cluster of sunspots and their sizes relative to the size of Earth. Figure 8 shows the number of sunspots recorded per year since 1700. Notice the number of sunspots fluctuates with the solar cycle, every 11 years [18].

When magnetic field lines become twisted near sunspots, coronal holes allow particles to escape. A solar flare releases as much energy as a billion megatons of TNT [16]. The result is an increase in solar wind density that is very rich in heavy ions.

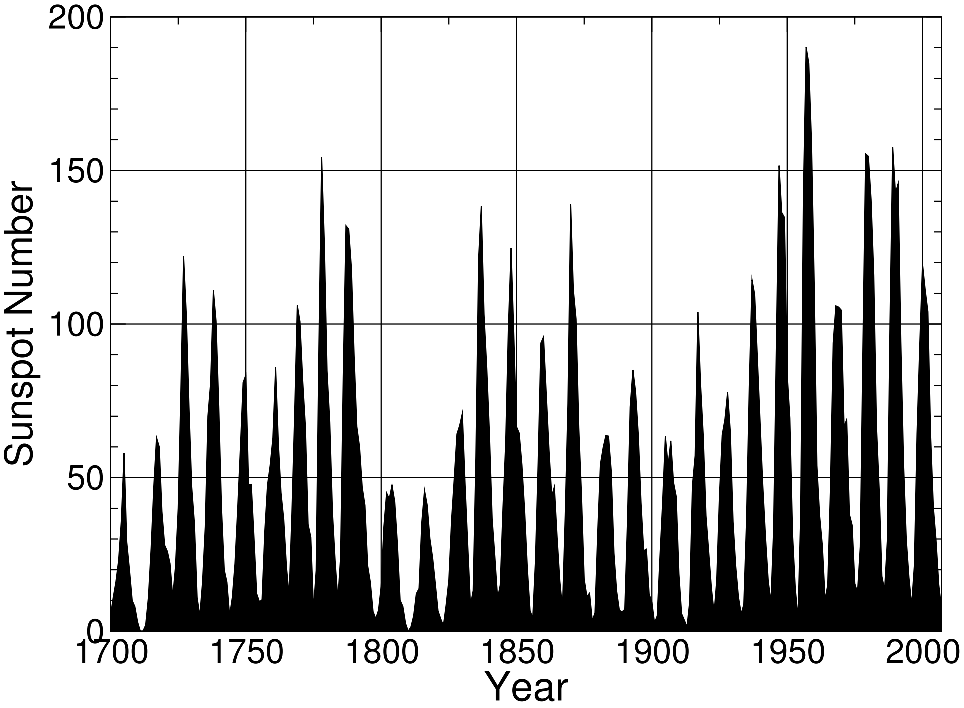

Figure 8: The number of sunspots recorded every year since 1700. Data from [19].

Figure 9 shows a solar flare from October 10, 1971.

Coronal mass ejections (CMEs) are observed as large gas bubbles are ejected from the Sun. They release 10^{17} grams of plasma and are responsible for an increase in the solar wind velocity and are rich in protons. Figure 10 shows a large CME captured by SOHO's (Solar and Heliospheric Observatory) LASCO (Large Angle and Spectrometric Coronograph) on November 8-9, 2000.

Trapped Particles

The Earth's magnetosphere is defined by the solar wind's interaction with the Earth's magnetic field. Figure 11 shows the Earth's magnetosphere and its key elements. 99.9% of the solar wind particles will pass around the Earth's magnetosphere. However, the 0.1% that do not pass by the Earth will leak into the magnetosphere via

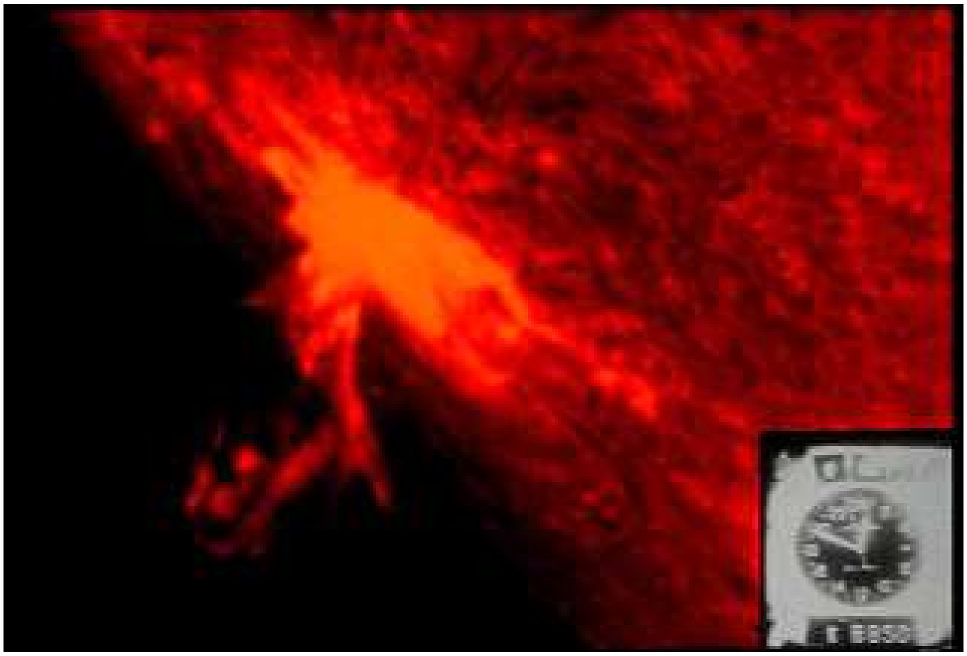

Figure 9: A solar flare that occurred on October 10, 1971 [17].

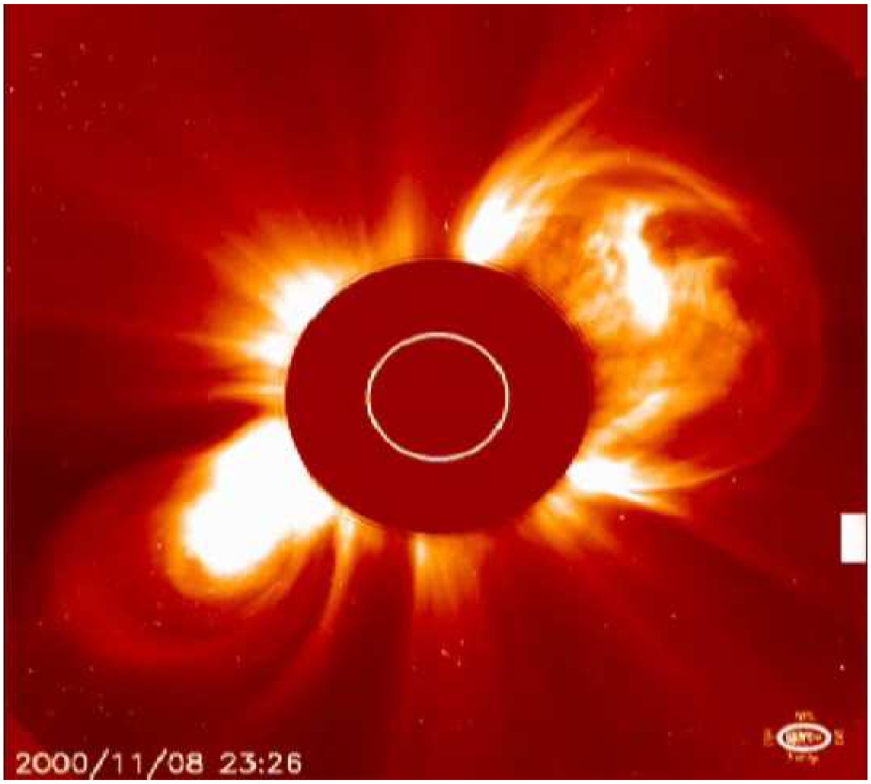

Figure 10: Coronal mass ejection occurring on November 8-9, 2000 (still image extracted from video) [20].

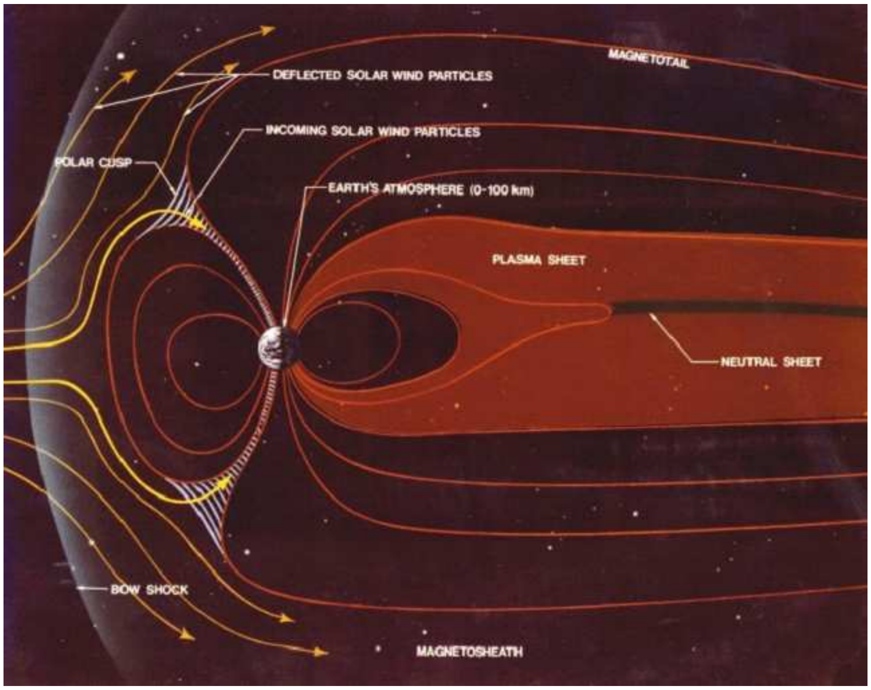

Figure 11: The magnetosphere and its key regions [17].

the polar cusps and become trapped [17]. These particles that become trapped contribute to the formation of the Van Allen belts. The Van Allen belts consist primarily of electrons and protons, with some heavy ions (Z > 1).

The inner Van Allen belt comes closest to Earth at the South Atlantic Anomaly (SAA). In this region many spacecraft are forced to shut down because of the radiation intensity. The location of this region can be seen in Figure 12. Here, the geomagnetic and rotational axes are tilted and shifted relative to each other, resulting in an inner edge of the proton belt dipping lower in altitude, as shown in Figure 13.

Galactic Cosmic Rays

The galactic cosmic ray (GCR) environment typically consists of 85% protons, 14% alpha particles (helium), and 1% heavy ions [23]. While only 1% of the galactic

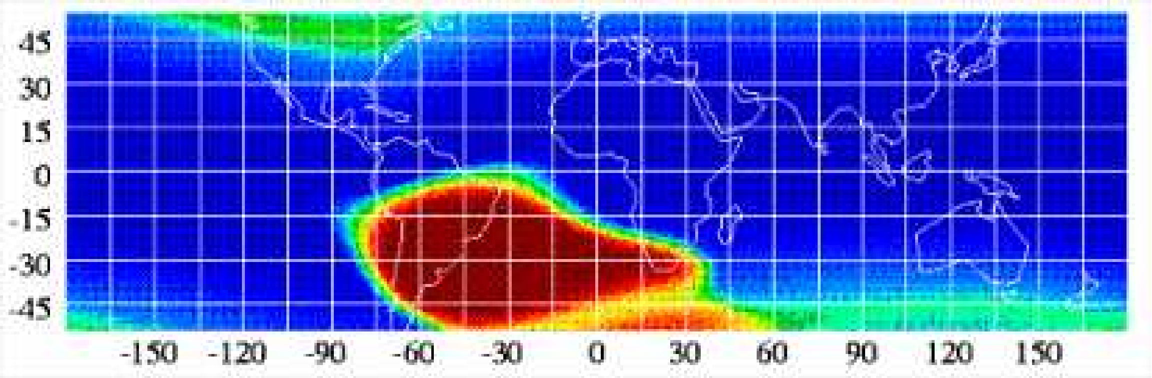

Figure 12: The location of the South Atlantic Anomaly [21].

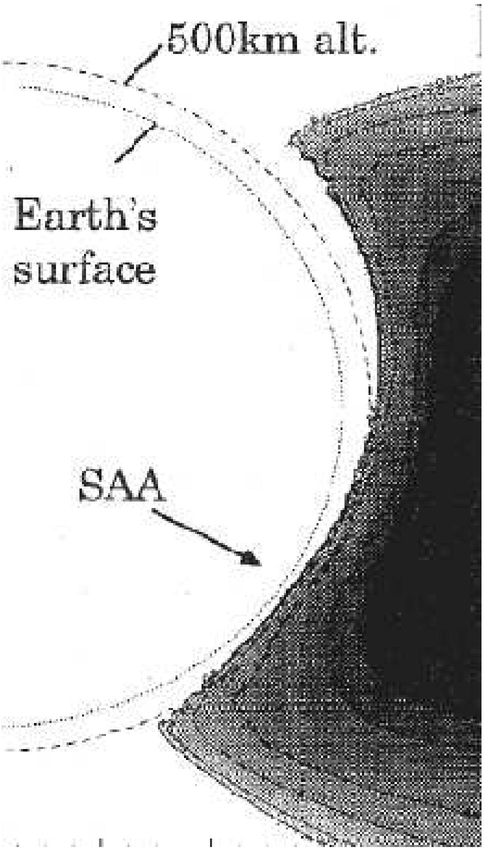

Figure 13: Illustration of how the proton belt dips closer to the Earth's surface at the SAA [22].

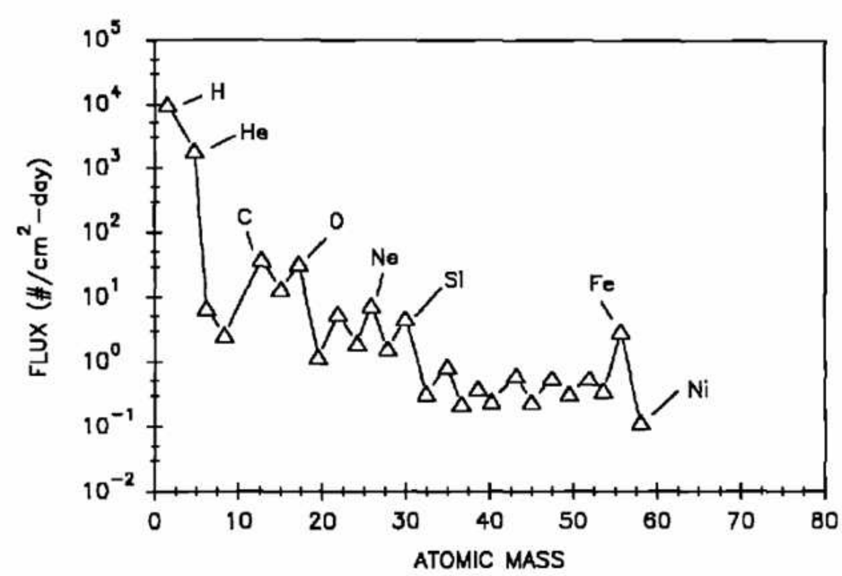

Figure 14: Galactic cosmic ray particle flux as a function of atomic mass for ions up to 60 atomic mass units [26].

cosmic rays are high energy heavy ions, they are very important when considering transient radiation effects in electronics because one hit by a heavy particle can deposit a great deal of energy into a device [23]. Spacecraft shielding can help block out lower energy particles, but can also create secondary particles that have the potential to likewise deposit energy into electronics [24] or cause higher energy particles to slow down and become more ionizing [25]. Figure 14 shows the ion flux as a function of atomic mass up to nickel for the GCR environment. There are peaks at hydrogen (protons), helium (alphas), carbon, oxygen, nitrogen (the last three are known as the CNO environment), neon, silicon, and iron.

Particles in the galactic cosmic ray environment that can affect devices in space range from 0.1 to 10^5 MeV/nucleon. Figure 15 shows the frequency of protons found in the GCR and was created using CREME96 [27], assuming 100 mils of aluminum shielding. It plots particle flux (cm^2-s-MeV)$^{-1}$ as a function of particle kinetic energy

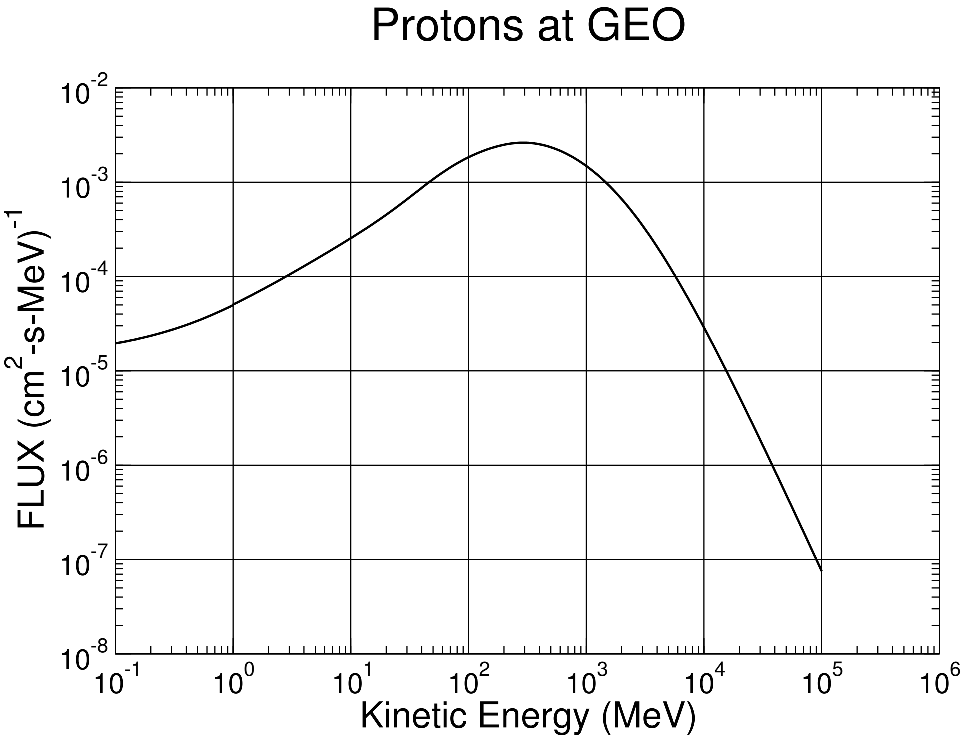

Figure 15: Proton particle flux as a function of kinetic energy at GEO [27].

(MeV). The peak in the flux occurs near 500 MeV. This is true for all species found in the GCR. Protons are the most abundant charged particles at geosynchronous orbit (GEO), followed by alphas, oxygen, neon, and iron (for most energies). The heavier ions are less abundant, but can still have a large effect on the behavior of devices during space flight.

Energies consistent with ground test facilities cover the lower range of Figure 15, typically from 3-500 MeV for protons. Since energies above this are not obtainable by test facilities, a lower range is used to predict the on-orbit response of a microelectronic device.

Radiation Effects

Radiation effects on detector arrays are enhanced due to cryogenic operating temperatures and their sensitivity to noise. The cold temperatures affect both the detector array itself and the ROIC. In this document, the focus will be on radiation effects in the detector arrays.

Ionizing radiation from particles found in the natural space environment can contribute to total-ionizing dose damage (TID), single-event effects (SEEs), and displacement damage (DD). Protons are accountable for all types of effects, electrons cause TID and DD, and heavy ions cause SEEs and DD. Total-dose damage occurs over the lifetime of the device, and is due to the build up of trapped charges in the materials from radiation [28]. Displacement damage also occurs over the lifetime of the device and is a result of atoms being knocked out of their lattice sites, creating defects in the materials that make up the device [23].

A SEE is a localized interaction of a single ionizing particle, which occurs at random and can have an immediate impact on the device response [29]. SEEs are the result of energy deposition within the materials of a device which contribute to a change in the device's charge. One type of SEE is a single-event transient (SET) [29]. In a detector array, a SET appears as a false signal and degrades the quality of the image. The likelihood a SET will occur in a space environment is commonly given as a rate in errors/bit/day. The focus of this thesis is on SETs and energy deposition in a FPA resulting from incident protons.

FPA have advantages in mitigating radiation effects over CCDs. CCDs require collected charge to be transferred many times before being read out, and a loss of charge through proton induced traps can occur [12]. Hybrid FPAs require, at most, one transfer, thereby reducing the trapping vulnerability. On the other hand, a silicon PIN device can have quite a thick collection volume, which makes the quantitative evaluation of the sensitivity to proton-induced transients an important issue.

Transient Effects

Although heavy ion transients do occur, protons are the primary cause of SETs in FPAs [3]. As a proton traverses a detector array, electron-hole pairs are generated along the particle's track. The energy deposited is dependent on the dE/dx (stopping power) of the particle and the track length. A detector array in an isotropic environment, such as encountered in space, will have a variety of track lengths [3]. Once a particle traverses the array, charge is transported by both drift and diffusion, as in most semiconductor devices affected by radiation. Drift refers to the movement of charge due to an electric field [6]. In a pixel composed of silicon, 100% collection efficiency may be approached [30].

Transient effects cause an increase in noise and a decrease in signal-to-noise ratio. Proton induced transient noise can mimic a signal and detectivity is degraded. Detectivity is the primary figure of merit for detectors [5]. It is the ratio of the responsivity to the noise normalized by the detector area and designates the sensitivity of a detector [31].

Transient effects result from primary particles in space traversing the detector, and ionizing secondaries created from nuclear reactions within the material from the primary ion striking a nucleus of the target material. Gamma-induced pulses, common in HgCdTe detectors, are one example of how a nuclear reaction contributes to transients in a detector array. A gamma interacts with the materials surrounding a detector creating secondary electrons, which are subsequently collected by the detector [15]. Nuclear reactions are described further in the next section. Charge generated on a node of a detector array remains there until the array is reset at the end of the integration time [30]. However, integration times can be 1000 seconds [15] and the false signal will remain that entire time.

Displacement Damage

Defects occur in the lattice as protons pass through the semiconductor materials. These defects can form stable complexes with impurities and permanent degradation [5]. Displacement damage (DD) results in a decrease in generation lifetime, which results in an increase in dark current [12]. This arises from the bulk of the devices and occurs in depletion regions via energy levels near midgap [9]. Both the mean dark current and the dark current distribution in an array are increased [12]. The increase in dark current due to DD has an effect on the performance of the devices due to increases in dark current shot noise, loss of dynamic range, and introduction of dark current spikes [9]. Effects of DD on dark current are enhanced by the presence of relatively high electric fields in imagers [9]. The high electric field leads to a decrease in the potential barrier thereby increasing the potential for funneling and an increase in dark current. This is known as field-enhanced emission [32], [33], [34].

A single pixel in a detector array can be struck by an energetic proton more than one time during integration in a high flux environment. This can cause an increase in dark current in one pixel while leaving neighboring pixels untouched, or with little damage. The result is a detector with nonuniformly distributed displacement damage and dark-signal nonuniformity (DSNU) [9].

Displacement damage is also responsible for charge transfer efficiency (CTE) degradation in CCDs due to carrier trapping within the n-buried channel [12], [3]. Defects in the n-buried channel make it difficult for the charge packets to efficiently move through the rows to the ROIC. This degradation of the CTE results in a loss of signal charge. There is also a reduction of the signal-to-noise ratio due to temporary trapping centers in the forbidden gap [9].

Total Ionizing Dose

In detectors, total ionizing dose (TID) leads to a buildup of trapped charge. This in turn produces a voltage shift in the pixels and increases surface dark current [3]. There is an increase of hole trapping at cryogenic temperatures due to the low mobility of holes. Hardening against TID includes thinning the oxide to reduce the area in which trapping can occur [5]. TID effects are well known in imagers. Therefore, hardening techniques have already been implemented in most modern devices used in space applications.

Energy Deposition

This section will define several key terms used throughout this document in regards to energy deposition. The total stopping power of a particle refers to the energy loss per unit length and is the sum of the electronic and nuclear stopping power:

$$(\frac{dE}{dx})_{total} = (\frac{dE}{dx})_{electronic} + (\frac{dE}{dx})_{nuclear} \tag{1}$$

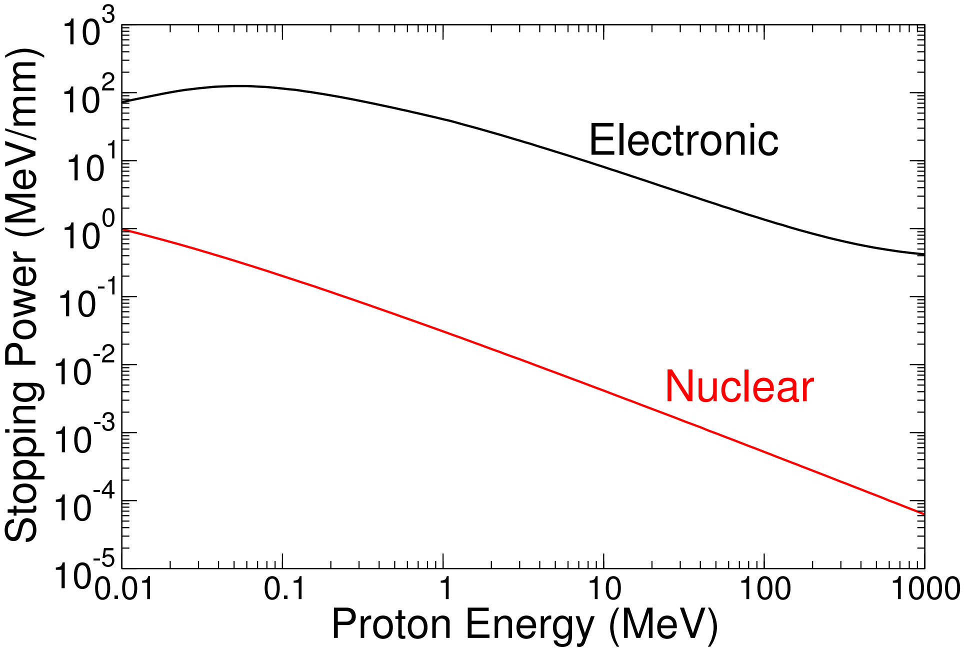

Figure 16: The electronic and nuclear stopping power of protons in silicon, computed with SRIM [35].

Figure 16 shows the electronic (or ionization) and nuclear stopping power of protons in silicon, computed using SRIM [35]. Notice that at all energies the electronic stopping power dominates. However, this is not true for all incident particles, such as ions heavier than Z $>$ 1. Figure 17 shows the stopping power of silicon ions in silicon where the nuclear stopping power dominates at lower energies. In the literature, the electronic stopping power is often referred to as linear energy transfer (LET), given in MeV-cm^2/mg.

The electronic stopping power refers to the energy lost due to direct ionization. Direct ionization occurs when an incident particle interacts with the electrostatic field of an electron in the target atom [36]. The energy introduced into the solid by the incident particles allows a bound electron to leave an atom, and an electron-hole pair is created. This type of reaction is shown in Figure 18. In most devices this is the

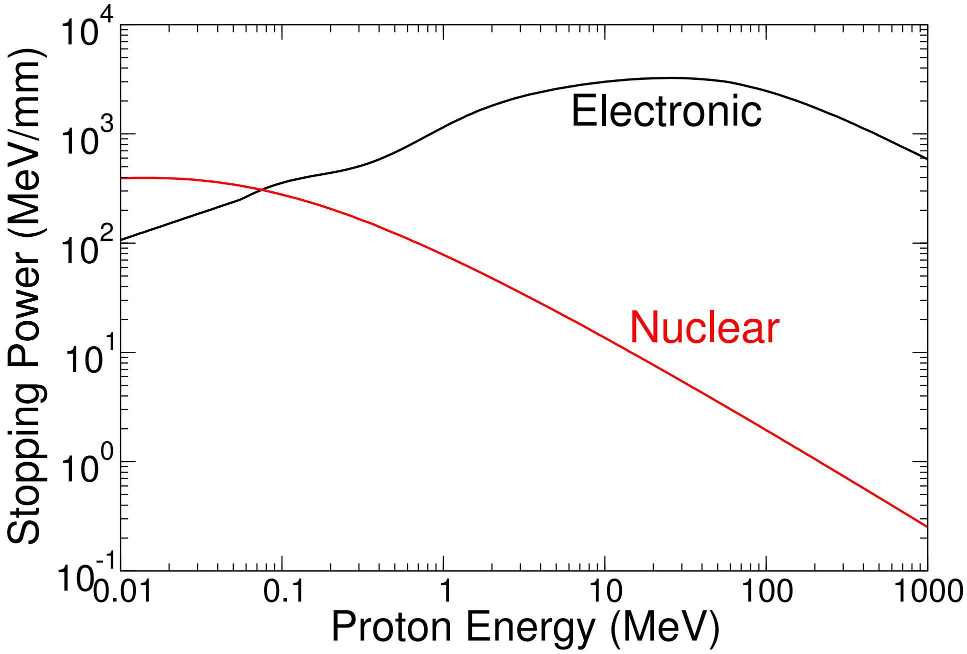

Figure 17: The electronic and nuclear stopping power of silicon ions in silicon, computed with SRIM [35].

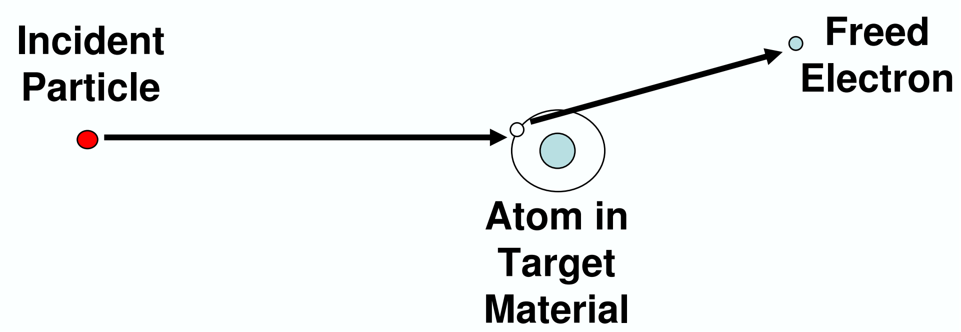

Figure 18: Electronic collision resulting in direct ionization when an electron-hole pair is created, adapted from [36].

main mechanism responsible for upsets from ions with Z $>$ 1 [37].

Nuclear stopping power refers to the energy lost due to indirect ionization, or nuclear inelastic and elastic collisions and screened Coulombic scattering. A nuclear inelastic collision results in the breakup of the target nucleus and the production of several secondary particles, as shown in Figure 19 [36]. The secondary particles

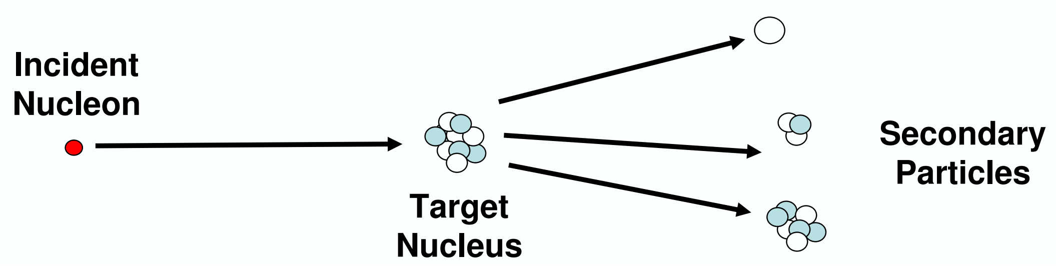

Figure 19: Nuclear inelastic collision resulting in indirect ionization when an incident ion hits the nucleus of a target atom creating several secondary particles, adapted from [36].

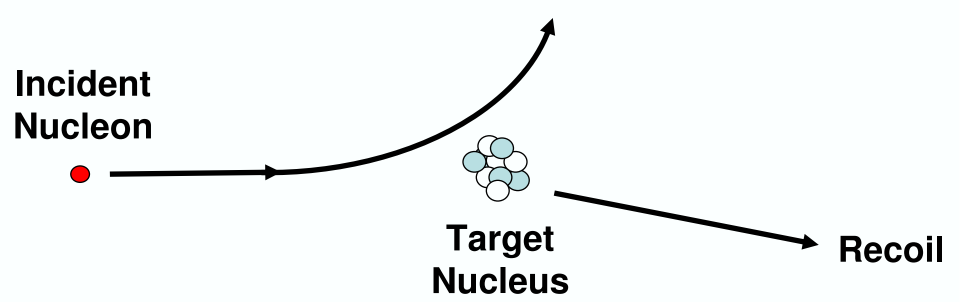

Figure 20: Nuclear elastic collision resulting in indirect ionization when a recoil atom is created, adapted from [36].

created through indirect ionization can be much heavier than the original particle, and therefore have the capability to deposit larger amounts of energy [38]. In a nuclear elastic collision, the target nucleus is not modified, but recoils with energy transferred from the incident particle as a result of the nuclear force. It is then free to interact within the material; see Figure 20 [36]. Screened Coulombic scattering is similar to a nuclear elastic collision in that the nucleus is not modified, but the particle changes energy and direction. A Coulombic scatter is the result of the electrostatic force and results in a recoil with a smaller angle and less momentum compared with the recoil from a nuclear elastic collision.

Simulation Tools

Monte Carlo techniques to predict radiation transport have been implemented for several decades (see [39], [40], and [41] for examples). Monte Carlo methods are computational algorithms based on the use of random numbers and probability statistics for solutions to real systems. In general, Monte Carlo methods consist of probability density functions (pdfs), random number generators, sampling rules, tallying, error estimation, variance reduction techniques, and parallelization and vectorization [42]. Monte Carlo methods are used in a variety of fields and are useful for solving equations with large numbers of possibilities [43]. They are often compared to a game of chance, which results in the solution to a problem. Because of Monte Carlo method's ability to solve large problems with relatively high efficiency, as compared with typical deterministic calculation techniques, it is ideal for scattering mechanisms [43]. Many incident particles and secondary particles can be accurately accounted for. Monte Carlo methods are also ideal for complex problems because they require fewer assumptions and approximations than analytical approaches [38].

Over the last couple of decades, Monte Carlo methods have been applied to predict energy deposition from complex nuclear reaction events [44], [45], [46], [47]. In general these tools have been limited to a small number of incident particle types, typically ions with $Z \leq 1$. Table 1 presents several codes and the particles of interest within them.

MRED - A Geant4 Application

The Monte Carlo application used in this work is called MRED (Monte Carlo Radiative Energy Deposition) [53], [54], [55], [56]. MRED is built on the Geant4

Table 1: Monte Carlo codes used for radiation transport through materials.

Monte Carlo Code	Incident Particles Available
BRIC [44]	protons
CUPID [48]	protons
EGS4/EGSnrc [49]	electrons, photons
MCBEND [50]	neutrons, gamma rays, electrons
MCNP [47]	neutrons, photons, electrons
MORSE [51]	neutrons, gamma rays
SEUSIM [52]	protons

libraries with Vanderbilt additions, including a model for screened Coulomb scattering of ions [57], tetrahedral geometric objects [54], a biasing technique for cross section enhancement, and a number of additional features relevant to semiconductor device applications. Simulations using MRED included physics processes that are relevant for radiation effects applications, including electromagnetic and hadronic processes, and elementary particles that live long enough to be tracked [57]. The Geant4 libraries frequently contain alternative models for the same physical processes. These may differ in level of detail and accuracy. Generally, MRED is structured so that all physics relevant for radiation effects applications are available and selectable at run time. This includes electromagnetic and hadronic processes for all relevant particles, including elementary particles that live long enough to be tracked. There are several models available for the description of intra-nuclear cascades of nucleons produced by neutron and proton irradiation and are user selectable at run-time. Results from using the "Standard Screened," "EM Penelope," and "EM Low Energy" models are discussed in Chapter 4.

"Standard Screened" includes the Geant4 standard electromagnetic (EM) physics [58] (ionization, bremsstrahlung, gamma conversion, and other charged particle and gamma interactions [59]) together with the VU screened Coulomb scattering for ions [57]. In MRED 8, the "Standard Screened" model is considered the most complete and fastest, and is therefore the default for simulation. This model was used throughout this document, except where noted otherwise in Chapter 4.

The "EM Penelope" model was developed from the PENELOPE code (PENetration and Energy LOss of Positrons and Electrons) [58], [60], designed specifically for Monte Carlo simulations. The model includes Compton scattering, photoelectric effect, Rayleigh scattering, gamma conversion, bremsstrahlung, ionization, and positron annihilation, as well as the VU screened Coulomb scattering [58].

The "EM Low Energy" model includes Geant4 low energy [58] as well as the VU screened Coulomb scattering. The low energy model is optimized for lower energy particles and includes the photo-electric effect, Compton scattering, Rayleigh scattering, gamma conversion, bremsstrahlung, ionization, and fluorescence of excited atoms [58].

Another user selectable parameter in MRED varied for simulations in Chapter 4 of this document is "range cuts," a parameter given in distance. This refers to the threshold at which no electron or photon will be generated. Geant4 translates this distance to an energy for each material included in the run [61], [62].

The version of MRED used in this work, version 8, is structured such that an input file is a python script created by the user stating all necessary commands and passed into MRED. This file contains information regarding the physics, structure, ion type and energy, and the desired output. An example of a typical input file can be viewed in Appendix A. Each line is documented so the reader may understand the commands. The example presented includes the simulation of 63 MeV protons at an angle of 45° on the complex silicon imager structure shown in Chapter 5. Note that future versions of MRED, including the upcoming online version, may not have the same type of input files as used in this work. The files presented here are for reference only.

Simulations for this work were conducted through Vanderbilt University's Advanced Computing Center for Research and Education (ACCRE). Through ACCRE's computing cluster, simulations using the MRED application were done in parallel, thereby allowing larger simulations to be performed in shorter amounts of time. A python script, developed by Dr. Marcus Mendenhall at Vanderbilt University, allows the MRED application to be duplicated to a specified number of copies and then each individual copy runs to completion independently.

The output of the version of MRED used in this work can be user-defined or defaulted to an hdf5 file [63]. The hdf5 file written contains information about the specific MRED run, including target size and material of each layer, sensitive volumes, gun details, histograms, etc. In this work, the default hdf5 files were written out and the results were post-processed using python.

Technology Computer Aided Design

Synopsys® technology computer aided design (TCAD) was used for modeling the charge transport in the silicon diode array. For this dissertation work, two-dimensional (2-D) device simulations were performed with version 10 using DEVISE and DESSIS [64]; these simulations are discussed in Chapter 4. TCAD works by solving the Poisson and carrier transport equations in a device and determining terminal currents, voltages, and charges. Key regions of the device are defined according to the user by creating a mesh within the device. Smaller mesh spacing is used for regions of key interest.

CHAPTER III

MOTIVATION AND HISTORY

Motivation

Modern FPAs have noise specifications on the order of only a few electrons and integration times as long as 1000 seconds [65]. The number of electrons in a detector array is directly related to the signal output of the FPA. Optical currents are small and near noise levels. A single electron can produce enough charge to disrupt a signal [5]. With these stringent requirements, it is important to thoroughly study the effects of radiation on these devices. Figures 21 and 22 show how the image produced by a CCD can be degraded by a solar proton event [20].

Figure 21 shows a large CME captured by SOHO's (Solar and Heliospheric Observatory) LASCO (Large Angle and Spectrometric Coronagraph) on November 8-9, 2000. The images show the progression of the image quality before, during, and after the solar event. Coronal mass ejections, very rich in protons, increase the solar wind velocity and can reach satellites in Earth's orbit quickly. Figure 22 captures a coronal mass ejection occurring on August 26, 2001. The figure on the right shows the image produced by a charge-coupled device (CCD) over an hour later due to the solar proton event [20].

Imaging devices give engineers a unique insight into single events since they can be visually observed. This type of disturbance in an imager could result in serious mission consequences. For example, if the FPA is being used as a star tracker, the false signal could be read as a star and the spacecraft would become misguided.

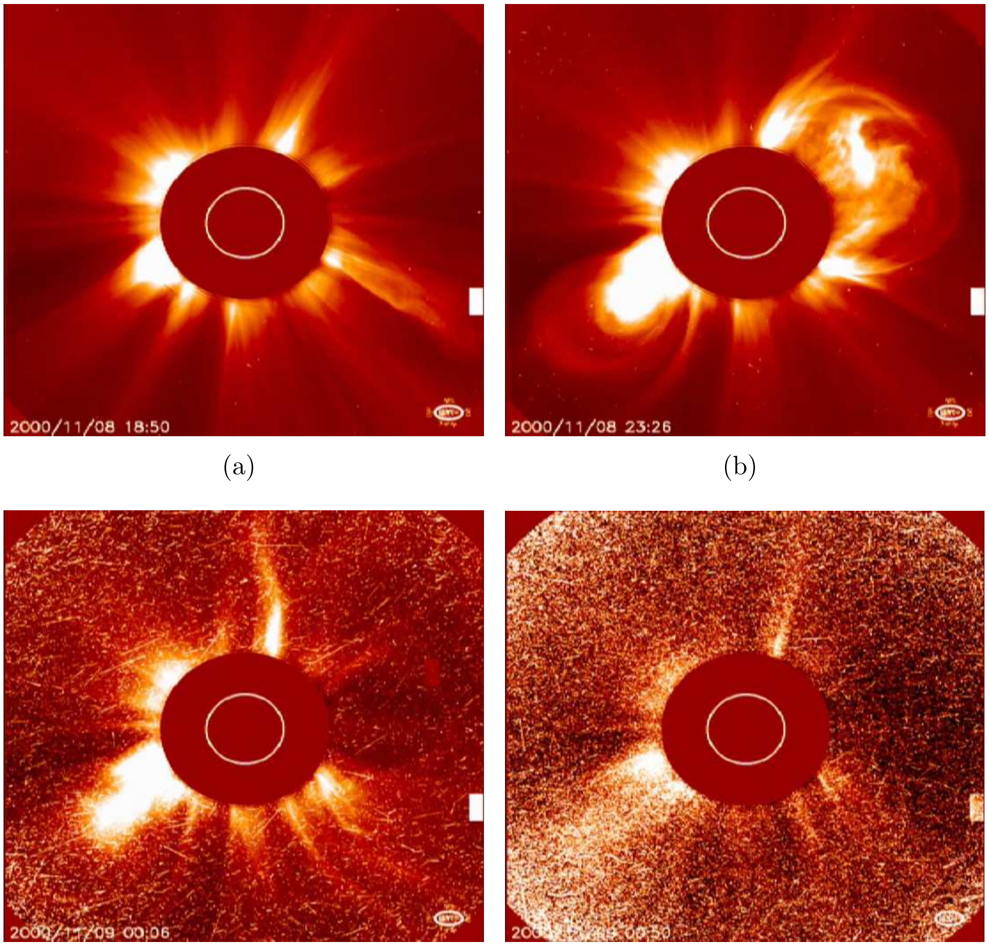

(a) (b)

(c) (d)

Figure 21: Progression of a CME emitting protons that degrade the image being produced from SOHO's LASCO: (a) starting image; (b) coronal mass ejection; (c) image beginning to degrade; and, (d) image severely disturbed due to protons from CME (still images extracted from video) [20].

Spacecraft shielding helps mitigate incident electrons, but it does not protect against protons, which also deposit charge and create secondary electrons.

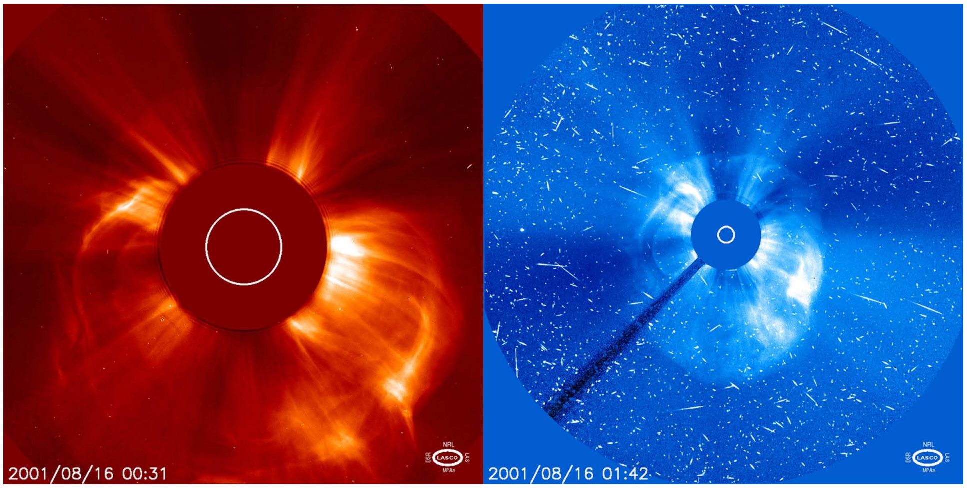

Figure 22: Coronal mass ejection captured by LASCO on August 26, 2001. Over an hour later, degradation of the image produced by the optical detector can be seen on the right figure [20].

History

In the late 1970s, research was primarily focused on displacement damage in detector devices. At that time, detector devices were single-element devices and displacement damage was the dominant concern [15]. By the mid 1980s, multi-element detector arrays were being developed and the focus shifted to total-dose induced radiation effects. In the early 1990s, radiation-hardened arrays were introduced and transient events became the immediate concern. Today, both displacement damage and transients are the main concerns [15].

In November 1995 the Infrared Space Observatory (ISO) was launched as the world's first orbiting infrared observatory [66]. It was equipped with four optical detectors, referred to as the ISOCAMs [67]. The cameras were operated at 2.4 K by passive helium cooling and contained 32 × 32 pixels with a pitch of 100 μm and a thickness of 500 μm [68]. ISO operated for 18 months in a 24 hour elliptical orbit. Data were taken 16 hours of each day while the spacecraft was exposed to GCRs.

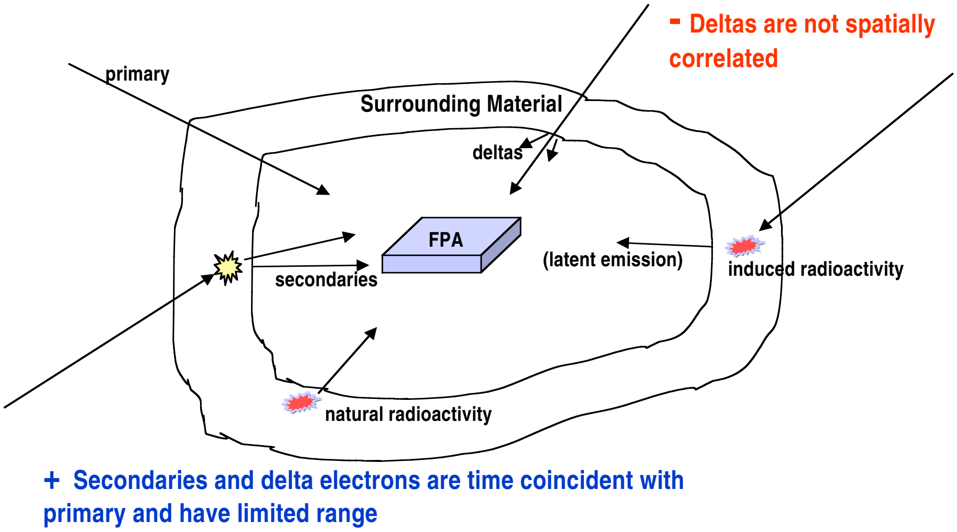

Figure 23: Pictorial explanation of the secondary environment affecting FPA on-orbit adapted from [30].

During 8 hours of each day, the ISOCAMs were unusable after the spacecraft passed through the proton radiation belts [4], [69].

Calculations of the on-orbit transient event rate compared to the expected event rate revealed, through analytical calculations, that the contribution of secondary particles and delta electrons account for 80% of the glitch rate [4]. In other words, transient measurements were 80% higher than could be accounted for from primary particles alone. A pictorial explanation of the secondary environment is shown in Figure 23, adapted from [30].

The ISOCAM results showed the importance of taking into account the secondary particle environment and launched a new era of study in the detector community. It was evident that a high fidelity modeling approach was needed for predicting the on-orbit response of imagers. Researchers have been working on many models to predict the response of detectors. Many of these are analytical approaches requiring several assumptions and approximations such as the path of the ion, LET, secondaries produced, etc. As discussed above, Monte Carlo based simulations reduce the need for these [38]. However, even though these type of simulations are the best option, there are very few reported Monte Carlo based simulation results on FPAs.

In 2002, Claret *et al.* published a paper using Geant4 to predict the glitch rate of a CCD aboard ISOCAM [68]. The calculated on-orbit glitch rate was 0.36 s^{-1} from primary GCRs, 0.29 s^{-1} from secondaries, and at most 0.35 s^{-1} from secondary alphas from the ^{232}Th lens for a total glitch rate of 1 s^{-1}. The result of the Geant4 simulation showed a glitch rate of of 0.83 ± 0.12 s^{-1} from GCR protons, 0.045 ± 0.026 s^{-1} from alphas of the GCR, and 0.002 ± 0.35 s^{-1} from the secondary alphas resulting from the ^{232}Th lens. Secondary alphas originating in the ^{232}Th lens were not determined by the Monte Carlo simulation, but instead assumed to be 4 MeV and of normal incidence. The simulated glitch rates included contributions from the primary particle and secondary contributions, and were not reported independently [68].

In 2004, Onoda *et al.* published a paper using a Monte Carlo based simulation to predict the proton induced charge in a silicon PIN photodiode [70]. The results of that study are shown in Figure 24. The experimental and simulated curves differ for most of the curve. The authors attribute this difference to not considering funneling in the simulation, the assumption of a constant energy loss in the simulation, displacement damage occurring during the experiment, and/or too few points available in the radiation model [70].

The importance of understanding proton-induced energy deposition in FPAs is evident through degraded images by devices in-orbit, as well as the data collected by ISO. However, despite the need for this understanding, there remains a lack of

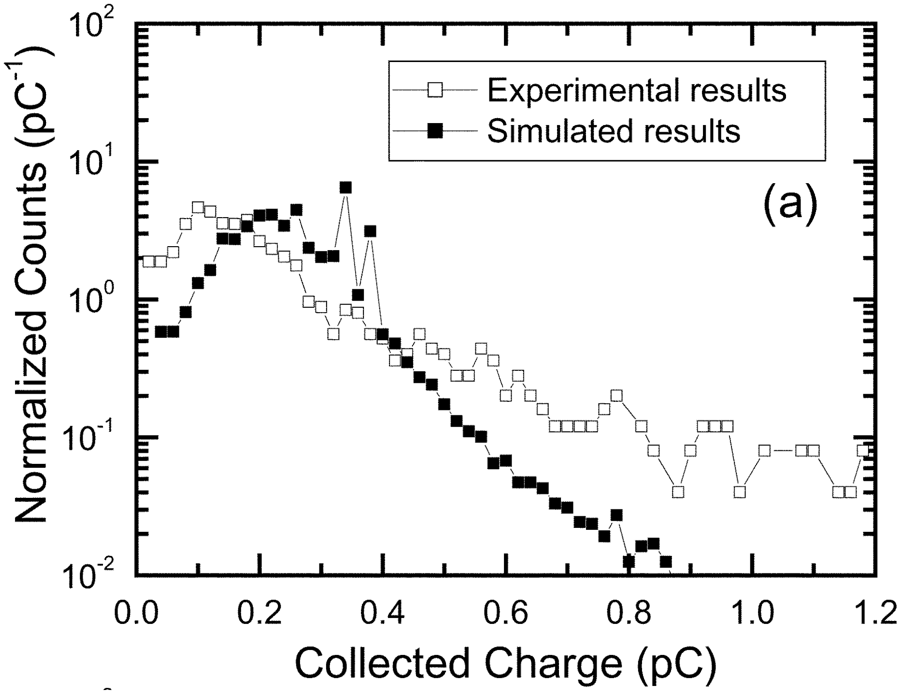

Figure 24: Comparison between experimental and simulation results from Onoda *et al.* [70].

dependable models for FPAs. There have been no previous reports of Monte Carlo simulations that allow the user to separate out different reaction mechanisms and consider their contributions to transients in detectors. The work presented in this thesis will show a Monte Carlo modeling approach that provides a significantly improved understanding of the effects of protons on a FPA.

CHAPTER IV

SILICON PIN FPA MODELING AND EXPERIMENT

Experimental Description

FPA Description

The focal plane arrays (FPAs) in this document were fabricated by Rockwell Scientific Company (RSC). They are visible FPAs consisting of a silicon PIN detector array with a hardened complementary metal-oxide-semiconductor (CMOS) read-out integrated circuit (ROIC). The detector array consists of 128 × 128 pixels with a pitch of 60 μm, a pixel height of 50 μm, and an anti-reflective (AR) coating to improve short wavelength response [71].

The SCM1250 ROIC was chosen for this device because of its proven tolerance to radiation [72]. An output amplifier is used to read the signal from one row of pixels while the output of the next row is placed into a pipeline architecture via a source follower amplifier [71]. Three separate clocks control the ROIC readout: a master clock, a synchronization clock, and a frame synchronization clock. The frame synchronization clock allows for variation of the integration time. Figure 25 shows a functional block diagram of the signal chain.

Testing Details

Proton radiation studies were performed at Crocker Nuclear Laboratory (CNL) of the University of California, Davis (UC Davis). Proton fluxes up to 3.13×10^{10}

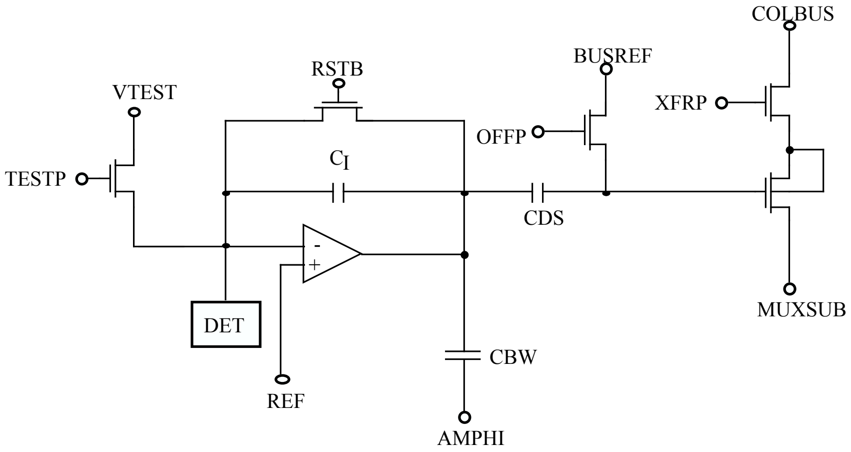

Figure 25: Functional block diagram of ROIC signal chain [71].

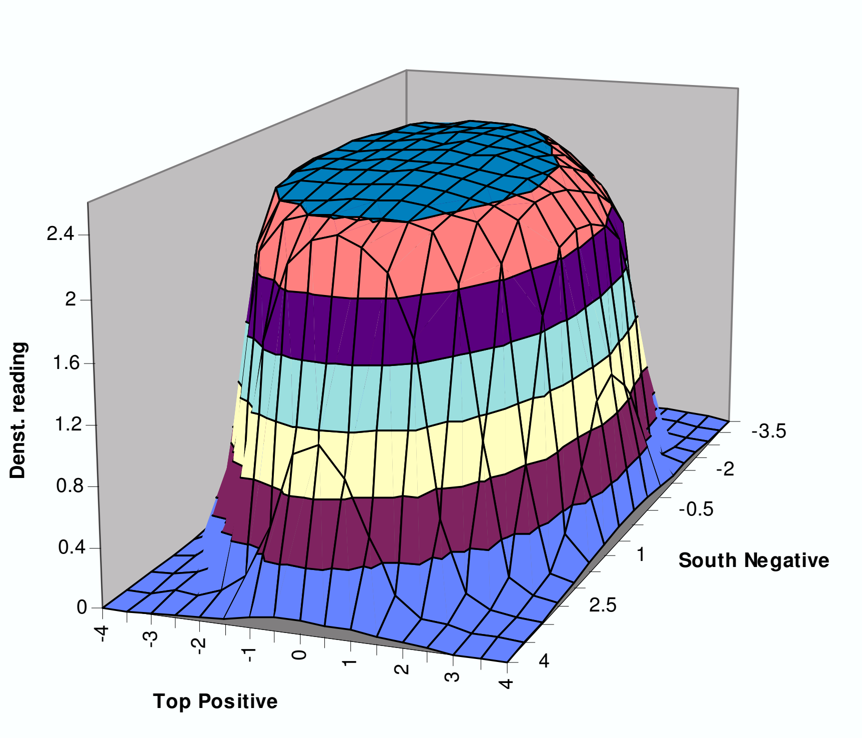

Figure 26: Spatial distribution of the proton beam output at CNL [73].

p/(cm^2-s) and energies from 1.25 to 68 MeV are available at CNL [73], [74]. The beam size is 2.75 inches in diameter. The spatial distribution of the proton beam output is in Figure 26.

Full radiometric characterizations were performed at each dose to determine the impact of the radiation on dark current, noise, responsivity, sensitivity, and dynamic range both pre and post irradiation [71]. The total ionizing dose response of this array has been described in [71]. This document focuses on the proton transient data.

The devices were irradiated with low flux levels to obtain sparse hit rates with 63 MeV protons at an angle of 45°. The low flux levels decrease the chances of a single pixel being struck multiple times during the experiment [75]. The silicon PIN detectors were biased to 15 V resulting in full depletion, and exposures were carried out at 233 K. Protons were incident on the silicon detector and then passed through the ROIC.

Pixel outputs for 25 frames of data were collected at a fluence of 1.7×10^5 p/(cm^2-s) with an integration time of 10.18 ms. Data were collected prior to irradiation to establish a baseline voltage for each pixel, referred to as clear frame data. After irradiation, data were collected again, referred to as irradiated data, and the pixels reset. This procedure was repeated for each of the 25 frames of data taken.

Data Reduction

To determine the effects of the proton irradiation on the FPA, it is necessary to subtract the clear data from the irradiated data for each pixel and each frame. The basic equation is

$$Raw\_Data_{n,m} = (Irradiated\_Data_{n,m}) - (Clear\_Data_{n,m}) \tag{2}$$

where n is the pixel number and m is the frame. After the subtraction is completed using Equation 2, the result is $n \times m$ data points. For the FPA in this document, the result is 16384×25 data points, or 409,600 data points. However, the actual number of data points is slightly lower. Some pixel values were not included in the data set. This includes the first four rows of pixels around the entire structure. These pixels are known to be noisy and therefore their outputs are unpredictable and inconsistent.

The $Raw\_Data_{n,m}$ is in microvolts after the subtraction is complete. In order to compare this to the MRED simulations, the data are histogrammed and converted to MeV by the following equation

$$Data_{n,m} = \frac{Raw\_Data_{n,m} \times E_{ehPair}}{C_g} \tag{3}$$

where C_g is 0.63 μV/electron, the conversion gain of the experiment, and E_{ehPair} is 3.6 eV, the amount of energy needed to create an electron-hole pair in silicon.

The conversion gain of a FPA is the transfer function between the integrated pixel current and the output voltage. The DC current method was used to determine the conversion gain during the experiment. To determine this value, the total current flowing in the detector common node (Eq. 4) and the median pixel output voltage (Eq. 5) are measured for several photon irradiance levels:

$$I_{total} = N_p(e\eta E_q A_{det} + I_{dark}) \tag{4}$$

$$V_{output} = C_g(\eta E_q A_{det}\tau_{int} + \frac{I_{dark}\tau_{int}}{q} + V_{offset} \tag{5}$$

where N_p is the number of pixels in the array, e is the mathematical constant, η is the quantum efficiency (electrons/photon), E_q is the photon irradiance (ph/s-cm^2), A_{det} is the detector area (cm^2), I_{dark} is the total pixel dark current (amps), τ_{int} is the integration time (s), q is the electronic charge (C), and V_{offset} is the multiplexer DC output voltage (v)[72].

Rearranging Equations 4 and 5 gives

$$I_{total} = (\frac{qN}{C_g \tau_{int}}) V_{output} \tag{6}$$

$$V_{output} = (\frac{C_g \tau_{int}}{qN}) I_{total} \tag{7}$$

When the output voltage is plotted as a function of the measured current, the slope of the straight line is used to determine the conversion gain. The resulting conversion gain is an average for the entire pixel array [72].

Results of Experiment

Figure 27 shows the average voltage of individual pixels in the clear data frames and the corresponding error bars (only every 20th pixel is shown to make the data points visible). The error bars (one standard deviation) are small on each pixel, showing that there was very little deviation between each frame of data. Therefore, during the experiment, the pixels remained free from defects, and each of the 25 frames of clear and irradiated data can be accepted as a new, unharmed experiment. For comparison, Figure 28 shows the average voltage of individual pixels in the irradiated data frames and the corresponding errors bars. Note here that the error bars are larger on some pixels, indicating that this pixel was struck during at least one of the 25 frames averaged. Also, note in Figures 27 and 28 that there is a pattern of decreased voltage across the pixel array. This voltage drop is expected and not related to the irradiation or experiment. It is simply an artifact of the FPA itself. Figure 29 shows a histogram of the clear and irradiated data, averaged over 25 frames.

Figure 30 shows a single frame of clear data in array format. There are a couple of

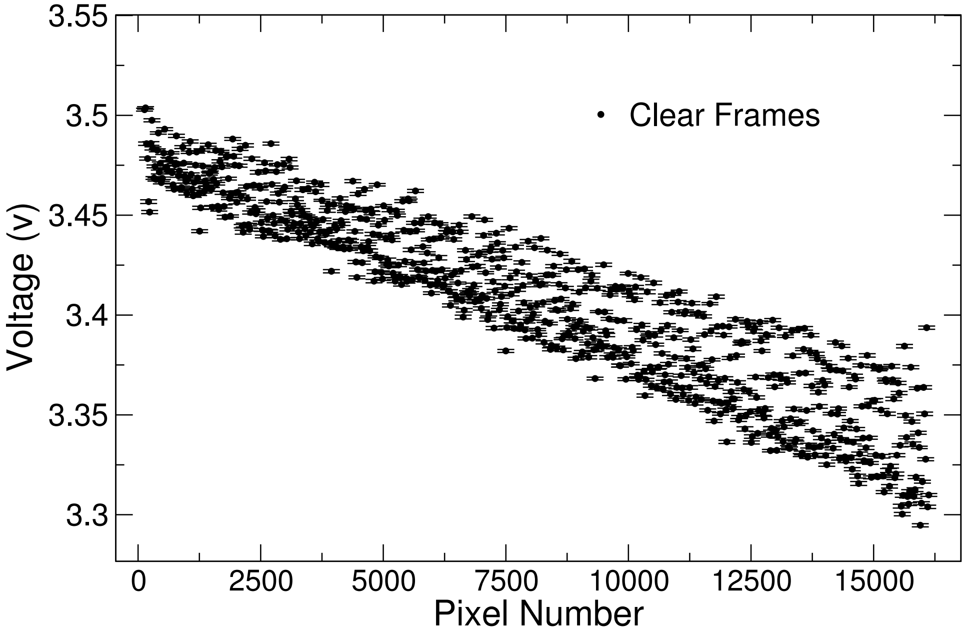

Figure 27: Average voltage of each pixel in the 25 clear frames and error bars showing the deviation over these frames. The deviation seen for individual pixels is low, showing that no permanent damage was done to each pixel during irradiation. Note that only every 20th pixel is shown on this graph so the data points are visible.

pixel clusters that appear to have a higher voltage than the surrounding pixels. This indicates a defect in these pixels. However, since this is detected in the clear frame data, it does not affect the result of the experiment because the defects are removed during the subtraction. The same defects are seen in Figure 31, which shows a single frame of pixel data taken after the proton irradiation. Notice also that Figure 31 has several spots within it that appear more yellow. These yellow spots indicate locations where the voltage has changed due to the irradiation and energy deposition within that pixel.

Figure 32 shows the result of the subtraction for a single frame of data, the same frames that were used in Figures 30 and 31. By doing the subtraction, the change in voltage is shown, and therefore the true effects of the protons are seen. Pixels with a

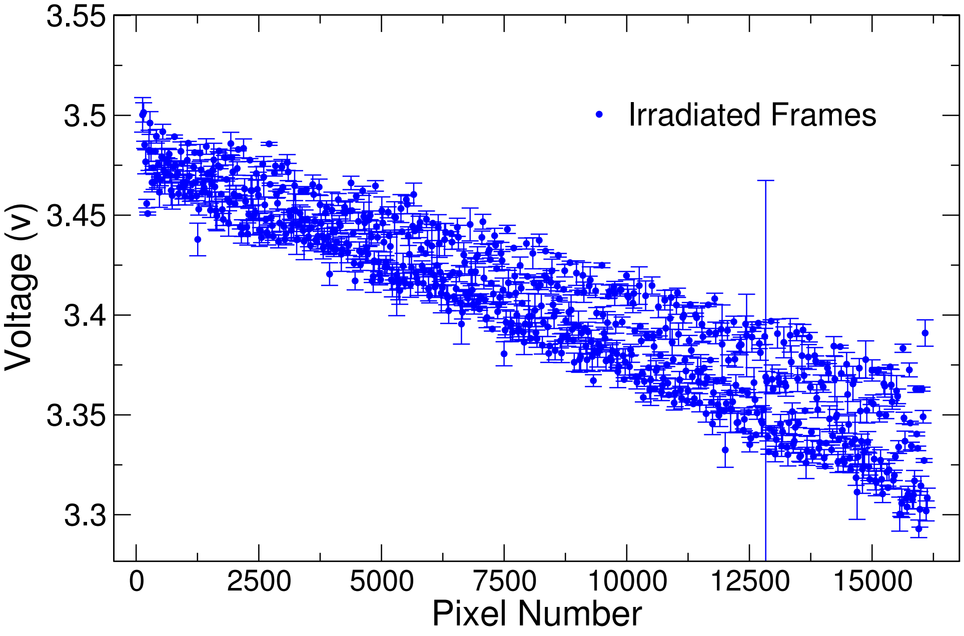

Figure 28: Average voltage of each pixel in the 25 irradiated frames and error bars showing the deviation over these frames. The deviation in voltage for individual pixels is larger than the clear frame averages, showing that many pixels were struck during irradiation. The pixel with the large standard deviation is one that was struck during two different frames so the voltage fluctuation across frames in this pixel is quite large. Note that only every 20th pixel is shown on this graph so the data points are visible.

defect are essentially filtered from the data, and the spots seen in Figure 32 indicate locations where a pixel received charge, either from a proton strike or a secondary event.

Figure 33 shows a histogram of the results of this subtraction. There is an approximately Gaussian broadening of pixels in the zero energy deposition range that represents the amount of system noise present, shown closer in figure 33(b). This peak is due to systematic noise and is not a result of the irradiation.

One way to handle data analysis of this noise is to “scrub” the data and remove pixels exhibiting saturated readings, those with consistently erratic readings, or ones struck across multiple frames [75]. Once these pixels are identified, they are excluded

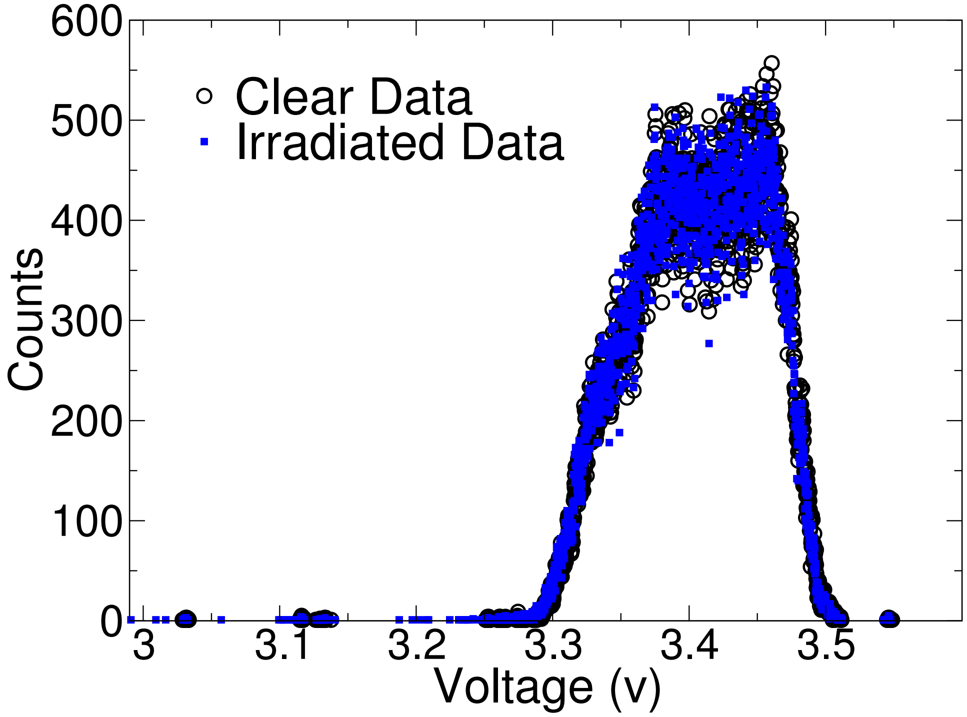

Figure 29: Histogram of the average voltage for each pixel over 25 frames of the clear and irradiated data.

from the data analysis. In the work presented here, the background noise was not removed. Instead, the simulation was post-processed to reflect this noise. This is described in the next section.

Recognizing Bad Data

Analyzing data using several different methods is extremely important to understand the data and determine the accuracy of the experiment. A good demonstration of this necessity is observed in Figure 34. Here, a set of data on a FPA is shown that was taken incorrectly. After looking at the data in this format, it was revealed that, when the data were collected during the experiment, every fourth pixel was read out. Therefore, the data appear to be in four "sections." If the data had not been

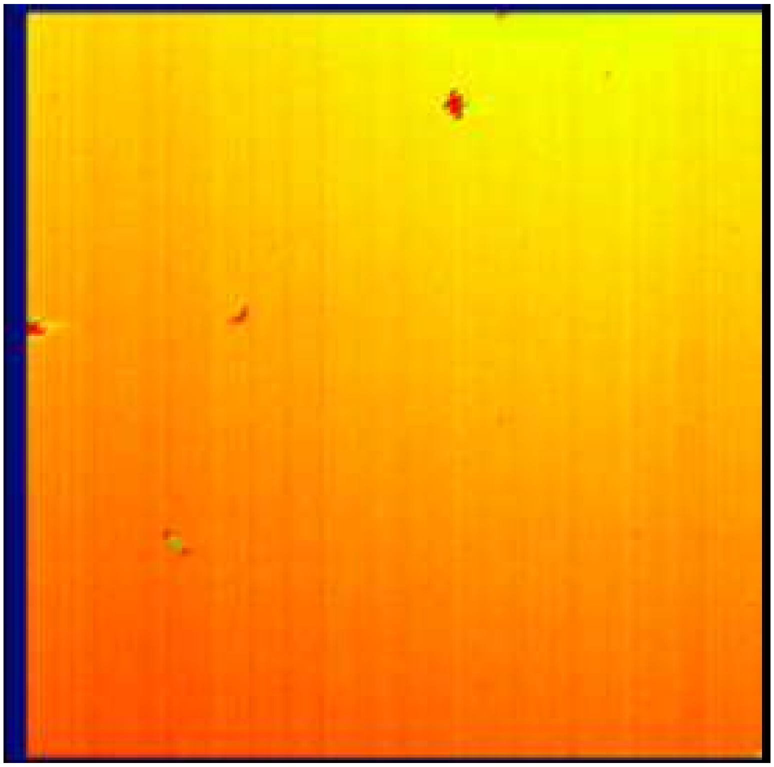

Figure 30: A single frame of clear data showing pixels that appear to have a slight defect.

analyzed in this way, the mistake may have been overlooked.

Modeling

Pileup

Each event in the Monte Carlo simulation represents one, and only one, primary particle. For finite integration times, there is a small but non-negligible probability of multiple hits on a single pixel (pile-up). In other words, while the data are being read by the ROIC, a particle could strike a pixel that was previously struck by a different ion. To account for this, a correction is applied. It is a very general transformation of an arbitrary single-particle spectrum for the case in which the average number of hits

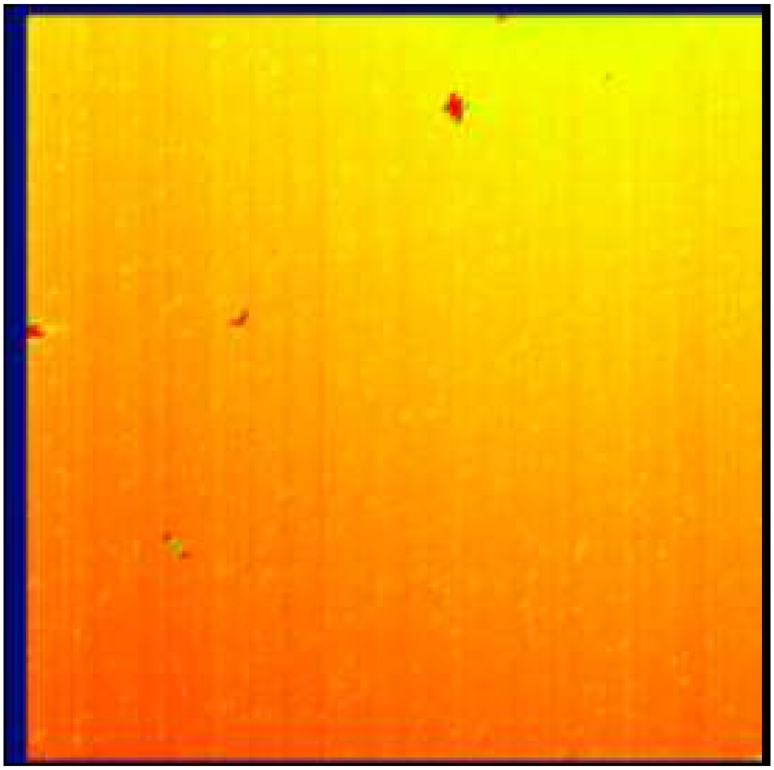

Figure 31: A single frame of irradiated data showing the same pixels that appeared to have a slight defect in Figure 30 are still present after irradiation. Also seen here are yellow dots within the FPA that indicate where a proton strike has likely occurred.

per pixel is μ and similar to that described in [76]. The transformation inherently includes multiple hits of all orders, and can be used without numerical difficulty from very low fluxes well into the photon-counting region, where tens or hundreds of particles can hit a pixel in a single integration period.

To account for pile-up, a non-adjustable parameter is used in a fast Fourier transform (FFT) during post processing of the MRED simulations. This parameter is μ, the mean number of protons hits per pixel during a single integration time, and is computed by Equation 8:

$$\mu = \sigma_{sim} \phi \tau_{int} \tag{8}$$

where σ_{sim} is the integral cross section of the simulation, ϕ is the experimental flux,

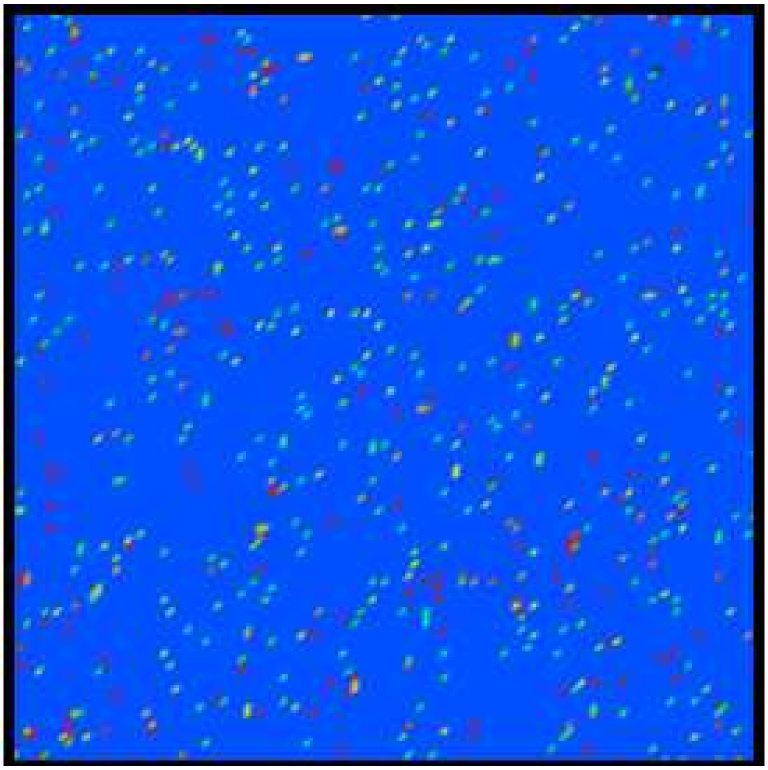

Figure 32: A single frame of experimental data showing the result of proton strikes. The clear frame data has been subtracted from the irradiated data in this figure.

and τ_{int} is the experimental integration time. The second non-adjustable parameter is the addition of the non radiation induced noise observed in the experimental data, as shown in 33(b). This is added to the simulation results by convolution. The python script that performs the pile-up routine was written by Dr. Robert Weller at Vanderbilt University, and is shown in Appendix A.

Figure 35 compares the differential spectrum of MRED simulations before and after the effects of pile-up and the non-radiation induced noise were included in post-processing of the data. The shape of the sloped region between 125 and 500 keV is affected by the finite number of pixels that receive multiple hits during one integration period. The region of very low energy is affected by the addition of the observed system noise.

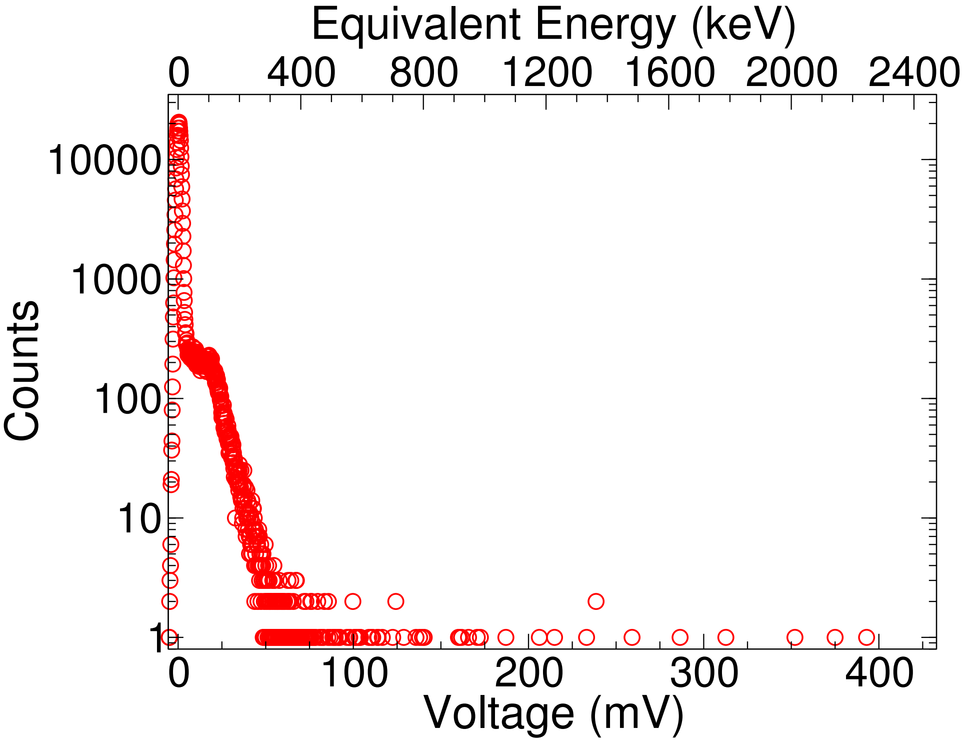

(a)

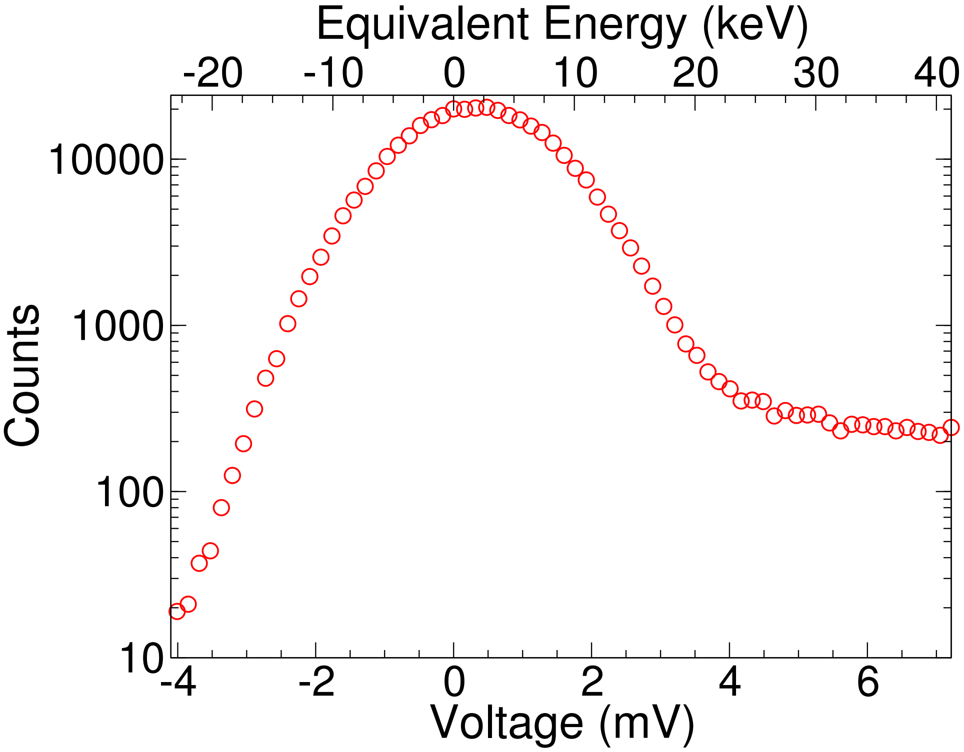

(b)

Figure 33: (a) Histogram of raw experimental data. (b) Zoomed in to show the noise region. This noise comes from the system and is not non-radiation induced.

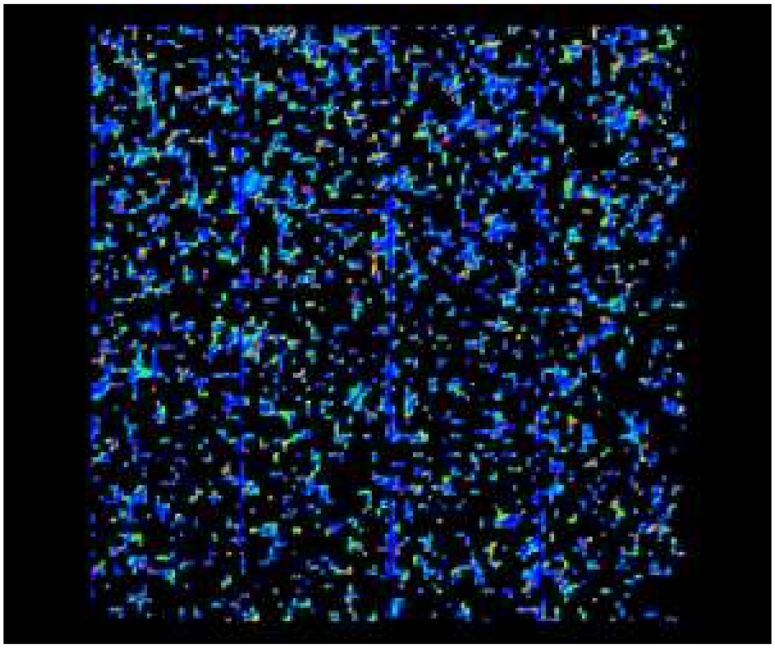

Figure 34: A single frame of experimental data showing four “sections” revealing there is an issue with the data. During this experiment, data were collected only for every fourth pixel instead of every pixel.

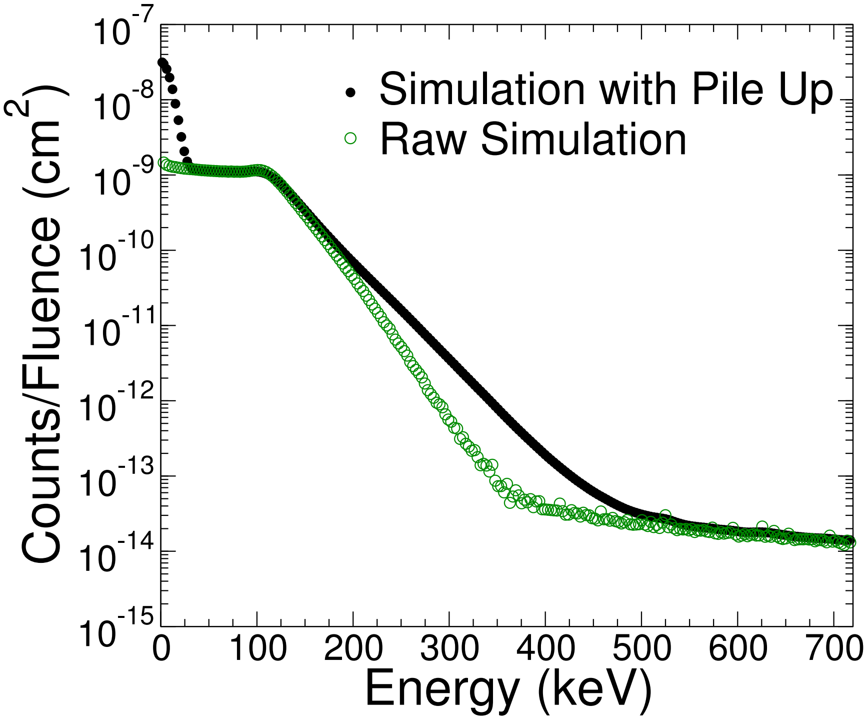

Figure 35: MRED simulations before and after the effects of pileup and non-radiation induced noise are applied.

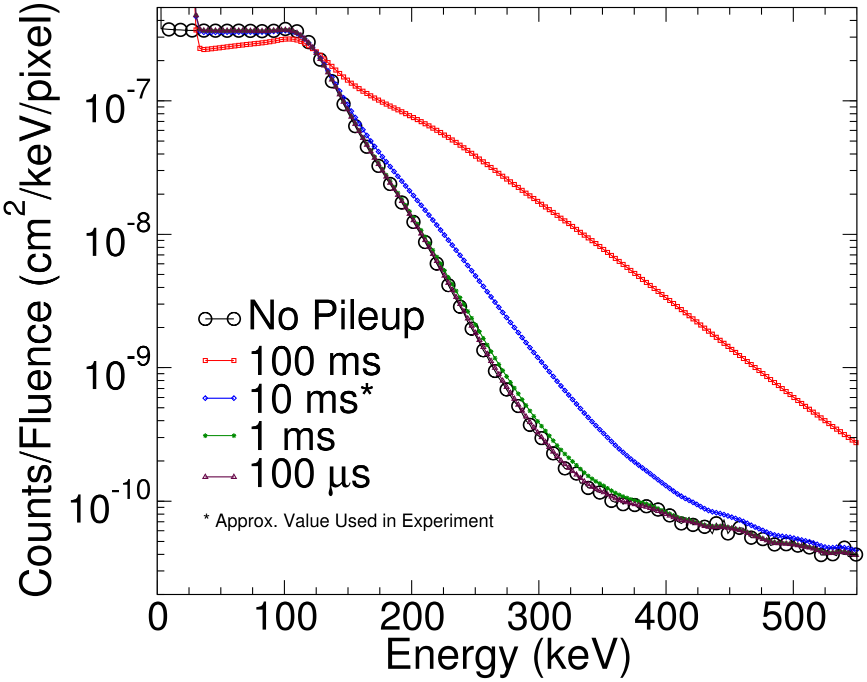

Figure 36: MRED simulations showing the effects of pile-up for varying integration times. By 1 μs the shift is negligible.

For very short integration times, pile-up can become nearly negligible. Figure 36 shows how the curve is affected by various integration times. At an integration time of 1 ms, pile-up causes only a slight shift in the curve, and by 1 μs the shift is not visible.

TCAD Simulations

TCAD simulations were conducted on two adjacent pixels to determine the amount of charge motion between them. The structure is shown in Figure 37. Charge transport and collection within the device was simulated for various strike locations from a 63 MeV proton incident at 45°. Using TCAD to simulate the amount of charge moving between pixels helps to determine the complexity of the structure necessary in MRED. If the pixels remain isolated, then simulating a single pixel in MRED should

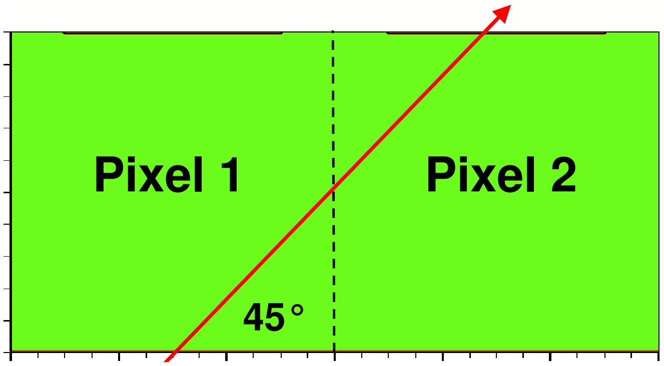

Figure 37: TCAD structure representing two pixels. Simulations include detailed device parameters.

be sufficient to capture the effects of radiation transport in the device. However, if the pixels show charge motion between them, a multiple pixel structure will be necessary for the MRED simulations.

Calculating Expected Charge

For each strike location, the amount of charge collected in TCAD is compared to the expected value. The expected collected charge was calculated using a rectangular parallelepiped (RPP) approximation of pathlength and dE/dx, as shown in Equation 9.

$$Collected\_Charge = dE/dx \times Pathlength \tag{9}$$

The dE/dx of 63 MeV protons in silicon was calculated using MRED and cross referenced with SRIM [35] and *A Physicist's Desk Reference* by H. L. Anderson [77]. Using MRED, simulations including direct ionization only of 63 MeV protons on a pure silicon structure of size 100 μm $\times$100 μm $\times$10 μm were performed. The protons were normally incident on the 100 μm $\times$100 μm face and all particles were simulated through the center of the structure as shown in Figure 38. The dE/dx in keV/μm

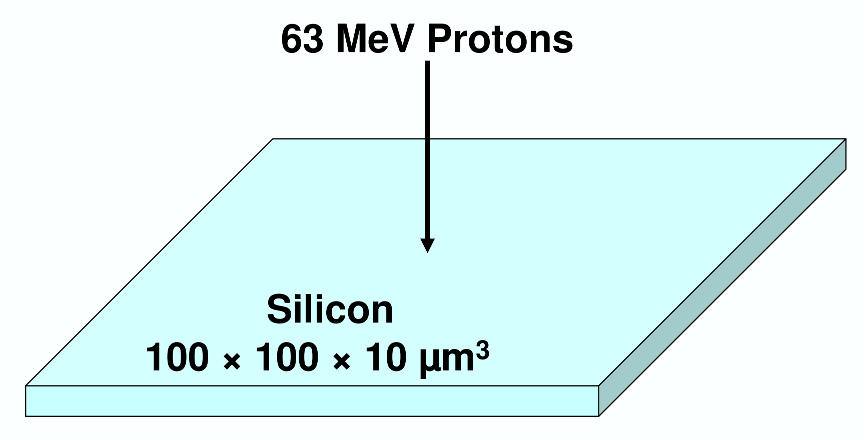

Figure 38: MRED structure used in the calculation of the dE/dx.

was extracted from the simulations by Equation 10.

$$dE/dx = \frac{\frac{\sum_{i=0}^{n} E \times c}{\sum_{i=0}^{n} c}}{t_{struct}} \tag{10}$$

where n is the number of bins, E is the energy of the ith bin, c is the counts of the ith bin, and t_{struct} is the thickness of the structure (10 μm).

The dE/dx was calculated for several different MRED runs, including varying values of range cuts and different physics lists (explained in Chapter 2). The resulting dE/dx values are listed in table 2, and shown graphically in figure 39. The values obtained from the MRED simulations were averaged to a value of 1.76 keV/μm. SRIM calculates the dE/dx of 63 MeV protons in silicon to be 1.92 keV/μm [35], and Anderson reports a value of approximately 1.86 keV/μm through experiment [77]. The difference between the experimentally reported dE/dx and the value calculated using MRED is approximately 5%.

A dE/dx of 1.76 keV/μm translates to a LET of 7.57 $\times$ 10^{-3} MeV-cm^2/mg. To convert dE/dx to LET, Equation 11 is used:

$$LET = \frac{dE/dx}{Density} \tag{11}$$

Table 2: Calculated values of dE/dx (keV/μm) using MRED for various physics lists and range cuts.

Physics List / Range Cuts	0.5 μm	1.5 μm	5 μm	10 μm	15 μm
Standard Screened	1.76	1.75	1.75	1.77	1.78
Penelope	1.75	1.74	1.74	1.76	1.78
EM Low	1.74	1.74	1.74	1.76	1.78

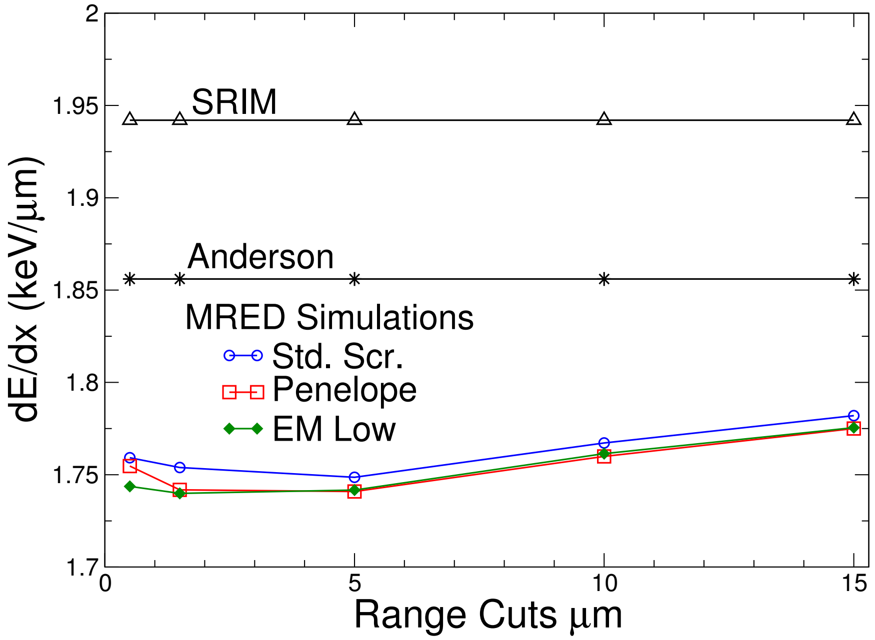

Figure 39: Values of dE/dx from 63 MeV protons in silicon from MRED simulations, SRIM [35], and Anderson [77].

Results

The strike locations in the TCAD simulations are shown in Figure 40. The results of the TCAD simulations and the RPP approximation for each strike location are shown in Figure 41. The strike labeled (a) is contained entirely within pixel 1. For this strike, based on the pathlength and dE/dx calculation, pixel 1 should collect 5.8 fC and pixel 2 should collect no charge. TCAD results show that pixel 2 does indeed collect no charge, however, pixel 1 collects only 5.2 fC. This result indicates that the pixels do not collect all the charge generated within them.

For strike locations (b) and (c), the strike spans both pixel 1 and 2. In both cases less charge is collected on pixel 1 than expected, but more charge than expected is collected on pixel 2. This indicates that there is charge moving between the two pixels. Some of the charge expected to be collected on pixel 1 moved laterally to pixel 2 and was collected there. Strike location (d) spans pixel 2 only, but is right on the edge of pixel 1. Once again, some charge motion to pixel 1 is seen and more charge than expected is collected.

For strike locations (e) and (f), slightly less charge than expected is collected on pixel 2; however, no charge is collected on pixel 1, indicating that when charge moves from one pixel to another, it moves in the direction of the strike. The charge that is expected, but not collected on pixel 2 for strike locations (e) and (f) would be collected on the next adjacent pixel if simulated. In general, for each strike location, approximately 10% less charge was collected on the pixel taking the initial strike, and 10% more charge than expected was collected on the neighboring pixel, as shown in Figure 41.

The motions of electrons and holes can be seen in Figures 42 and 43. Note how the electrons and holes move not only vertically, but along the charge strike as well. This correlates with the results shown in Figure 41 where strikes contained within pixel 1 affected pixel 2, but when the strike was contained in pixel 2 it did not affect pixel 1. This shows that the strike can become a temporary conducting path, causing more charge to collect on the adjacent pixel, as noted above. If the pixels were completely isolated from one another, charge would move only vertically.

Figure 44 shows the electric field after a strike that spans two pixels equally.

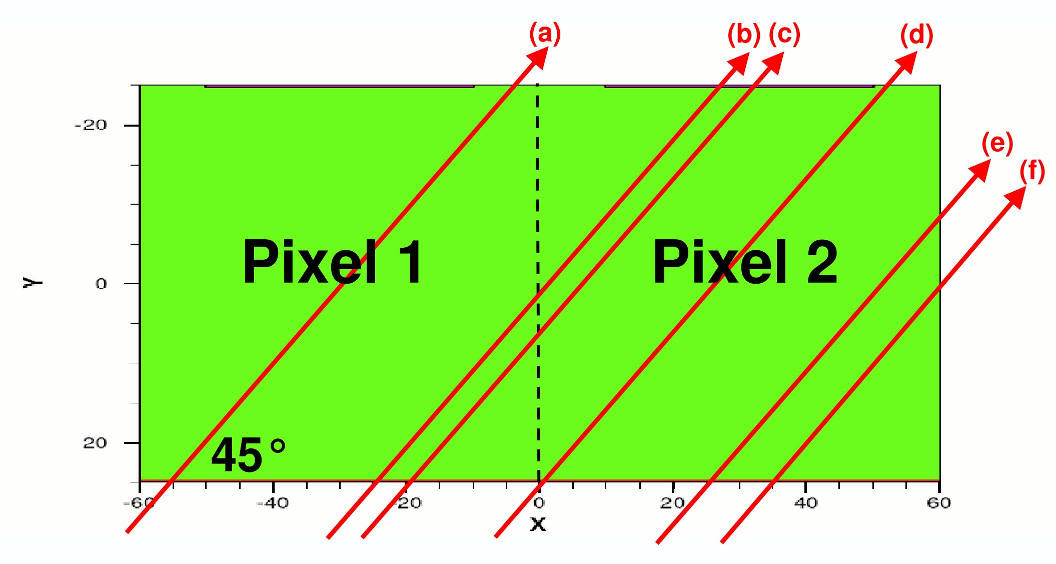

Figure 40: TCAD simulation strike locations of two adjacent pixels. Strike (a) spans only pixel 1, strike (b) and (c) span pixels 1 and 2, and strikes (d), (e), and (f) span only pixel 2.

There is a slight disturbance in the electric field where the two pixels meet, but, for the most part, they stay relatively isolated. Figure 45 shows the electrostatic potential. It is likewise only slightly disturbed, but it is minimal and will restore quickly to equilibrium.

Since the motion of charge between pixels is at maximum 10%, it suggests that a RPP assumption is sufficient to estimate the device response for this technology. Therefore in the MRED simulations, a single pixel structure is expected to capture the effects of protons on the pixel array. However, as the next chapter will show, a single pixel does not capture the full effect.

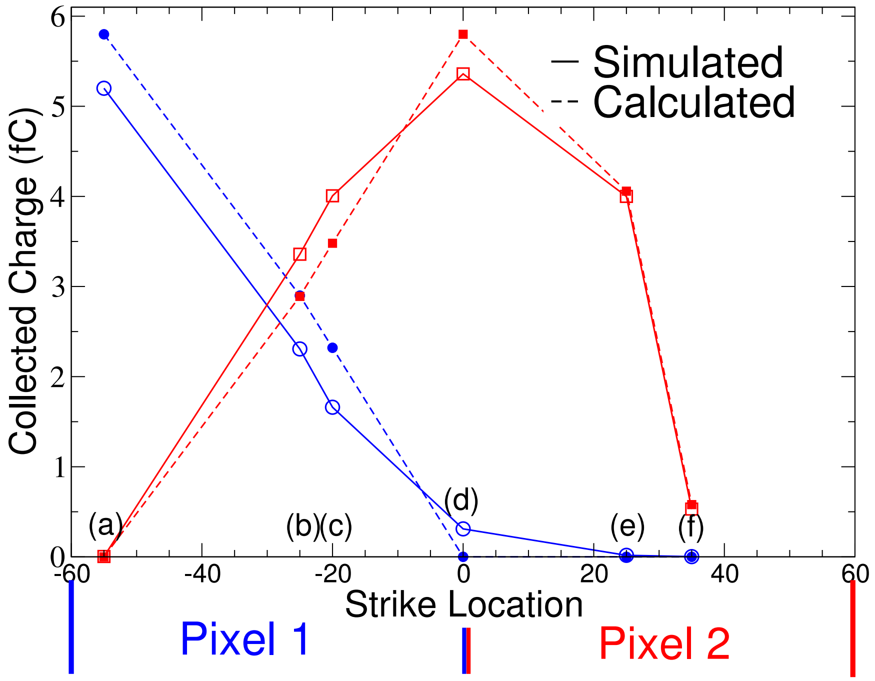

Figure 41: Amount of collected charge simulated by TCAD compared with the expected charge using a RPP approximation for various strike locations. In general, approximately 10% less charge was collected on the pixel taking the initial strike, and 10% more charge than expected was collected on the other pixel.

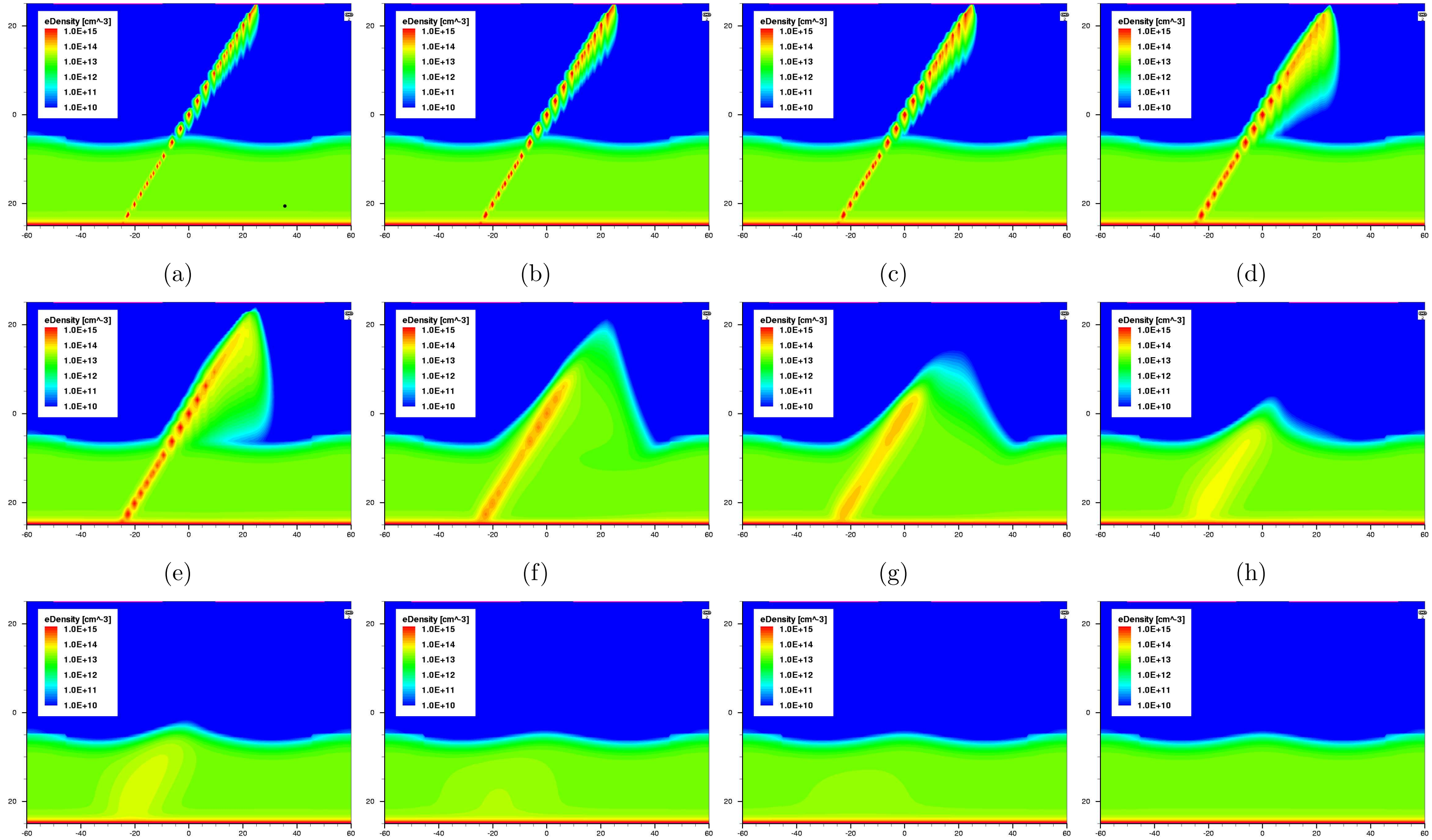

(a) (b) (c) (d)

(e) (f) (g) (h)

(i) (j) (k) (l)

Figure 42: Electron density at (a.) initial strike time and then (b.) 4 ps, (c.) 8 ps, (d.) 30 ps, (e.) 70 ps, (f.) 400 ps, (g.) 800 ps, (h.) 4 ns, (i.) 8 ns, (j.) 40 ns, (k.) 80 ns, and (l.) 400 ns after a strike that spans two pixels equally. The pixel on the left is referred to as pixel 1 and the pixel on the right pixel 2. The motion of electrons is not only vertical, but along the strike as well. The strike creates a temporary conducting path between the two pixels.

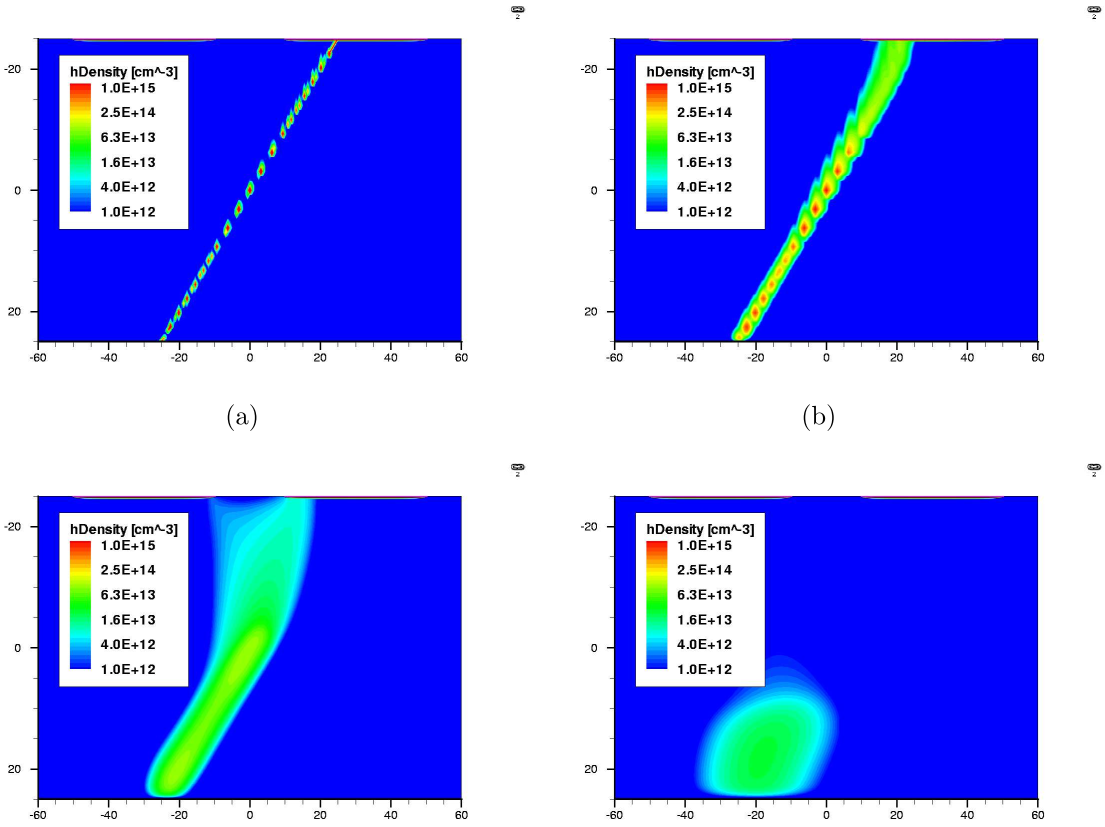

(a) (b)

(c) (d)

Figure 43: Hole density at (a.) initial strike time and then (b.) 90 ps, (c.) 900 ps, and (d.) 10 ns after a strike that spans two pixels equally. The motion of holes is not only vertical, but along the strike as well.

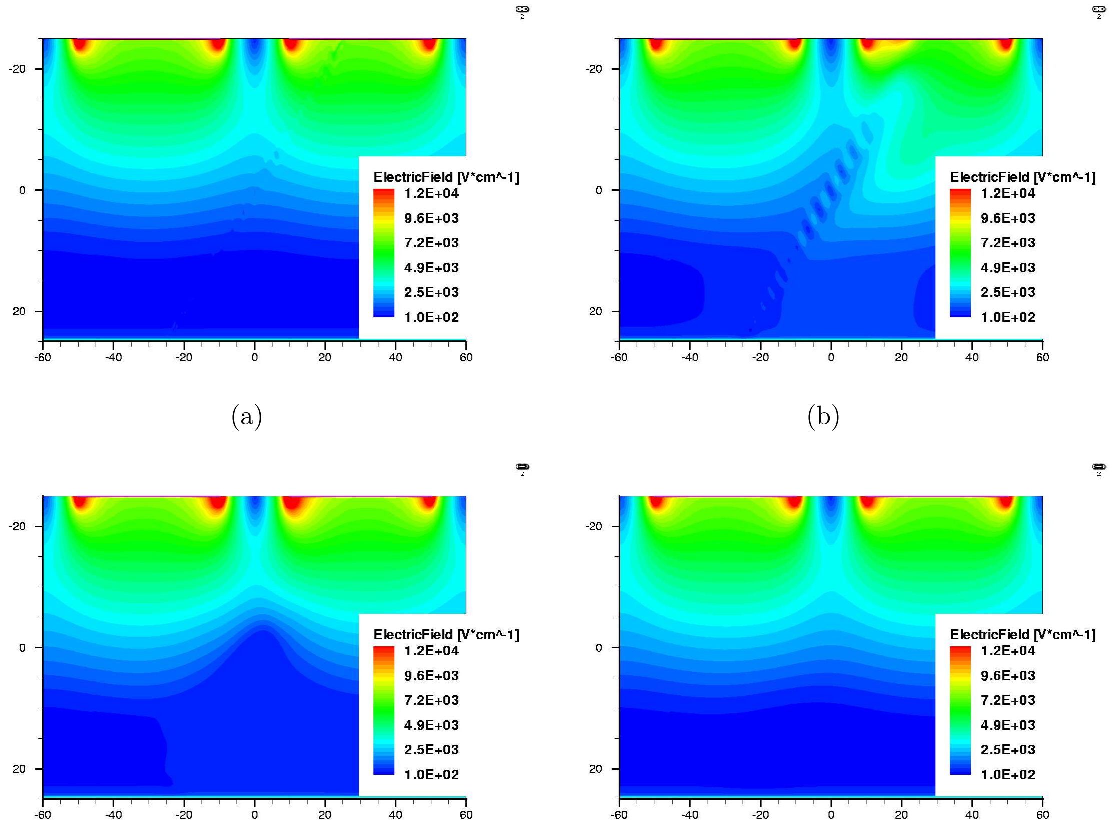

(a)

(b)

(c)

(d)

Figure 44: Electric field at (a.) initial strike time and then (b.) 90 ps, (c.) 900 ps, and (d.) 10 ns after a strike that spans two pixels equally. The electric field is only slightly perturbed and recovers quickly.

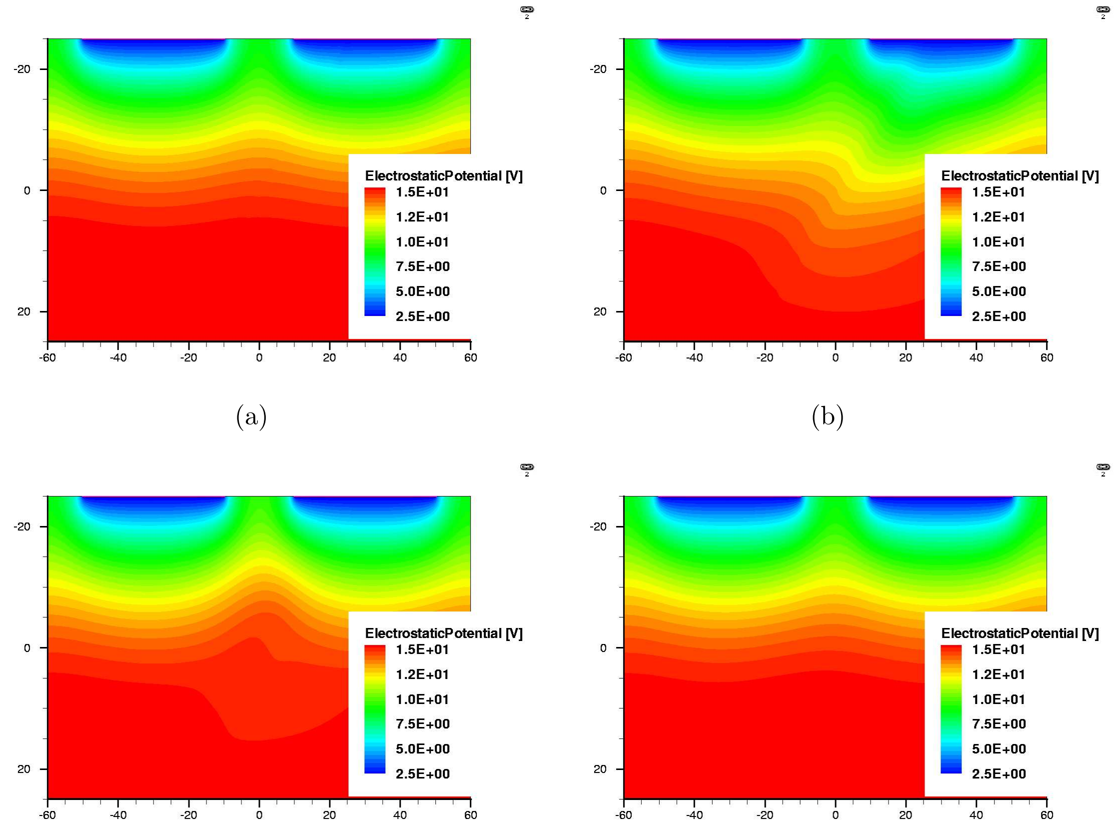

(a) (b)

(c) (d)

Figure 45: Electrostatic potential at (a.) initial strike time and then (b.) 90 ps, (c.) 900 ps, and (d.) 10 ns after a strike that spans two pixels equally. The potential is only slightly perturbed and recovers quickly.

CHAPTER V

RESULTS OF SILICON FPA MODELING

Structures

Simple Structure

The first structure is shown in Figure 46 and will be referred to as the simple structure throughout this document. The sensitive region of this structure is equal in size to one pixel of the FPA. The sensitive region corresponds to the region in which energy deposition must occur to produce a transient event. The top and bottom of the sensitive volume are flush with the top and bottom of the surrounding material, which is also silicon.

Based on TCAD simulations showing that adjacent pixels share no more than 10% of charge, this structure was assumed to be sufficient to model the FPA. This structure is very simple allowing MRED simulations to run very quickly. This structure was used as a first look at modeling the radiation response. As results show below, however, this structure was too simple to capture the full response of the FPA to 63 MeV protons.

Complex Structure

The structure in Figure 47 represents the full size of the focal plane array. Every pixel in the device is included in the simulation and treated as a sensitive volume. On top of the pixels is a very thin anti-reflective coating, and directly below the pixel

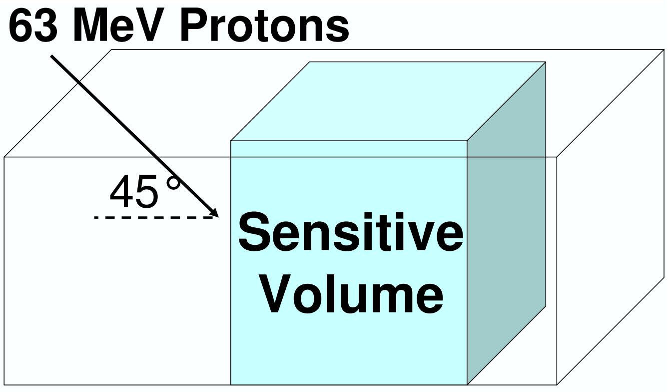

Figure 46: Structure used in [78], representing one pixel of a silicon PIN detector array. The entire structure is made of silicon and the shaded region is sensitive to the proton irradiation.

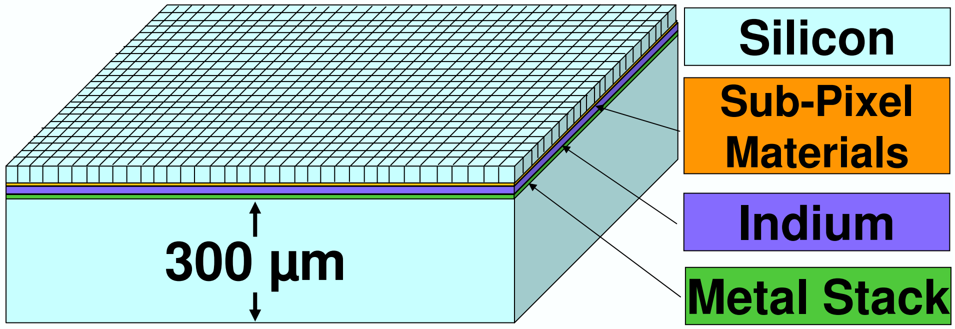

Figure 47: Complex FPA structure simulated using MRED. The structure includes all pixels in the array, and each of the 128 x 128 pixels is a sensitive volume. Below the pixel layer are layers of indium and metalization to represent the bumps and ROIC.

layer is a thin layer of metalization including titanium and nickel, 10 μm of indium, and a metal stack representative of the materials in a CMOS ROIC. The CMOS stack is shown in Figure 48. There is also a silicon substrate of 300 μm below the metal stack.

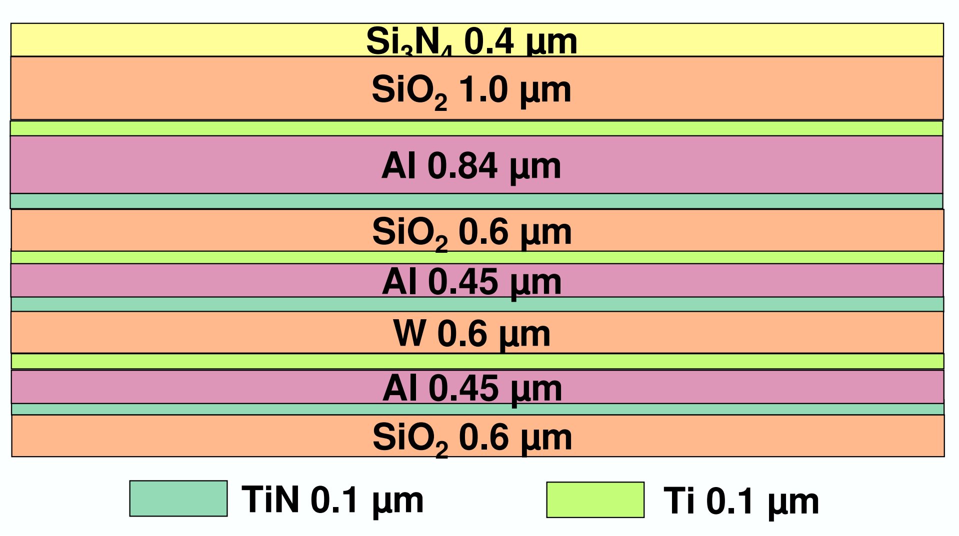

Figure 48: Details of the metal stack in Figure 47 representing the CMOS ROIC.

Complex Structure on Mount

In Figure 49, the FPA structure from Figure 47 is placed on a mounting, as done during experiment and simulated here. The mounting is 1 cm thick and three times greater than the size of the FPA laterally. Several different materials were considered for the mounting. Figure 50 compares raw MRED simulations on the structure for aluminum, beryllium, ceramic, copper, and tantalum mounts. Results showed the mounting material had little impact on the response of the device. An aluminum base was used for simulations throughout the rest of this document. The mounting was added to better capture the exact conditions of the experiment.

Results

This section shows the results of MRED simulations on the structures described above. Simulations mimic the experimental conditions by simulating protons incident at an angle of 45° with energy of 63 MeV.

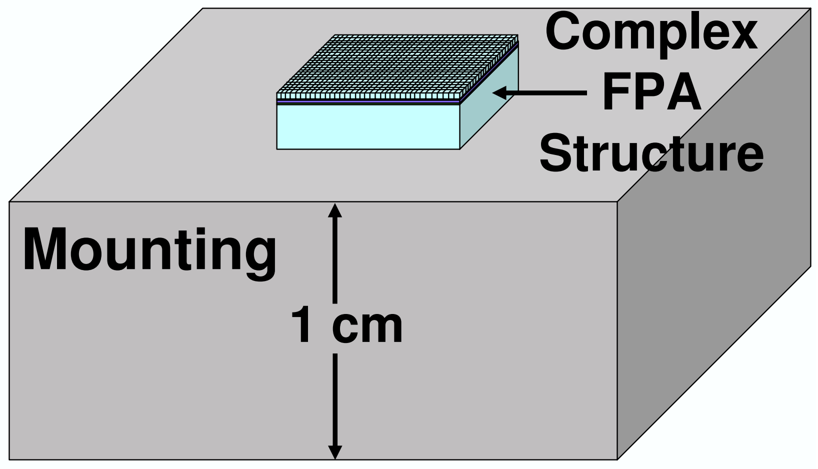

Figure 49: Complex FPA structure in Figure 47 on an aluminum mounting, as done in the dewar during the experiment.

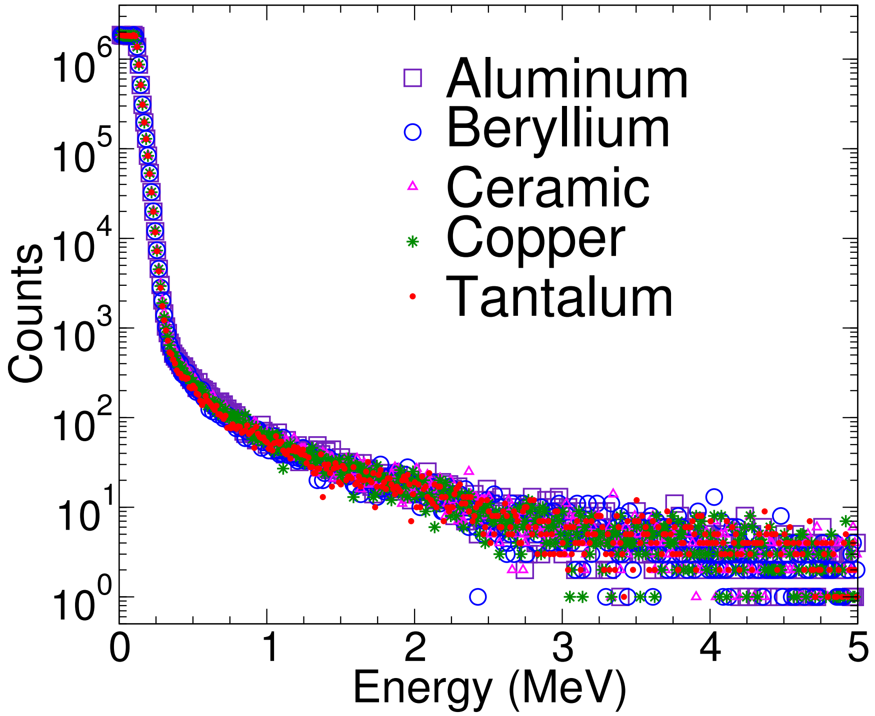

Figure 50: Raw MRED simulations comparing mount materials of aluminum, beryllium, ceramic, copper, and tantalum. Results showed the base material had little impact on the response the of device.

Comparison with Experimental Data

Figure 51 shows the results of simulations done with MRED, comparing simulation results of the structures shown in Figures 46, 47, and 49 with the experimental data. The simple structure, which consists only of one silicon pixel, fails to capture events contributing to the cross section above 300 keV. When underlying materials are added to the simulated structure, there is a significant increase in the cross section. This increase is due to secondary nuclear reaction fragments and multiply-scattered primary particles recoiling back toward the pixels.

When an aluminum mounting is added below the full pixel array and underlayers, as in Figure 49, the cross section increases even more in the region above 300 keV. There is an order of magnitude increase in the cross section when compared with the single pixel structure, and approximately a two-times increase when compared with the full pixel array simulations. This clearly shows the importance of layers below the device, even down to the mounting when the beam is obliquely incident.

The reason for the increase in cross section when underlying materials are added below the pixels can best be explained by visually examining the details of events. Figure 52 shows two events in the complex structure where energy is deposited into the pixel array and no secondaries affect the pixels. Both of these events fall in the lower energy range of Figure 51, where all three structures simulated result in roughly the same curve. In 52(a) the primary particle deposits some of its energy in a single pixel, and then passes through the device creating no secondary particles. The total energy deposited in this event is 106 keV. Figure 52(b) shows a similar event in that only the primary ion deposits energy into the pixel array, but here two pixels receive energy and a secondary electron is released in the underlayers.

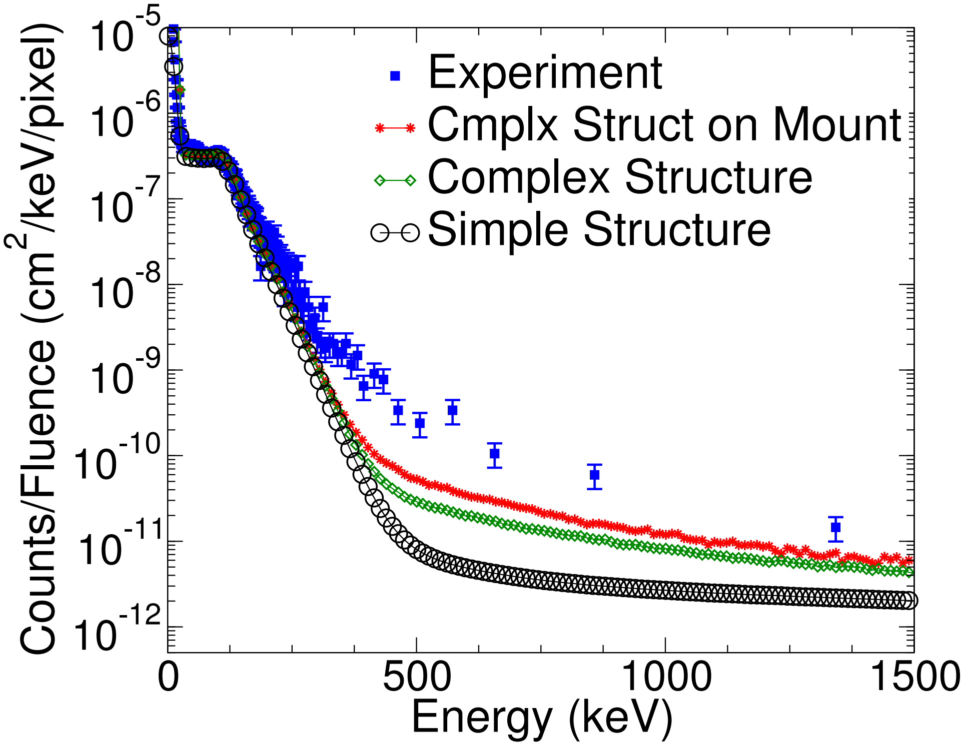

Figure 51: Differential spectrum of counts per unit fluence per pixel for 63 MeV protons incident on the focal plane array structure from Figures 46, 47, and 49 compared with experimental results.

In contrast to the events shown above, Figure 53(a) shows an event where the primary particle first deposits energy into the pixel array, and then a scattering event occurs in the silicon substrate below the pixels, causing a secondary proton and gammas to recoil back towards the pixel array depositing energy into an additional pixel. The total number of pixels affected in this event is three, and the total amount deposited in all three pixels is 658 keV. The pixels affected are mapped out in 53(b). This event clearly demonstrates why an increase in cross section is noted in Figure 51 when the underlayers are included in the simulation as well as all the pixels in the array. Another event of this type is shown in Figure 54 where six pixels were affected and a total of 3.24 MeV was deposited.

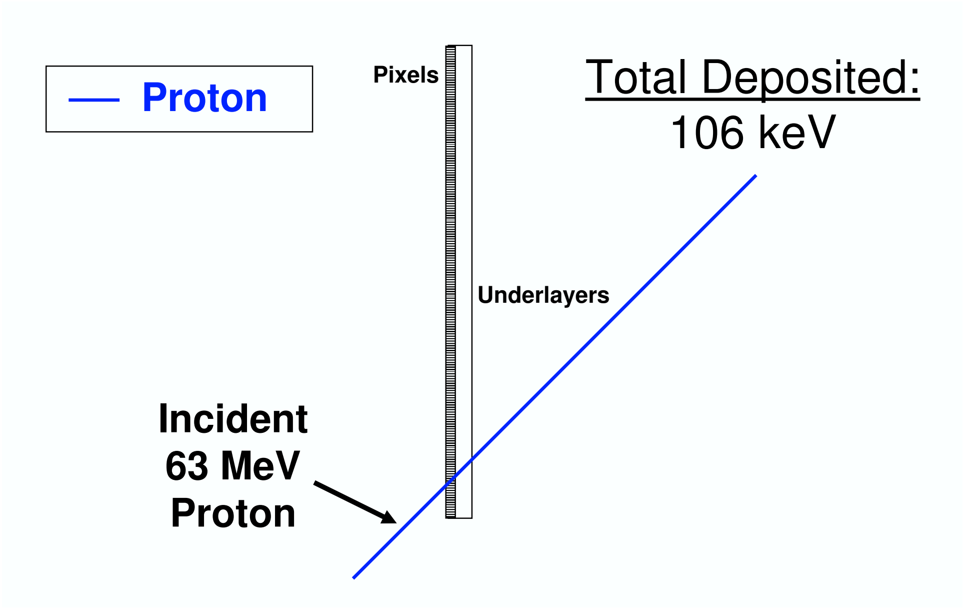

(a)

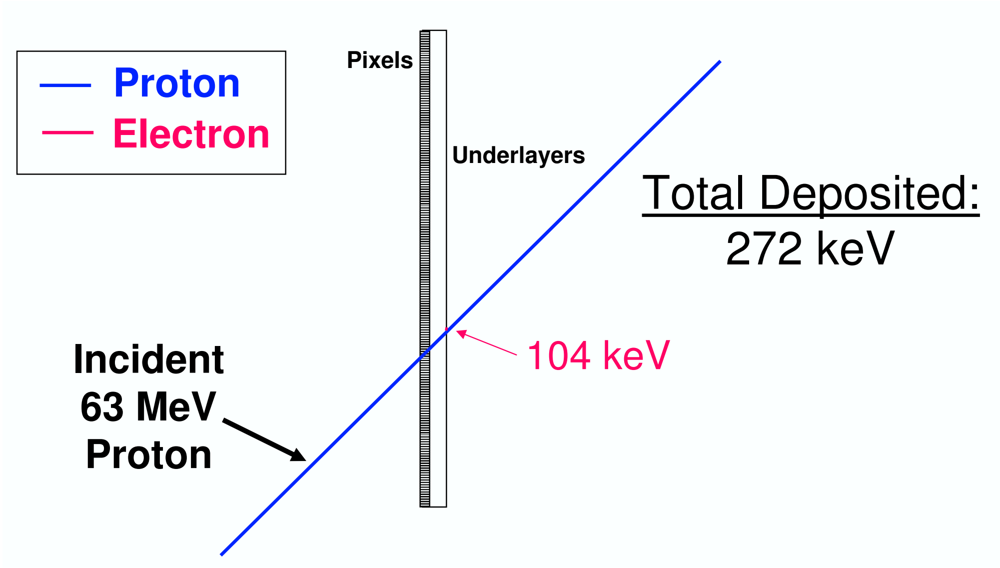

(b)

Figure 52: MRED event showing the incident proton depositing energy into (a) a single pixel in the structure and (b) two adjacent pixels in the structure from Figure 47. Here a secondary electron is released, but does not affect the pixel array

Figure 55 shows an event in the complex structure on an aluminum mount shown in Figure 49. Here the primary particle deposits energy into the pixel array, and then an event occurring in the aluminum mounting causes a secondary proton to deposit

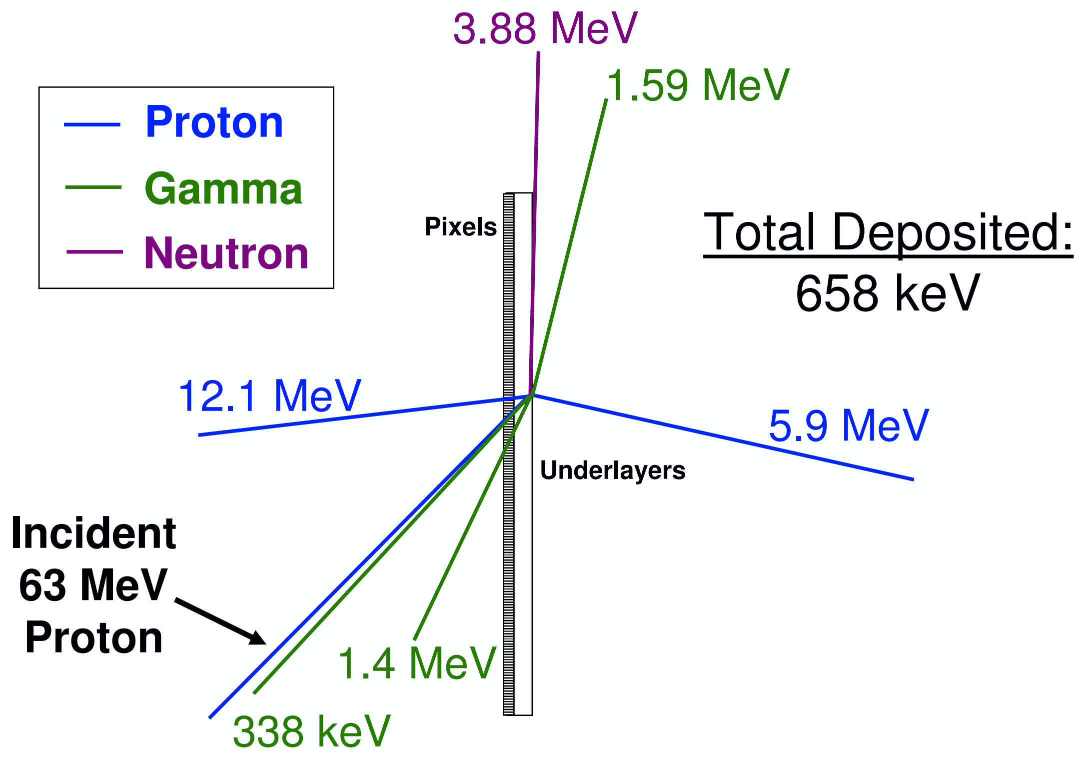

(a)

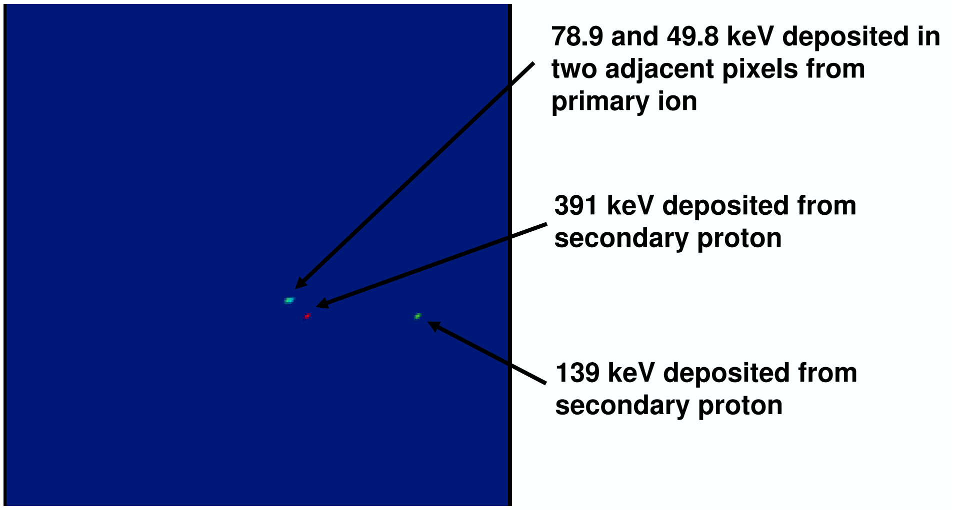

(b)

Figure 53: MRED event showing the incident proton depositing energy into two pixels, and then creating scattering events in the silicon substrate below the pixels. A secondary proton recoils back towards the array and subsequently deposits energy into one additional pixel of the array.

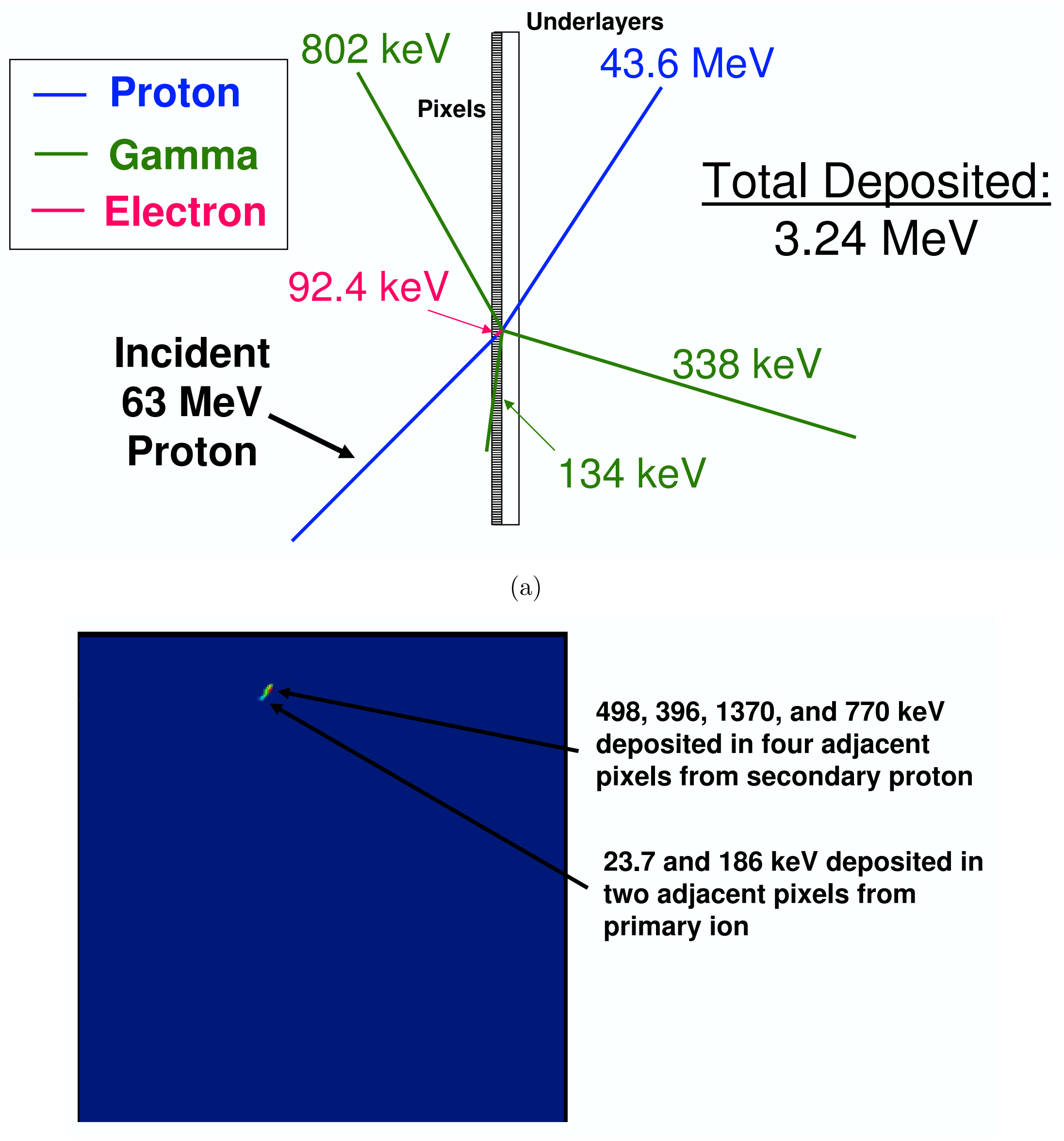

(a)

(b)

Figure 54: MRED event showing the incident proton depositing energy into two pixels in the array, and then creating scattering events in the silicon substrate below the pixels. A secondary proton then recoils back towards the array and deposits more energy into four additional pixels.

additional energy into the pixel array. This event demonstrates the importance of including the mount structure. The total energy deposited from this event is 836 keV in four pixels. Looking at Figure 51, this is the region of energy deposition where a large difference is seen between the various MRED structures.

The event shown in Figure 56 is particularly interesting because the primary ion does not deposit energy into the pixel array. However, a secondary proton produced in the aluminum mounting recoils towards the array depositing a total of 2.84 MeV in three pixels. Figure 57 shows another event occurring in the mounting. The interesting part of this event is the large number of recoils. There are 5 gammas, as well as an ^{26}Al ion, a positron, a neutron, and a neutrino. However, the particles that deposit energy into the pixel array include an electron and two secondary protons. They are released close to the array and are not visible on Figure 57(a) because of their small tracks.

In summary, the above MRED event images demonstrate how the incident proton causes a scattering event in layers beneath the pixels. The event releases a secondary particle(s), lower in energy than the incident particle, which then passes through pixels depositing energy. These secondaries are often at greater angles than the primary ion, causing them to pass through many pixels. The lower energy secondary protons deposit more energy than the primary 63 MeV proton because they are moving slower and have a higher LET. These scattering events result in an increase in the cross section, as shown in Figure 51.

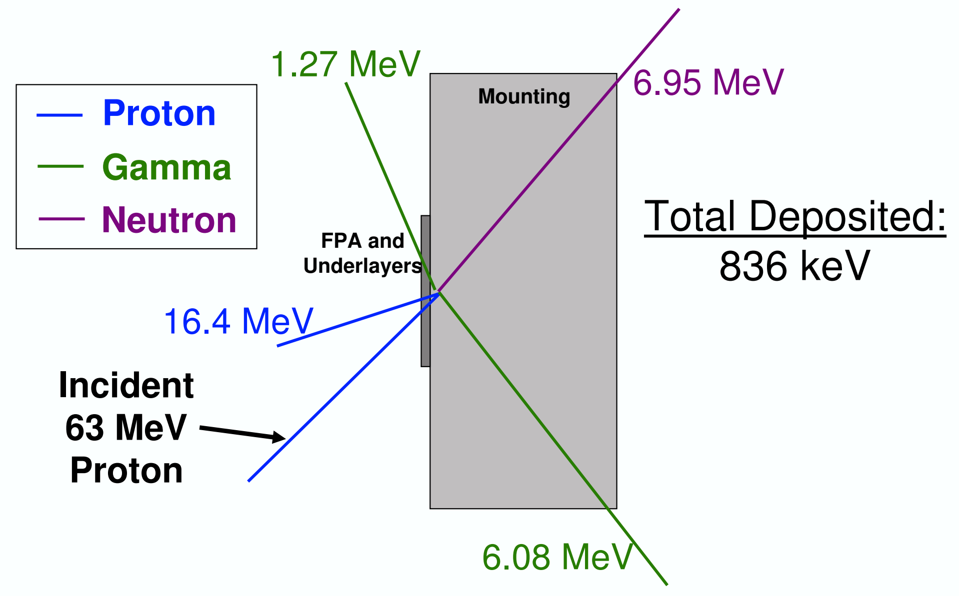

(a)

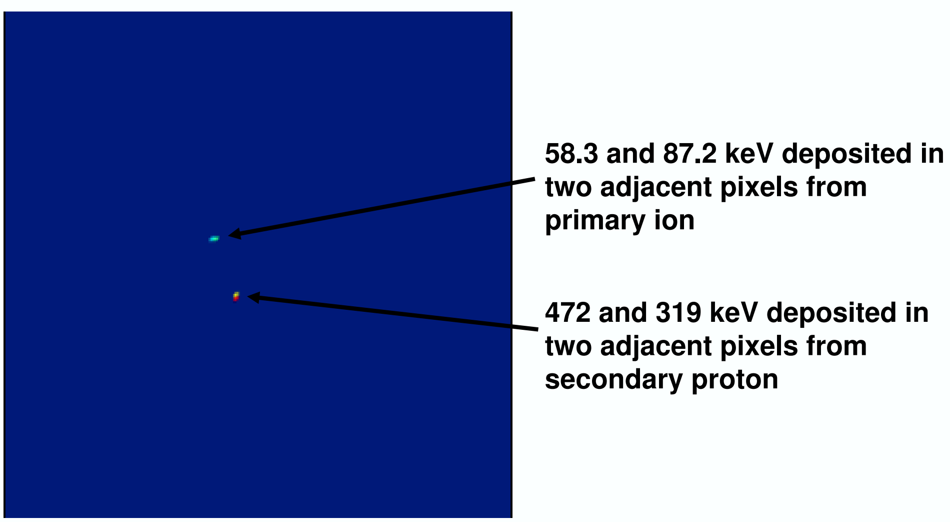

(b)

Figure 55: MRED event showing the incident proton depositing energy into two pixels of the array, and then creating scattering events in the aluminum mounting the FPA is placed on. A secondary proton recoils back towards the array and deposit additional energy into two pixels.

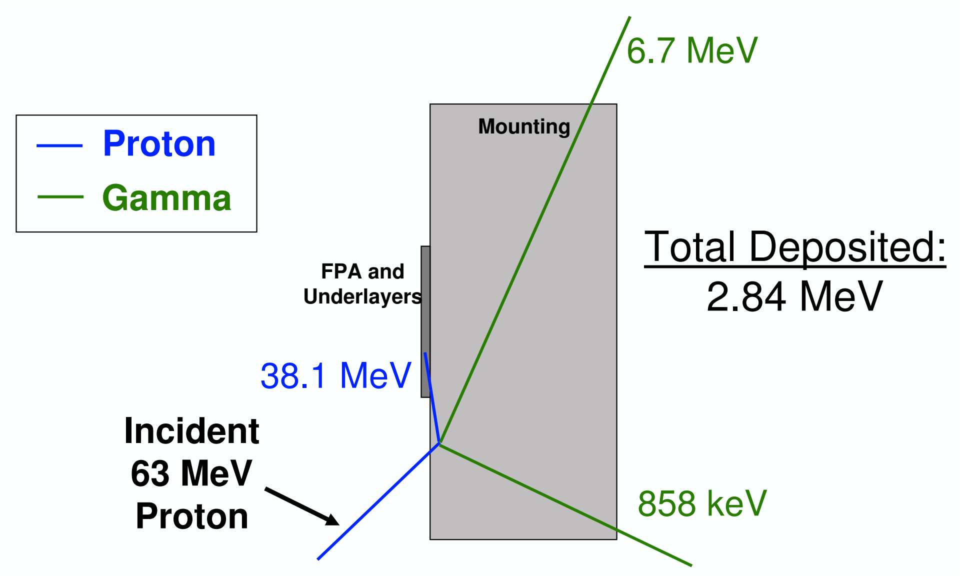

(a)

(b)

Figure 56: MRED event showing the incident proton missing the FPA, but creating scattering events in the aluminum mounting the FPA is placed on. Secondaries from this event recoil back towards the array and deposit energy into three adjacent pixels.

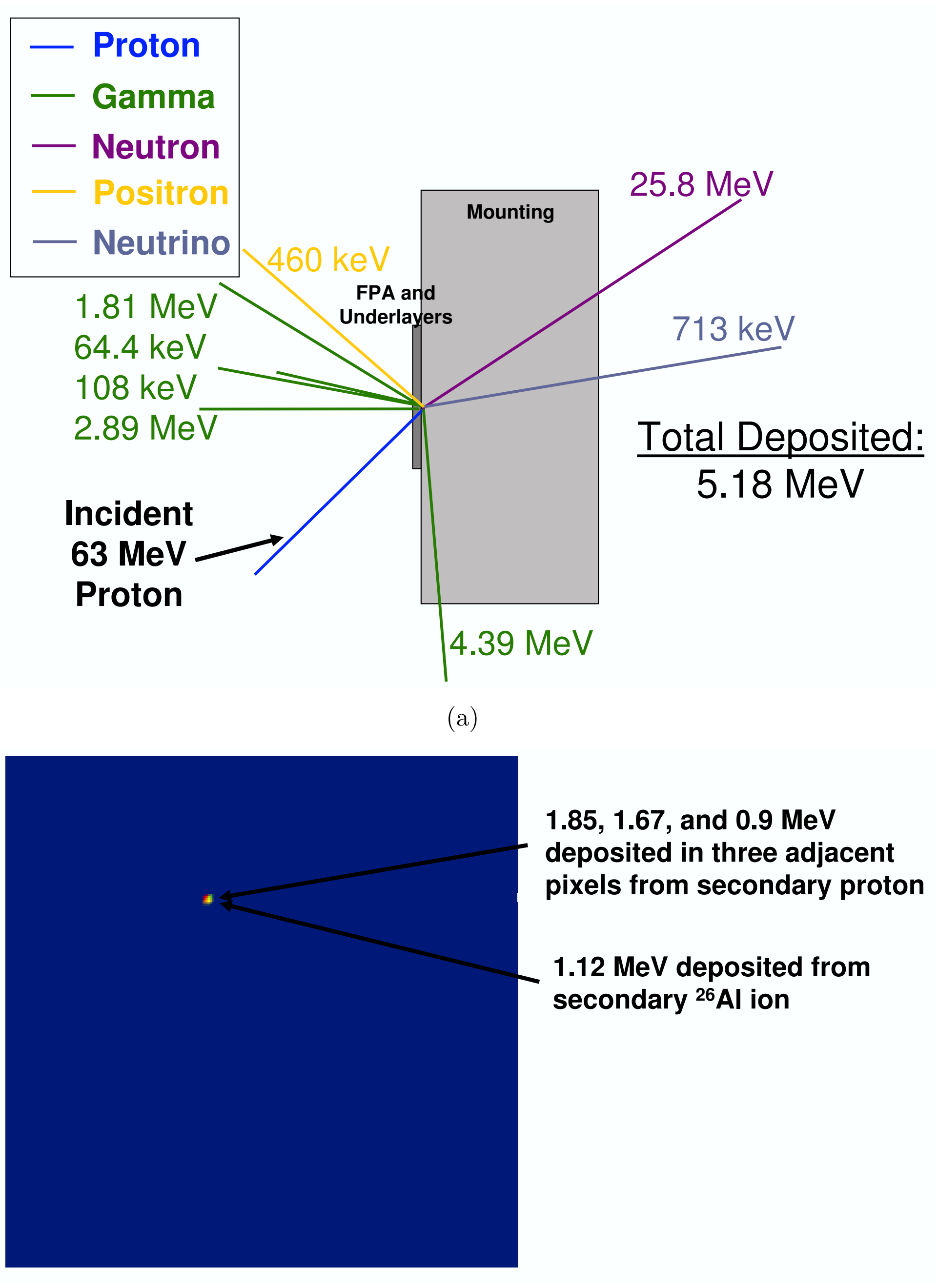

(a)

(b)

Figure 57: MRED event showing another example of how the incident proton deposits energy into the pixels, and subsequently creates secondaries in the mounting which also deposit energy into the pixel array. This event is interesting because of the large number of secondaries created and the heavy ^{26}Al ion.

Reaction Mechanisms

Figure 58 compares MRED simulations including all physics processes available in the simulation with simulations including direct ionization only. The two situations are shown for both the complex FPA structure on a mount from Figure 49 and the simple structure from Figure 46. In Figure 58, when comparing the two curves for the complex FPA structure on a mount (the triangle curves), nuclear reactions begin to dominate around 350 keV (where the two curves begin to deviate from one another). When comparing the two curves in this figure for the simple structure (represented by circles), this dominance is not seen until 420 keV. This slight difference is due to nuclear reactions scattering secondary particles back toward the pixels from the layers underneath as shown in the event images in the prior section. These scatters are not present in the simple structure because there are no underlying materials.

A larger difference is observed in the amount of energy deposited from direct ionization only in the complex structure when compared with the simple structure. In Figure 58, the simple, single pixel structure curve falls off at approximately 500 keV, while the complex FPA structure has energy depositions beyond 2 MeV. Again, the layers underneath the pixels are playing a role in the energy deposition through scattering events.

In Figure 59, MRED simulations for three situations: inclusion of all physics processes, direct ionization and screened Rutherford (Coulomb) scattering only, and direct ionization only are compared for the complex structure on a mount. Again, at energies below 350 keV, direct ionization dominates the device response, while screened scattering contributes little to the cross section for this structure. This is as expected for 63 MeV protons since the nuclear stopping power is 2500 times smaller

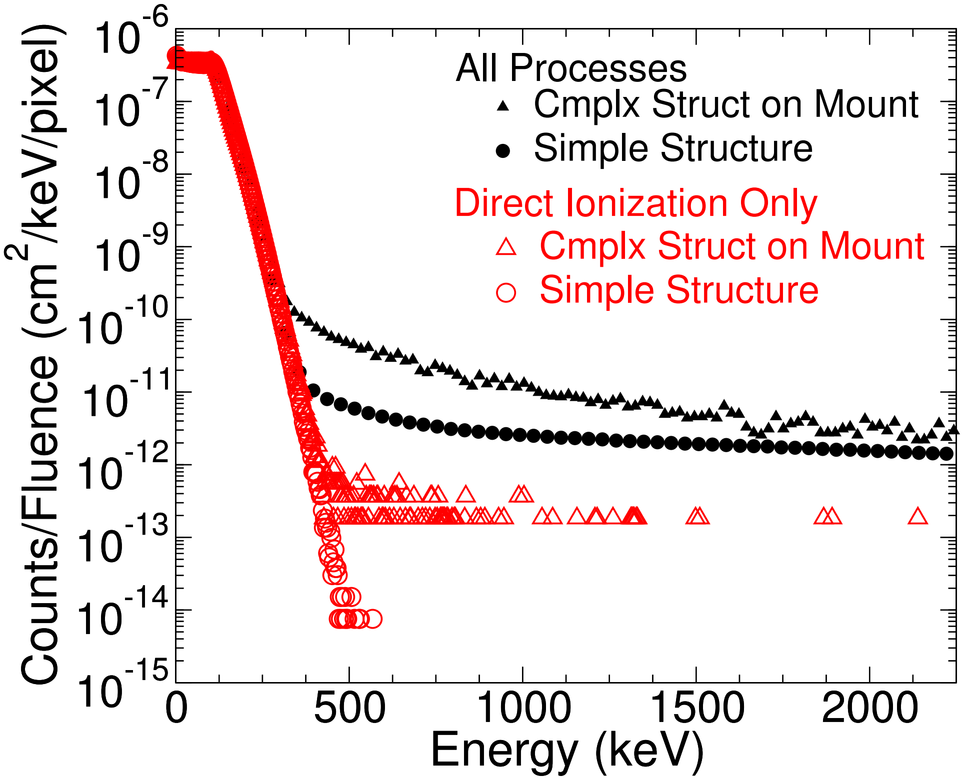

Figure 58: MRED simulations comparing reaction mechanisms. The small closed triangles represent the simulation of all physics processes available on the full FPA structure in Figure 49, and the large open triangles include direct ionization only on this same structure. The small closed circles represent the simulation of all physics processes on the single pixel structure from Figure 46, and the large open circles include direct ionization only on this same structure.

than the electronic stopping power at this energy, as shown in Chapter 2 Figure 16. Since the stopping power is so small, it is expected that direct ionization (the electronic portion of the stopping power) will be the dominant mechanism for energy deposition.

The dashed lines in Figure 60 represent the expected average and maximum energy deposited in the device from a constant-LET and path length distribution calculation. The dashed line labeled “Avg” is the energy deposited along an average path length through one pixel, and the dashed line labeled “Max” is the energy deposited along

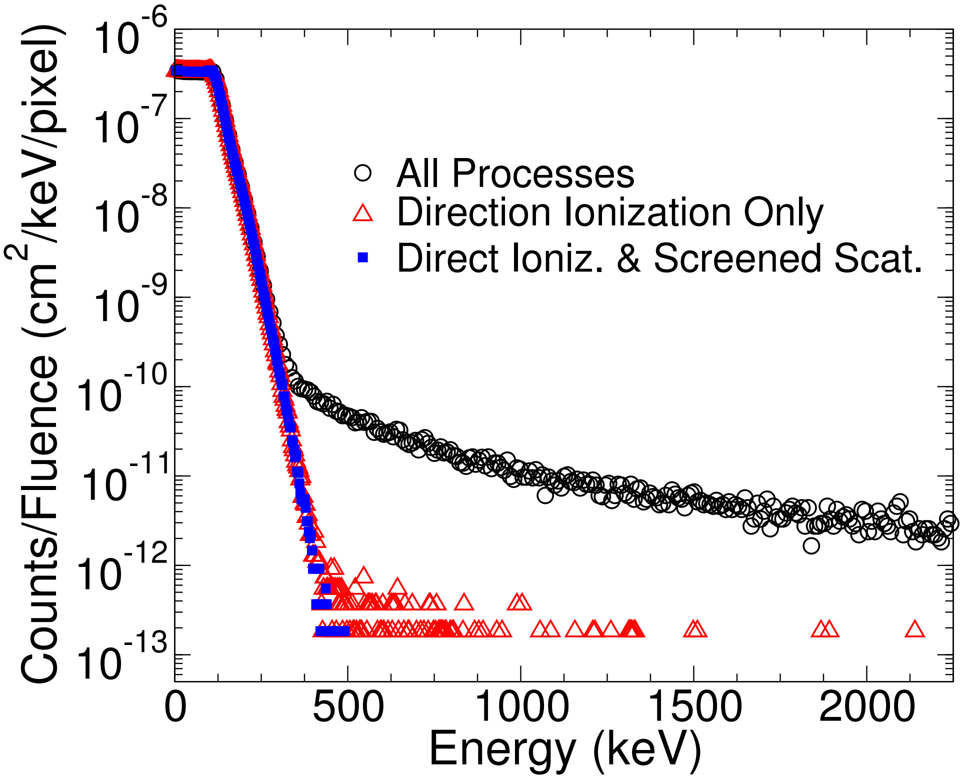

Figure 59: MRED simulations comparing reaction mechanisms. The large open circles represent the simulation of all physics processes available, the open triangles include direct ionization and screened Rutherford (Coulomb) scattering, and the small filled square include only direct ionization. Screened scattering contributes little as expected.

the longest path length through a single pixel. The maximum amount of energy deposited in the structure via this calculation is approximately 130 keV. Based on a constant LET analysis, no events are considered that deposit energy greater than this value. In 2004, Lomheim reported that for proton energy spectra encountered in space, the LET approximation would be appropriate [9]. However, the results for this device show that a constant LET model does not describe the shape of the curve in Figure 60 above 130 keV. The constant LET approximation considers only direct ionization, which is the dominant mechanism, but a path length analysis can only address averages while even primary ionization has fluctuations.

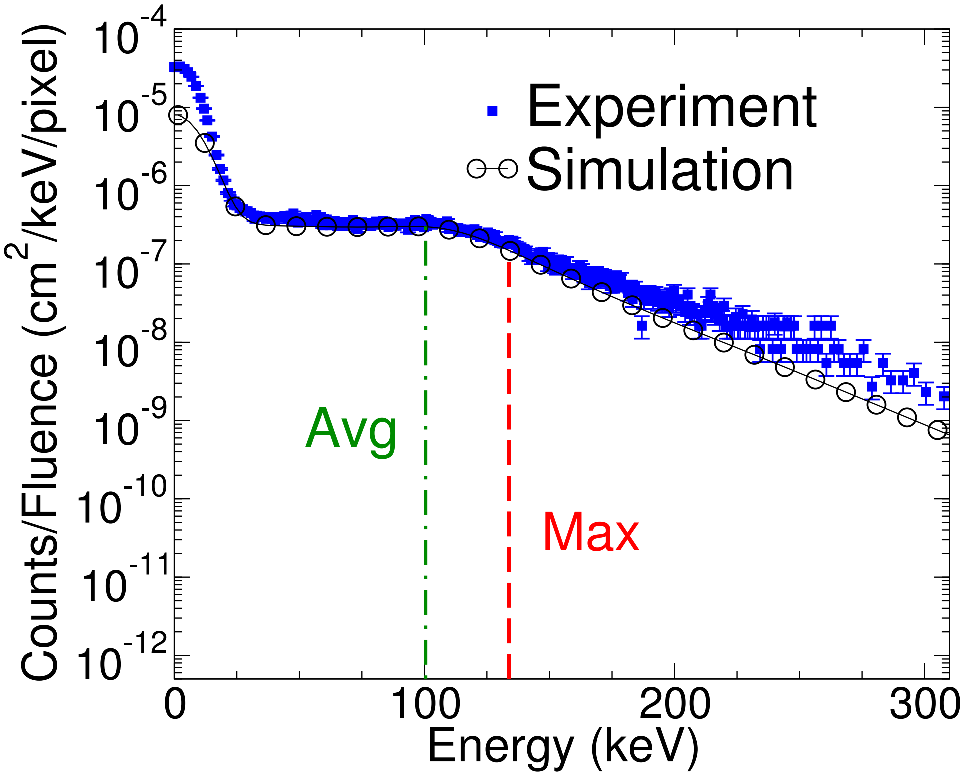

Figure 60: Differential spectrum comparing the simulation results with experimental data and a constant LET path length calculation. The path length calculation does not predict the occurrence of large energy depositions.

CHAPTER VI

EXTENDING SILICON FPA MODELING

This chapter extends the MRED simulations to evaluate the effects of angle on the imager response, determine the impact of the dewar window on the response of the device, and predict an event rate in space.

Effect of Angle

The importance of including the layers underneath the FPA is even more significant than noted above at oblique angles. Figure 61 shows MRED simulations at both 45 and 65° for the simple structure from Figure 46 as well as the complex structure on a mount from Figure 49. Simulations on the simple structure showed similar results at 45 and 65°, with a slight increase for the 65° curve between 200 and 500 keV. This increase is due to geometrical factors. At an angle of 45°, an incident ion will pass through either 1 or 2 pixels, while at 65°, an ion will always pass through 2 pixels and sometimes 3. This geometrical fact, shown in Figure 62, causes a slight increase in the counts per fluence per pixel curve until nuclear reactions take over. At this point, approximately 500 keV, the simple structure shows similar results at angles of 45 and 65°, while the complex structure shows a slight increase in the counts per fluence per pixel for the entire curve. This is due to the increased angle of backscatters coming from the layers below.

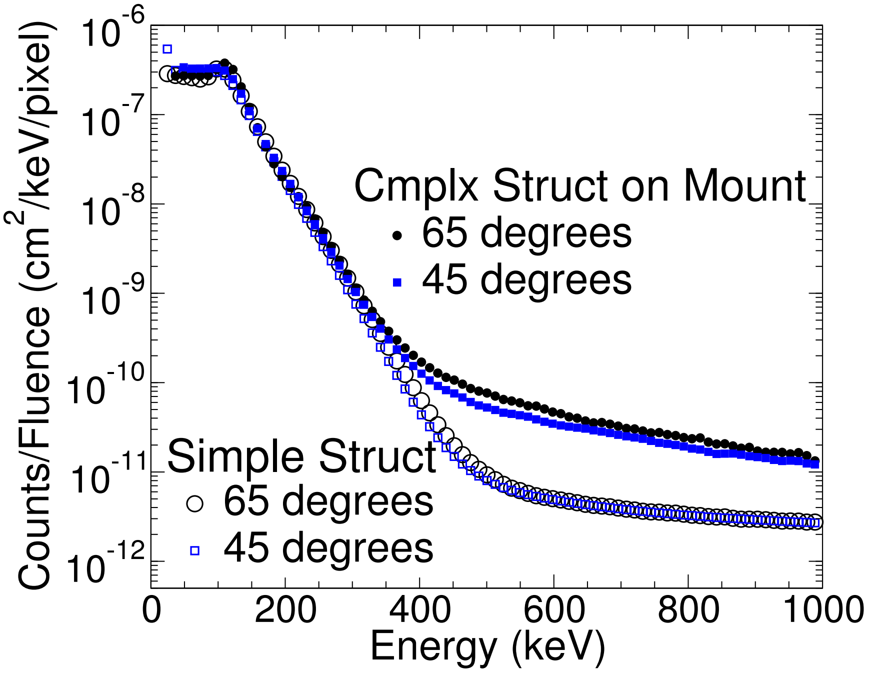

Figure 61: Differential spectrum of counts per unit fluence per pixel for 63 MeV protons incident on the focal plane array structure from Figures 46 and 49 at angles of 45 and 65°.

Simulations Including a Dewar Window

During the physical experiment, the protons pass through a thin aluminum dewar window before reaching the FPA. Figure 63 shows the MRED structure used in this section that includes a dewar window. The window was assumed to be 3.175 mm thick and placed 254 mm away from the FPA.

Figure 64 shows the results of including the dewar window. The presence of the aluminum dewar window caused a slight increase in the cross section. This increase is due to scattering events originating in the window. The variability in the curve in Figure 64 is due to low statistics. The structure in MRED is very large resulting in fewer particles striking the pixels.

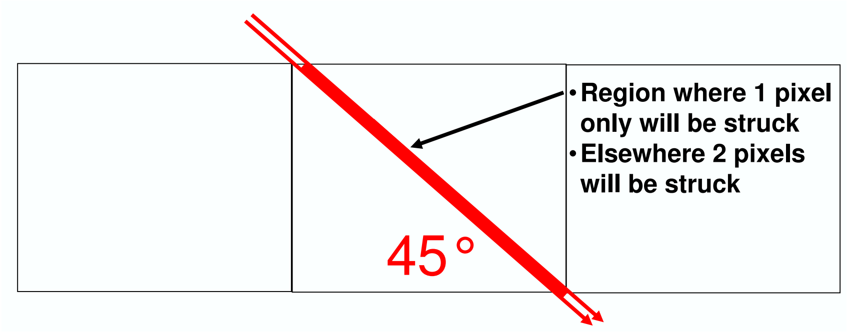

(a)

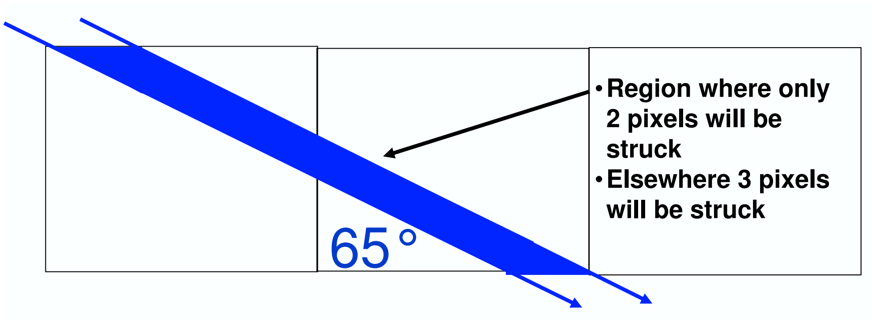

(b)

Figure 62: Pixels affected by a strike at (a) 45° and (b) 65°.

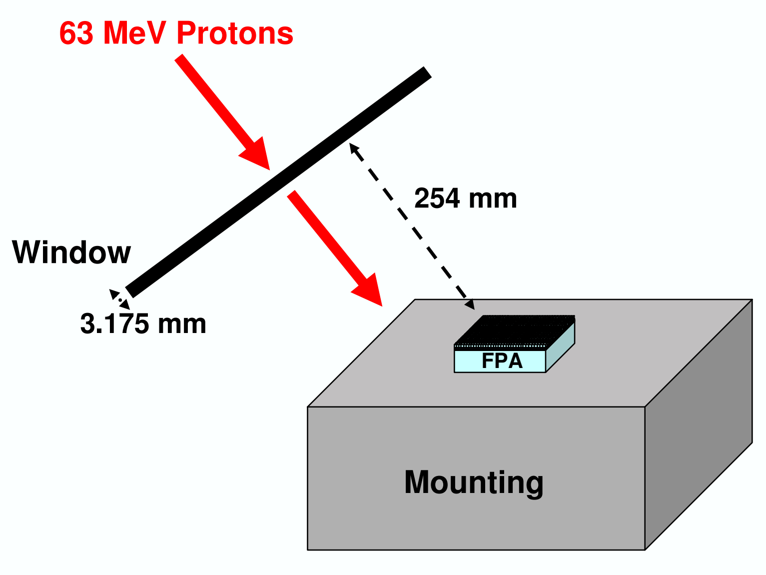

Figure 63: MRED structure including a thin aluminum dewar window. 63 MeV protons pass through the window before reaching the complex FPA structure.

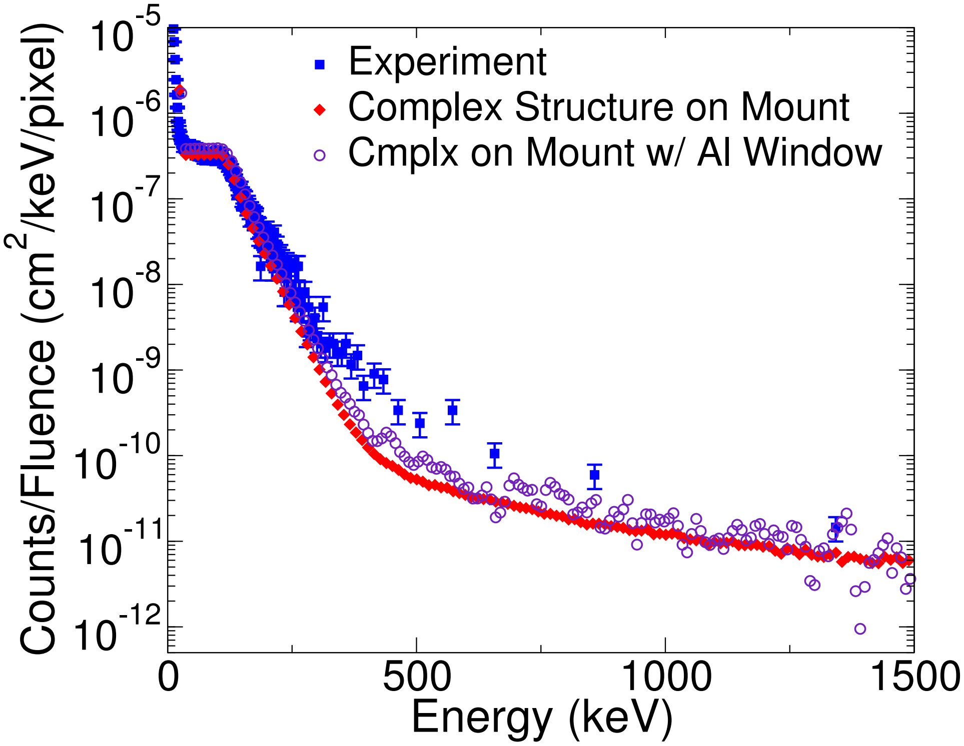

Figure 64: Differential spectrum of counts per unit fluence per pixel for 63 MeV protons incident on the focal plane array structure from Figure 63. The dewar window is 254 mm away from the FPA and 3.175 mm thick.

Event Rate Predictions From Space Proton Fluxes

In this section, event rate simulations are shown for proton environments computed using MRED. The results are compared to calculations done using CREME96. For this calculation, MRED simulations were done with an isotropic ion fluence. Figure 65 shows the environment models used in the calculations in this section. The curves were computed using CREME96 [27]. The curve labeled "GEO" is for the peak five minutes in geosynchronous orbit while the "ISS" curve represents the international space station orbit using ap8min [79] for solarmin.

Figure 66 shows the MRED simulated event rate in events per pixel per day as a function of deposited energy for the peak five minutes in the geosynchronous orbit

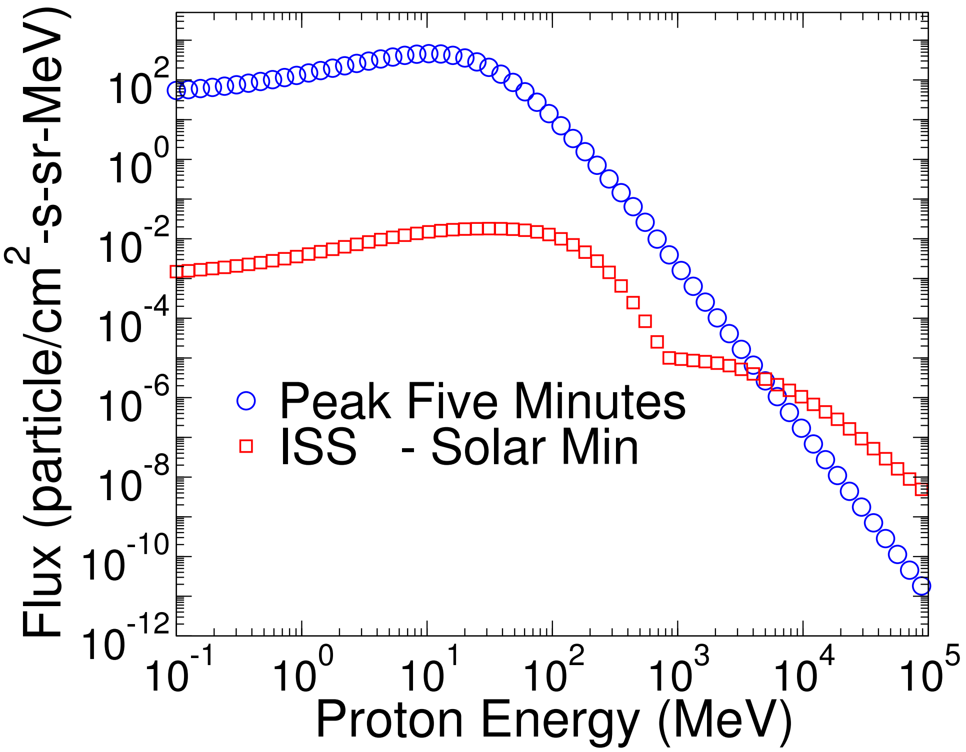

Figure 65: Proton environments calculated using CREME96 [27]. The "GEO" curve is for the peak five minutes in geosynchronous orbit and "ISS" is for space station orbit using ap8min for solarmin.

proton environment on both the simple structure and the complex structure on a mount. The event rate for the simple structure is slightly higher than the event rate for the complex structure on a mount. The reason for this is that essentially half of the ions are being shielded from the pixels by the underlying materials and mount as shown in Figure 67. For this type of calculation, the scattering events become less dominant because of the isotropic beam and the simple structure gives an appropriate estimation of the event rate. The MRED simulations in the remainder of this chapter are on the simple structure.

Figure 68 presents the integrated event rate in events per pixel per day as a function of deposited energy for the peak five minutes in the geosynchronous orbit

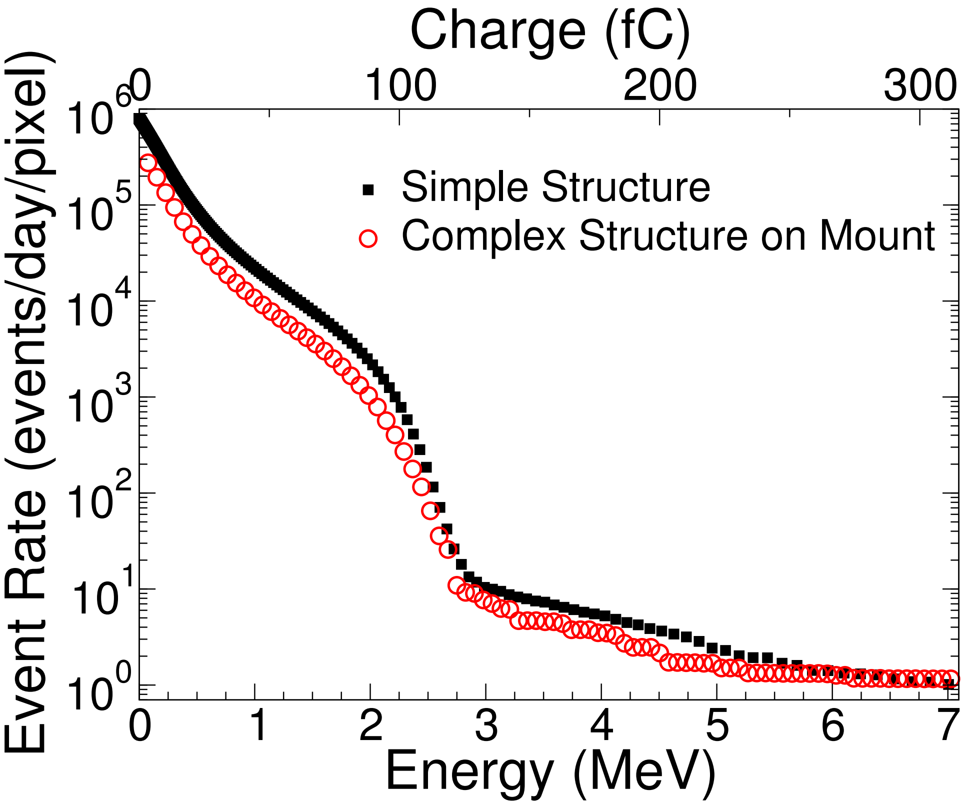

Figure 66: Proton environments calculated using MRED for the peak five minutes in geosynchronous orbit on the simple and complex structures.

proton environment. MRED simulations show that when the full proton spectrum is considered, direct ionization dominates at energies below 2.75 MeV (125 fC). Figure 68 also presents event rate calculations done with CREME96, which only consider direct ionization. At energies below 1.75 MeV (80 fC), there is good agreement between the MRED simulations and the CREME96 results. However, if the default value for the minimum energy in the LET spectrum of 0.1 MeV/u is used in the CREME96 calculation, the event rate is overestimated by as much as four orders of magnitude at higher energies. This overestimation is due to the limited range of protons in large silicon volumes, which is not considered by the CREME96 calculation. CREME96 uses only the initial value of the particle's LET and does not include slowing down

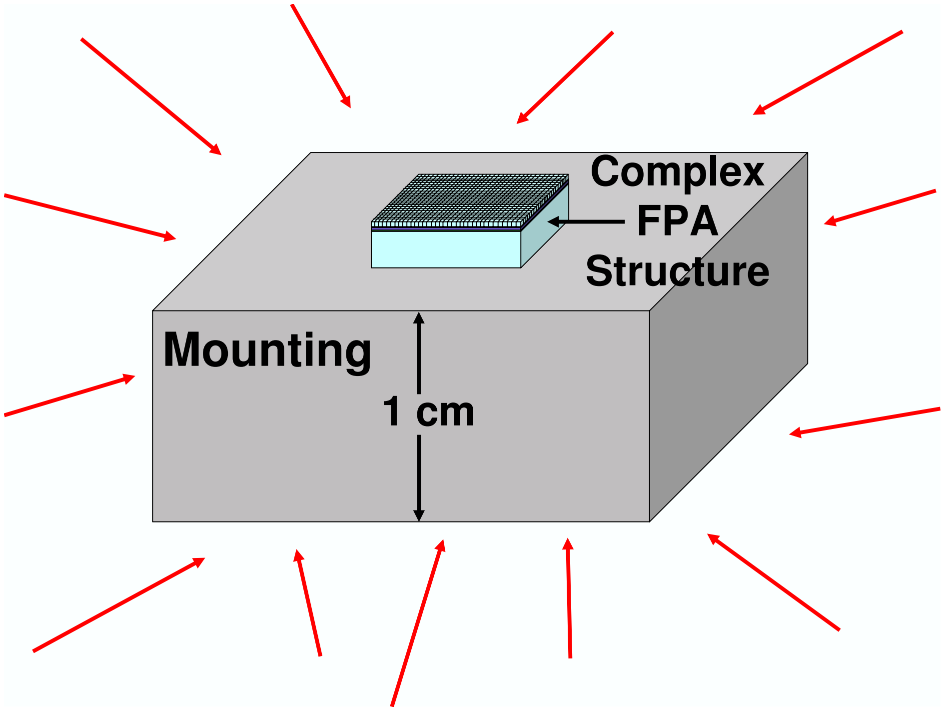

Figure 67: Isotropic beam on complex structure on a mount. Half of the ions are shielded by the thick mount.

along the particle's track. For smaller volumes this is okay, but for larger values such as the one considered here, the constant LET results in an overestimation. This is noted on CREME96's website, and its authors suggest adjusting the minimum energy parameter for certain SEU applications [27]. When a minimum energy value of 1.25 MeV/u is used in the CREME96 calculation, the event rate is comparable to the event rate obtained through MRED simulations. This value was obtained by fitting to the MRED simulations. Thus for ground testing energies, CREME96 is a good predictor of device response. However, at energies expected in space, a high fidelity simulation that includes tracking of the ion through the structure is needed to avoid overestimating the event rate by not properly adjusting the minimum energy parameter in CREME96.

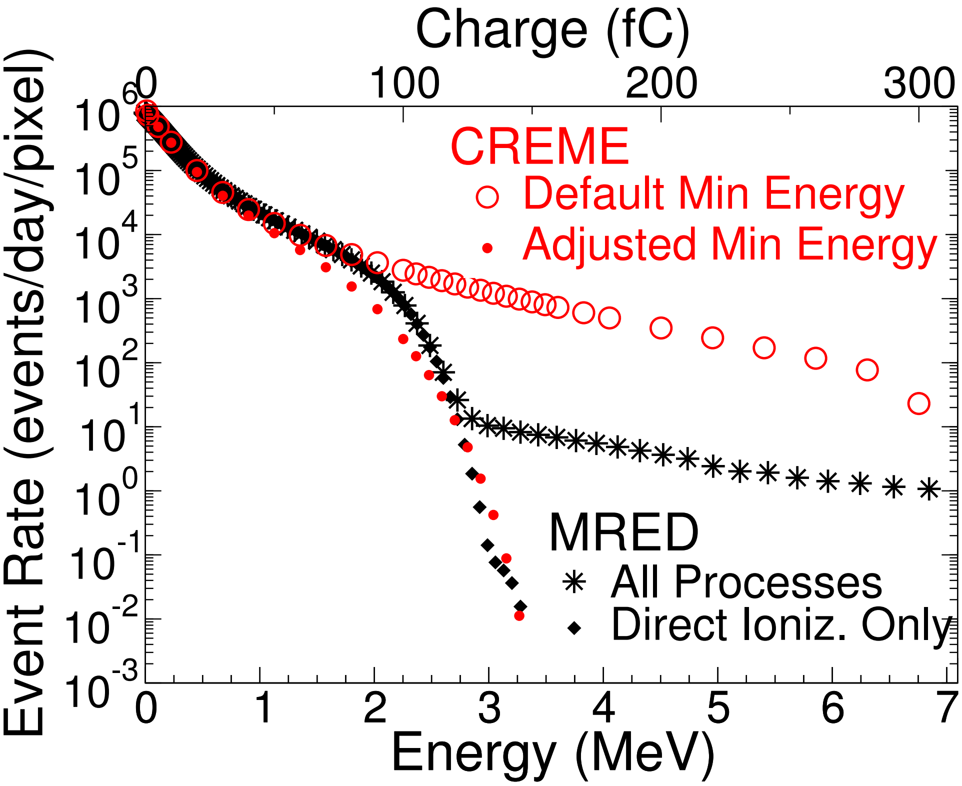

Figure 68: Simulation results of the expected event rate from geosynchronous peak five minute proton environment in Figure 65. Direct ionization dominates below 2.75 MeV (125 fC). To accurately predict the event rate at higher energies using CREME96, the minimum energy in the LET spectrum must be properly adjusted.

When the same calculation is done for the international space station orbit, again we find that below 2.5 MeV, the rate is dominated by direct ionization, as in Figure 69. Due to lower proton fluxes, the event rate is several orders of magnitude lower than the geosynchronous rate, as expected. The default CREME96 parameters again overestimate the event cross section by several orders of magnitude unless the minimum energy parameter is adjusted to 1.25 MeV/u.

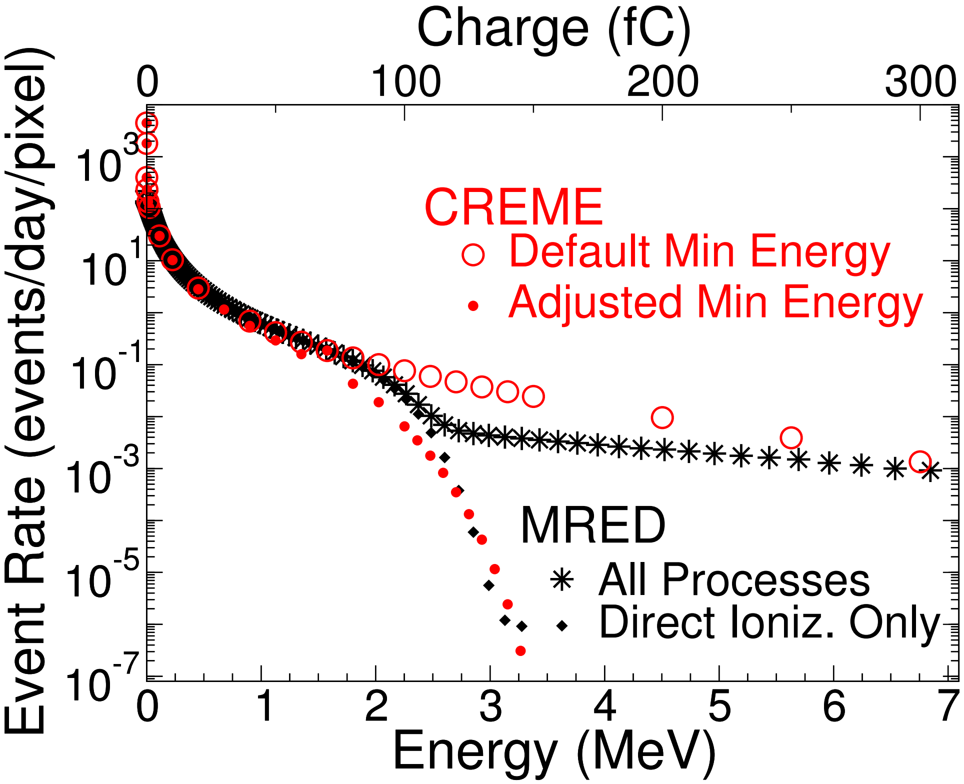

Figure 69: Simulation results of the expected event rate from ISS orbit solar min proton environment in Figure 65. As expected the event rate is several orders of magnitude lower than the expected geosynchronous rates, but once again, incorrect adjustment of the CREME96 parameters could result in an overprediction of event rate.

CHAPTER VII

CONCLUSION

Using Monte Carlo based simulations, the proton-induced energy deposition in a silicon PIN focal plane array was analyzed, and the importance of considering the materials surrounding a device was shown by comparing the results with experiment. This includes materials around all sides of the device, even those a centimeter away. During ground testing, caution must be used when setting up the experiment because dewar windows and mountings can also affect the amount of energy deposition observed in the device. Failure to include materials below a structure during simulation will result in an underprediction of the response for devices with high sensitivity to single events, such as detector arrays. This work shows that a high fidelity simulation is needed to estimate the energy deposited, or large energy events will be missed. This approach uses MRED by simulating all physics processes and tracking ions through the device. MRED simulations, in combination with pile up, can provide a good approximation of the expected radiation induced energy deposition. This high fidelity simulation approach can be used for other device modeling as well.

The MRED simulations on the silicon imaging device show that direct ionization is the dominant mechanism for energy deposition below 300 keV in the focal plane detector considered here, while nuclear reactions dominate at higher energies and screened Rutherford scattering contributes very little. Even though direct ionization is the dominant mechanism, a constant LET and path length calculation does not address the fluctuations in dE/dx, only the variation in path length, and therefore does not capture the shape of the differential distribution. Modeling codes that use only a single value LET will fail to predict the response accurately.

MRED simulations show that, when an omnidirectional beam is considered and an on-orbit event rate calculated, a simple structure including only one pixel and excluding surrounding materials to obtain error rate calculations is sufficient, with significantly improved accuracy over CREME96 calculations. The surrounding materials in this type of simulation essentially shield the sensitive regions of the device. The simple structure will result in a worst-case analysis of event rate.

Future Work

At higher energies, a slight difference is seen between the experimental data and MRED simulations. One issue that could be contributing to the difference between the two curves is an identified issue with the nuclear reaction models used by Geant4. There is an underprediction in the fragmentation energy resulting from nuclear reactions [80], [62]. Figure 70, taken from Reed *et al.*, shows how GEANT4 simulations differ from experimental results. This systematic error makes it difficult to simulate the sensitive region where nuclear reactions begin to dominate, which is precisely where the difference is seen in this work between simulation and experiment. Future versions of MRED are in progress that will have an additional feature in which this issue will be handled better. Preliminary simulations on other structures have indicated this new feature may help to explain the differences in the curve seen in this work between experiment and simulation. There is also some discussion within the community regarding a possible issue with the dE/dx in Geant4 [81]. This is currently being investigated further.

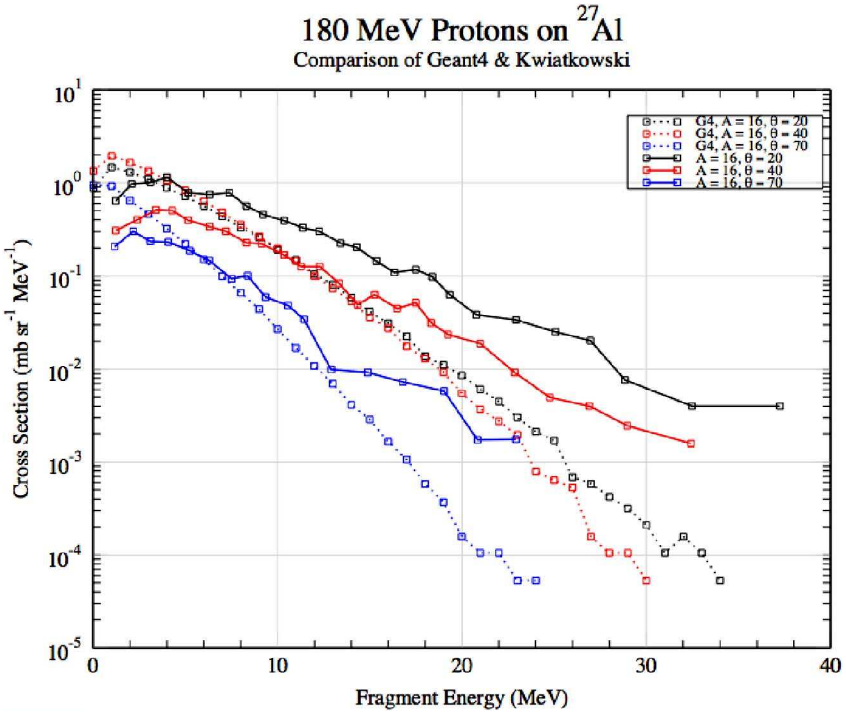

Figure 70: Comparison of Geant4 simulation with experimental results showing Geant4's underprediction of fragment energy, taken from [80].

There are currently test plans for a new silicon imager device. This device has a smaller pixel size than the one discussed here, but is similar in design. This will allow for a comparison between the two devices in response to radiation experimentally and through simulation. Once the experimental results are obtained, MRED simulations can be performed in the same manner as outlined in this thesis. This new device will give a great deal of insight into explaining the differences in the curves shown in this document. If the experimental data from the new device and the MRED simulations have the same slight difference at higher energies as shown here, then the issue can be narrowed down to MRED. If the difference is much smaller, or gone completely, then the issue can be narrowed down to a problem with the testing done on the device in this document, or lack of including a key surrounding material in the simulation that was present at the time of experiment. It would also be beneficial to assess the energy deposition from a lower, more ionizing proton energy such as 12 or 22 MeV, if experiment allows.

Another way to further quantify the effects of energy deposition using MRED is to use the idea of weighted sensitive volumes [82]. MRED allows for each sensitive volume to be assigned a weight. Using this method, the charge collected in a sensitive volume can be determined through simulation and the following equation

$$Q_{collected} = \frac{1pC}{22.5MeV} \sum_{i=1}^{N} \alpha_i E_i \tag{12}$$

where α_i is the weighting coefficient of the sensitive volume and E_i is the charge deposited in that volume [82]. Determining the appropriate weight to give each portion of the sensitive volume can be tricky. It will require more in-depth TCAD simulations to be completed first in order to determine more precisely how the charge generated in a pixel is collected. By doing this analysis and new MRED simulations, the small amount of charge motion noted in the TCAD simulations in chapter 4 can be accounted for. This may help resolve the difference seen between experimental results and MRED simulations. The amount of charge motion is very small though and more likely contributing to the lower portion of the curve where agreement is good, but for a complete look at all possibilities, it should be further considered.

Once the details of the high energy region have been worked out, future work can also include taking the methods of simulation described in this document and calculating the expected response for a pixel structure that is twice the height as the one described here. The implications of the height change have not been quantified in the literature thus far. Knowing these effects will help device designers understand how the physical size changes in these types of detectors will effect the radiation response.

Future work may also include using the methods described here to simulate HgCdTe FPAs using both MRED and TCAD. Simulation of these devices is extremely difficult due to low precision in many simulators so very little work has been published on the topic. With the methods outlined here, however, it should be straightforward to predict the proton-induced radiation response of a HgCdTe FPA.

Appendix A

EXAMPLE MRED INPUT FILE

Example run file for MRED used in this document. The structure is the complex structure on mount, shown in chapter 5. This script simulates 63 MeV protons on this structure at an angle of 45°, and computes the energy deposited in each of the sensitive volumes (pixels). A linearly binned histrogram of the energy deposited is output to an hdf5 file.

This example includes only those commands of interest to the work in this document, and should be used as a reference only. Note that many other commands are available in MRED and input files for future versions of the application, including the online version, will appear differently. Comments are denoted by a # at the beginning of the line. Some comments come directly from the example initialization file provided by MRED's creators.

```
#!/usr/bin/env python

import sys
import cPickle
import base64

# Startup MRED file
execfile('run_mred.py')

###############
## MRED8 run ##
###############

# Setup the physics for the run

# 11/Jan/2007
#
# Select one EM process from the following list. "Standard" is Geant4 standard
# EM physics. "StandardScreened" is the same except that the VU screened
```

```
# Coulomb scattering is added for ions. "LowEnergy" is a simple Geant4
# low energy EM physics implementation without screened scattering.
# "EmLowEnergyQED" and "EmPenelopeQED" include screened scattering for ions
# and were intended to be the most comprehensive, using Geant4 low energy
# and Penelope physics respectively. As of this writing, StandardScreened
# appears to have a more compelling treatment of ion stopping and is faster.
# Therefore, it is selected as the default for most semiconductor device
# applications pending improvements in the Geant4 low energy and Pendelope
# code.
#
mred8.physics.addModule('StandardScreened')

# ------------------------------------------------------------------------------
# These are for elementary particles. Normally use them all.
mred8.physics.addModule('HadronElastic')
mred8.physics.addModule('HadronInelastic')
mred8.physics.addModule('PiKInelastic')

# ------------------------------------------------------------------------------
# Neutron & proton physics. Select one of four.
# "NucleonInelasticA" = binary cascade + HP neutrons
# "NucleonInelasticB" = Bertini cascade + HP neutrons
# "NucleonInelasticC" = Bertini cascade + standard neutrons
# "NucleonInelasticD" = binary cascade + standard neutrons (default)
#
mred8.physics.addModule('NucleonInelasticC')

# ------------------------------------------------------------------------------
# 'AltIonInelastic' is the default ion-ion model
#
mred8.physics.addModule('IonInelastic')

# ------------------------------------------------------------------------------
mred8.physics.list.SetBiasPrimaryOnly(True)
mred8.physics.list.SetSigmaBiasFactor(1.)
mred8.physics.list.SetUseTrackWeighting(True)
print mred8.physics.list.GetSigmaBiasInfo()

# ------------------------------------------------------------------------------
mred8.physics.range_cuts = 50.*micrometer

# We know the material list ahead of time, so we need to enable SiO2,  since
# only silicon and vacuum are enabled by default.
mred8.material.enableBasicElectronicMaterials()
#mred8.material.enableMaterial('SiO2')
mred8.material.enableMaterial('indium')
mred8.material.enableMaterial('nickel')
mred8.material.enableMaterial('tantalum')

# Create an instance of a RPP device
mred8.setDevice('rpp')

# Variables
numPixels=128
```

```
devW=numPixels*60
baseW=devW*3
baseZ=1.
substrate=300.
arCoating=0.35
subPixel=10.175
roicSize=5.54

mred8.device.setLayers([
((devW*um, devW*um, 0.35*um), 'aluminum'),
((devW*um, devW*um, 50.*um), 'silicon', 'sd'),
((devW*um, devW*um, 0.025*um), 'titanium'),
((devW*um, devW*um, 0.15*um), 'nickel'),
((devW*um, devW*um, 10.*um), 'indium'),
((devW*um, devW*um, 0.4*um), 'Si3N4'),
((devW*um, devW*um, 1.0*um), 'SiO2'),
((devW*um, devW*um, 0.1*um), 'TiN'),
((devW*um, devW*um, 0.84*um), 'aluminum'),
((devW*um, devW*um, 0.1*um), 'titanium'),
((devW*um, devW*um, 0.6*um), 'SiO2'),
((devW*um, devW*um, 0.1*um), 'TiN'),
((devW*um, devW*um, 0.45*um), 'aluminum'),
((devW*um, devW*um, 0.1*um), 'titanium'),
((devW*um, devW*um, 0.6*um), 'tungsten'),
((devW*um, devW*um, 0.1*um), 'TiN'),
((devW*um, devW*um, 0.45*um), 'aluminum'),
((devW*um, devW*um, 0.1*um), 'titanium'),
((devW*um, devW*um, 0.6*um), 'SiO2'),
((devW*um, devW*um, substrate*um), 'silicon')]),
((baseW*um, baseW*um, baseZ*cm), 'aluminum')])

# Create array corresponding to centers of sensitive volumes
xCenters=range(-devW/2,devW/2,60)
yCenters=range(-devW/2,devW/2,60)

SVx=30
SVy=30

# Bottom and top of sensitive volumes
zbttm=-(((substrate+arCoating+subPixel+roicSize+50.)/2.0)-arCoating)
ztop=-(((substrate+arCoating+subPixel+roicSize+50.)/2.0)-arCoating-50.0)

# Offset from centers
xoffset1=0
yoffset1=0

# Initialize the simulator
mred8.init()

# Visualize
mred8.suv()

# ---------------------------------------------------
# Define multiple sensitive volumes
```

```
svCounter=0
sd=mred8.sd_vector[0]
minValidEnergy=100*eV

for x in xCenters:
 for y in yCenters:
    sd.addSensitiveVolume()
    sd.sv_vector[svCounter].rpp_min_corner=(
               vector3d(x+xoffset1-SVx,y +yoffset1-SVy,zbttm)*micrometer)
    sd.sv_vector[svCounter].rpp_max_corner=(
                vector3d(x+xoffset1+SVx,y +yoffset1+SVy,ztop)*micrometer)
    sd.sv_vector[svCounter].on=True
    sd.sv_vector[svCounter].min_valid_energy=minValidEnergy
    svCounter+=1

sd.coincidence_order=1

# -------------------------------------------------
# Set up histograms so all SVs point to same histogram

numSVs=sd._mredPySensitiveDetector__sd.GetNumberOfSensitiveVolumes()

h=mred8.runAct.GetNewHistogram('hist', 1525.832*eV, 50.*MeV, 16384, False)

for i in range(0, numSVs):
sd._mredPySensitiveDetector__sd.SetSVHistogram(i,h)

mred8.runAct.SetAutoGenerateHistogramFlag(False)

# -------------------------------------------------
mred8.accumulate_histograms=True

# Setup the gun
mred8.gun.setDefaults()
mred8.gun.setParticle('proton')
mred8.gun.direction=vector3d(0,1,1)
mred8.gun.energy=63*MeV
mred8.gun.random_flux=True

mred8.physics.screened_scattering.mean_free_path_scale_factor=5

mred8.hdf5.file_path='/home/'
mred8.hdf5.file_name='test.run.hdf5'
mred8.hdf5.write_output_files=False
mred8.hdf5.include_energies=False
mred8.hdf5.include_tracks=False
mred8.hdf5.include_hits=False
mred8.hdf5.include_histograms=True
mred8.progress_interval=50000

# Run particles
mred8.beamOn(200000)
```

```
# Kill mred8
mred8.exit()
```

Appendix B

REDUCING DATA

Experimental Data Script

The python script below was used to reduce the experimental data. It filters out the 'NAN' pixels (those whose voltage was not recorded because they are known to be noisy and upredictable), and then bins the data points such that there are exactly 10 non-zero points in each bin.

```
import numpy
import sys
import os
import math

# This file was written by Marcus Mendenhall on 12 July 2007
# Modified by Christina Howe on 3 Sept 2007
# File takes experimental imager data, already subtracted from its clear frames
#    and plots using bins that contain exactly 10 non-zero data points each,
#    "smart binning".

if len(sys.argv) < 9 :
print >> sys.stderr, "Usage: python", os.path.basename(sys.argv[0]), "ExpDataFile
                      ExpFlux(p/s-cm^-2) IntegTime(s/frame) NumFrames ElecConv(v/e)
      AdPrec(v) ElecHolePair(eV) outfilename"
print >> sys.stderr, "This file histograms data in dataFile according to the bins in
                      binFile and saves in outfilename."
sys.exit(0)

expDataFileName=sys.argv[1]
flux=float(sys.argv[2])
intTime=float(sys.argv[3])
frames=float(sys.argv[4])
elec_conv=float(sys.argv[5])
ad_prec=float(sys.argv[6])
ehpair=float(sys.argv[7])*1e-6
outFileName=sys.argv[8]

datafile=open(expDataFileName,"r")

data=map(float, [x for x in datafile if x.strip() and x.strip() != "NAN"])

datafile.close()
```

```
data.sort()

binwalls=[data[0]]
binxy=[0]
binvals=[0]

fluence=flux*intTime*frames
minbinwidth=ad_prec
fluence_scale=fluence*len(data)/frames

# Print message to screen to assure values are correct

print >> sys.stderr, "The experimental fluence = " , fluence , " cm^-2"
print >> sys.stderr, "The number of frames = " , frames
print >> sys.stderr, "The electron conversion factor =
                      ", elec_conv , " volts/electron"
print >> sys.stderr, "The A/D precision = " , ad_prec , " volts"
print >> sys.stderr, "The energy required to create eh pair = ", ehpair/1e-6 , " eV"
print >> sys.stderr, "The fluence scale = " , fluence_scale

for v in data:
    if not (v-binwalls[-1] < minbinwidth or binvals[-1] < 10):
        binwalls.append(v)
        binvals.append(0)
        binxy.append(0)

    binvals[-1] += 1
    binxy[-1]+= v

if binwalls[-1] != data[-1]:
    binwalls.append(data[-1])

sigmas=[0.0]*len(binvals)

outfile=open(outFileName,"w")
for i in range(len(binwalls)-1):
    sig=math.sqrt(float(binvals[i]))
    binmean=(binxy[i]/binvals[i])*(ehpair/elec_conv)
    binwidth=(binwalls[i+1]-binwalls[i])*(ehpair/elec_conv)
    print >> outfile, binmean, \
          binvals[i]/binwidth/fluence_scale, sig/binwidth/fluence_scale

outfile.close()
```

Processing MRED HDF5 File

The python script below takes the hdf5 files from multiple runs created by MRED, sums them into one array, and produces four data sets: (1) the raw MRED data of counts as a function of energy, (2) MRED differential spectrum of counts per fluence per pixel as a function of energy, (3) MRED integral spectrum of counts/fluence/pixel as a function of energy, and (4) differential spectrum of post-processed MRED simulations to account for pile-up and the non-radiation induced noise.

```
#!/usr/bin/env python

# Author: Brian Sierawski
# Modified: Christina Howe and Robert Weller
# Read in specified .hdf5 files, accumulate the histograms
# and print out in a n-column text format.  Don’t give
# this script .hdf5 files with different histograms or
# different numbers of histograms. Also perform pileup
# routine on MRED simulations

# This script will print out each histogram in the given
# hdf5 files.  The first column of each row is the bin
# energy (should be in MeV, but it doesn’t hurt to check
# this), the second is the count in the given bin for
# the first histogram, the third column is the standard
# error of the bin for the first histogram, the fourth
# column is the count in the given bin for the second
# histogram, and so on...

from mred_hdf5 import *
import pileup
import numpy
import math
import sys
import os
import gzip
import vumps

if len(sys.argv) < 9 :
print >> sys.stderr, "Usage: python", os.path.basename(sys.argv[0]),
                     "outfilename indexValue Nt fluence_unit(cm^-2)
      binWidth(MeV) numPixels mu sigma MREDfile1 MREDfile2 etc..."
print >> sys.stderr, "This file accumulates runs and outputs the SV histogram in
                      2 column format, post-processed MRED data, and integral data."
print >> sys.stderr, "February 23, 2007"
sys.exit(0)

outfilename = sys.argv[1]
indexValue = int(sys.argv[2])

Nt = sys.argv[3]
fluence_unit = sys.argv[4]
binWidth = sys.argv[5]
numPixels = sys.argv[6]
```

```
mu = float(sys.argv[7])
sigma = float(sys.argv[8])

#------------------------------------------
# 2 Column output

hlist=accumulate(sys.argv[9:])

# Check that each histogram has the same x values
energiesMatch=True
energies=hlist[0].x
for h in hlist:
    if(not (h.x == energies).all()):
        energiesMatch=False
if (energiesMatch==False):
    raise RuntimeError, "Error: Energy bins do not match."

# Print out the histograms in a E, count

f2col=open(outfilename+'_2Col.dat','w')

for bin in range(len(hlist[0].x)):
    print >> f2col, hlist[indexValue].x[bin], hlist[indexValue].y[bin]

f2col.close()

#------------------------------------------
# Plot differential and integral spectrums

data=open(outfilename+'_2Col.dat').read()
data=data.split()
data=[float(i) for i in data]
fluence=float(fluence_unit)*float(Nt)
binWidth=float(binWidth)
numPixels=float(numPixels)

newData=[0.0*m for m in range(len(data))]
crossSecData=[0.0*m for m in range(len(data))]

fplot=open(outfilename+'_plot.dat', 'w')

# Divide y by (fluence*binWidth)
# Print out differential spectrum
for i in range(0,len(data),2):
newData[i]=data[i]
newData[i+1]=data[i+1]/(fluence*binWidth*numPixels)
print >> fplot, newData[i], newData[i+1]

fplot.close()

fint=open(outfilename+'_plot_integral.dat', 'w')

# Integrate y/fluence
```

```
for i in range(len(data)-1, 0, -2):
crossSecData[i-1] = data[i-1]
if i==len(data)-1:
crossSecData[i]=data[i]
else:
crossSecData[i]=(data[i]/(fluence*numPixels))+crossSecData[i+2]

# Print integral spectrum
for i in range(0,len(data),2):
print >> fint, crossSecData[i], crossSecData[i+1]

fint.close()

#--------------------------------------------
# Do pileup and print data file
# This portion written by Robert A. Weller

fin=open(outfilename+'_plot.dat')
sim=[map(float,x.strip().split()) for x in fin]
fin.close()
simx=[x[0] for x in sim[:16384]]
simy=[x[1] for x in sim[:16384]]

simypad2=pileup.pad_right(simy)
simypad2[0]=0.
simypu=pileup.pileup(simypad2,mu=mu)
simypu[0]=simy[0]
g=pileup.gaussian(sigma=sigma,x0=0.,nchan=len(simypu))
simypc=pileup.convolve(g,simypu)
fout=open(outfilename+'_PILEUP.dat','w')
for x in zip(simx,simypc[:len(simx)]):
    print >>fout, x[0], x[1]
fout.close()
```

Pile-up Routine

The following python script was written by Dr. Robert Weller, Vanderbilt University, and used on MRED simulations to account for pileup and include the non-radiation induced noise. Further description of pileup and the non-radiation induced noise is available in chapter 4.

```
import numpy
import math

def pileup(spect, mu, padding_replicas=16):
```

```
    """Starting with an un-normalized single-hit spectrum spect, compute
    what it would look like if a mean number of hits mu is used. The input
    spect should have a power-of-2 length for best efficiency, although
    numpy isn't too bad in other cases. padding_replicas should be
    a power of 2 somewhat bigger than mu. The argument padding_replicas,
    which defaults to 16, specifies the factor by which the working
    array should exceed the input array in size. The return value is a
    numpy array of the same length as the input spect."""
    if mu == 0.:
        return spect
    padded=pad_right(spect, padding_replicas)
    fft=numpy.fft.rfft(padded)
    #normalize spect and use expm1 for high-precision exp-1
    pileft=numpy.expm1((mu/fft[0])*fft)
    #scale out expm1 and reset norm to original
    piled=(fft[0]/numpy.expm1(mu))*numpy.fft.irfft(pileft)
    #undo numpy-ized numbers back to native python floats
    return numpy.array(map(float,piled[:len(spect)]))

def convolve(spect1, spect2, padding_replicas=2):
    """This produces the convolution of two spectra, which are assumed to
    be the same length. By default the spectra are padded in the middle
    to double the total number of channels. A value of zero for pading_replicas
    suppresses this padding. The return value is a numpy array of the same
    length and with the same ordering as the input spectra."""
    if len(spect1) != len(spect2):
        raise RuntimeError, "Spectra must be the same length."
    if padding_replicas == 0:
        ps1=spect1
        ps2=spect2
    else:
        ps1=pad_zeros(spect1,padding_replicas)
        ps2=pad_zeros(spect2,padding_replicas)
    fspect1=numpy.fft.rfft(ps1)
    fspect2=numpy.fft.rfft(ps2)
    cs=numpy.fft.irfft(fspect1*fspect2)
    n=len(spect1)/2
    r1=map(float,cs[:n+1])
    r2=map(float,cs[-n+1:])
    return numpy.array(r1+r2)

def pad_zeros(a, padding_replicas=2):
    """Return an array in standard form with zeros padded in the middle. This
    assumes that the array a has the zero value at offset zero, positive
    values at a[1:n/2+1] and negative values at a[n/2+1:], where n=len(a).
    The return value is a numpy array of floats."""
    n=len(a)/2+1
    r1=list(a[:n])
    r3=list(a[n:])
    r2=((padding_replicas-1)*len(a))*[0.]
    return numpy.array(r1+r2+r3)

def pad_right(a,padding_replicas=2):
    """Return an array with zeros padded on the right. This is a sensible
```

```
    operation for functions that are zero for negative arguments but which
    may have non-zero values in the upper half of the array. The argument
    padding_replicas, which defaults to 2, and should be a power of 2,
    expresses the relative size of the final array. By default the length
    of the input array a is doubled. For padding_replicas==4 the output
    array is quadrupled in size, etc. The return value is a numpy array of
    floats."""
    return numpy.array(list(a)+((padding_replicas-1)*len(a))*[0.])

def gaussian(sigma=1.,x0=0.,nchan=1024):
    """The function gaussian produces a gaussian shape centered about channel
    x0 with width sigma. These are assumed to be in units of channel width.
    The default spectrum is nchan=1024 channels and is wrapped so that channel
    0 contains the peak, with channel 1023 corresponding to the largest
    negative argument. nchan should always be a power of 2. The return value
    is a numpy array of floats."""
    ns=nchan/2-1
    x=numpy.array(range(nchan))-float(ns)
    z=numpy.append(x[ns:],x[:ns])-x0
    return numpy.exp(-z*z/(2.*sigma*sigma))/(sigma*math.sqrt(2*math.pi))
```

REFERENCES

[1] D. A. Scribner, M. R. Kruer, and J. M. Killiany, “Infrared focal plane array technology,” *Proc. IEEE*, vol. 79, pp. 66–85, 1991.

[2] P. A. Sabelhaus and J. Decker, “James Webb space telescope (JWST) project overview,” in *Aerospace Conference*, Big Sky, MT, Mar. 2006, pp. 1–13.

[3] G. R. Hopkinson, C. J. Dale, and P. W. Marshall, “Proton effects in charge-coupled devices,” *IEEE Trans. Nucl. Sci.*, vol. 43, pp. 614–627, 1996.

[4] A. Claret, H. Dzitko, and J. J. Engelmann, “Transient particle effects on the ISOCAM instrument on-board the infrared space observatory,” *IEEE Trans. Nucl. Sci.*, vol. 49, pp. 1511–1518, 1999.

[5] J. Pickel, “Novel devices and sensors,” 1993 IEEE Nuclear and Space Radiation Effects Conference Short Course, Snowbird, UT, July 1993.

[6] R. S. Muller and T. I. Kamins, *Device Electronics for Integrated Ciructs.* Hoboken, NJ: John Wiley and Sons Inc, 2003.

[7] F. J. Morin and J. P. Maita, “Electrical properties of silicon containing arsenic and boron,” *Phys. Rev.*, vol. 96, pp. 28–35, 1954.

[8] P. Capper and C. T. Elliot, *Infrared Detectors and Emitters: Materials and Devices.* Boston, NJ: Kluwer Academic Publishers, 2001.

[9] T. S. Lomheim, “Optical detectors and imaging arrays,” 2004 IEEE Nuclear and Space Radiation Effects Conference Short Course, Atlanta, GA, July 2004.

[10] A. Rogalski, *Infrared Detectors.* Singapore: Gordon and Breach Science Publishers, 2000.

[11] A. Johnston, “Optoelectronic devices with complex failure modes,” 2000 IEEE Nuclear and Space Radiation Effects Conference Short Course, Reno, NV, 2000.

[12] P. W. Marshall and C. J. Marshall, “Proton effects and test issues for satellite designers,” 1999 IEEE Nuclear and Space Radiation Effects Conference Short Course, Norfolk, VA, July 1999.

[13] A.Rogalski, “HgCdTe infrared detector material: history, status, and outlook,” *Rep. Prog. Phys.*, vol. 68, pp. 2267–2336, 2005.

[14] R. J. Keyes, *Opitcal and Infrared Detectors.* New York: Springer-Verlag, 1980.

[15] J. C. Pickel, A. H. Kalma, G. R. Hopkinson, and C. J. Marshall, “Radiation effects on photonic imagers-a historical perspective,” *IEEE Trans. Nucl. Sci.*, vol. 50, pp. 671–688, 2003.

[16] M. G. Kivelson and C. T. Russel, *Introduction to Space Physics*. Cambridge: Cambridge University Press, 1995.

[17] (2008) Solar physics. [Online]. Available: http://solarscience.msfc.nasa.gov.

[18] M. Xapsos, "Modeling the space radiation environment," 2006 IEEE Nuclear and Space Radiation Effects Conference Short Course, Ponte Vedra Beach, FL, July 2006.

[19] (2008) NOAA satellites and information national geophysical data center. [Online]. Available: http://www.ngdc.noaa.gov/ngdc.html.

[20] (2007) Solar and helispheric observatory website. [Online]. Available: http://sohowww.nascom.nasa.gov.

[21] (2008) NASA's high energy astrophysics science archive research center. [Online]. Available: http://heasarc.gsfc.nasa.gov.

[22] E. J. Daly, J. Lemaire, D. Heynderickx, and D. J. Rodgers, "Problems with models with the radiation belts," *IEEE Trans. Nucl. Sci.*, vol. 43, pp. 403–414, 1996.

[23] J. R. Schwank, "Basic mechanisms of radiation effects in the natural space environment," 1994 IEEE Nuclear and Space Radiation Effects Conference Short Course, Tucson, AZ, July 1994.

[24] J. Barth, "Modeling space radiation environments," 1997 IEEE Nuclear and Space Radiation Effects Conference Short Course, Snowmass Village, CO, July 1997.

[25] E. Petersen, "Single-event analysis and prediction," 1997 IEEE Nuclear and Space Radiation Effects Conference Short Course, Snowmass Village, CO, July 1997.

[26] F. W. Sexton, "Measurements of single event phenomenon in devices and ICs," 1992 IEEE Nuclear and Space Radiation Effects Conference Short Course, New Orleans, LA, July 1992.

[27] (1997) Cosmic ray effects on micro electronics website. [Online]. Available: https://creme96.nrl.navy.mil/.

[28] P. S. Winokur, "Total-dose radiation effects," 1992 IEEE Nuclear and Space Radiation Effects Conference Short Course, New Orleans, LA, July 1992.

[29] L. W. Massengill, "SEU modeling and prediction techniques," 1993 IEEE Nuclear and Space Radiation Effects Conference Short Course, Snowbird, UT, July 1993.

[30] J. C. Pickel, R. A. Reed, R. Ladbury, B. Rauscher, P. W. Marshal, T. M. Jordan, B. Fodness, and G. Gee, "Radiation-induced charge collection in infrared detector arrays," *IEEE Trans. Nucl. Sci.*, vol. 49, pp. 671–688, 2002.

[31] J. R. Janesick, *Scientific Charge-coupled Devices.* SPIE Press, 2001.

[32] C. J. Dale, P. W. Marshall, and E. A. Burke, "Particle-induced spatial dark current fluctuations in focal plane arrays," *IEEE Trans. Nucl. Sci.*, vol. 37, pp. 1784–1791, 1990.

[33] J. R. Srour and R. a. Hartmann, "Enhanced displacement damage effectiveness in irradiated silicon devices," *IEEE Trans. Nucl. Sci.*, vol. 36, pp. 1825–1830, 1989.

[34] J. V. der Spiegel and G. J. Declerck, "Characterization of dark current non-uniformities in charge-coupled devices," *Solid State Electron., volume =.*

[35] J. Ziegler. (2008) Particle interactions with matter. [Online]. Available: www.srim.org.

[36] F. Wrobel, "Fundamentals on radiation-matter interaction," 2005 European Conference on Radiation and Its Effects on Components and Systems, Cap d'Agde, France, Sept. 2005.

[37] R. A. Reed, J. Kinnison, J. C. Pickel, S. Buchner, P. W. Marshall, S. Kniffin, and K. A. LaBel, "Single-event effects ground testing and on-orbit rate prediction methods: the past, present, and future," *IEEE Trans. Nucl. Sci.*, vol. 50, pp. 622–634, 2003.

[38] P. E. Dodd and L. W. Massengill, "Basic mechanisms and modeling of single-event upset in digital microelectronics," *IEEE Trans. Nucl. Sci.*, vol. 50, pp. 583–602, 2003.

[39] L. L. House and L. W. Avery, "The Monte Carlo technique applied to radiative transfer," *J Quant Spectrosc Radiat Transf*, vol. 9, pp. 1579–1591, 1969.

[40] L. W. Avery, L. L. House, and A. Skumanich, "Radiative transport in finite homogeneous cylinders by the Monte Carlo technique," *J. Quant. Spectrosc. Radiat. Transf.*, vol. 9, pp. 519–532, 1969.

[41] A. Razani, "A Monte Carlo method for radiation transport calculations," *J. Nucl. Sci. Technol.*, vol. 9, pp. 551–554, 1972.

[42] R. C. Allen *et al.*, *Computational Science Education Project*, 1993. [Online]. Available: http://www.phy.ornl.gov/csep/.

[43] C. Jacoboni and L. Reggiani, "The Monte Carlo method for the solution of charge transport in semiconductors with applications to covalent materials," *Rev. Mod. Phys.*, vol. 55, pp. 645–705, 1983.

[44] H. Duarte, “Improvement of the Intranuclear Cascade code of Bruyéres-le-Châtel (BRIC) at low intermediate energy,” in *Proceedings of the 10th International Cconference on Nuclear Reaction Mechanisms*, E. Gadioli, Ed., vol. 122, Varenna, June 2003, pp. 607–616.

[45] P. J. McNulty and G. E. Farrell, “Proton-induced nuclear reactions in silicon,” *IEEE Trans. Nucl. Sci.*, vol. 28, pp. 4007–4012, 1981.

[46] C. J. Dale, L. Chen, P. J. McNulty, P. W. Marshall, and E. A. Burke, “A comparison of Monte Carlo and analytic treatmetns of displacement damage in Si microvolumes,” *IEEE Trans. Nucl. Sci.*, vol. 41, pp. 1974–1983, 1994.

[47] J. S. Hendricks *et al.*, *MCNPX Extensions Version 2.5.0*, Los Alamos National Laboratory, 2005.

[48] P. J. McNulty, W. G. Abdel-Kader, and J. M. Bisgrove, “Methods for calculating SEU rates for bipolar and NMOS circuits,” *IEEE Trans. Nucl. Sci.*, vol. 32, pp. 4180–4184, 1985.

[49] I. Kawrakow and D. W. O. Rogers, *The EGSnrc Code System: Monte Carlo Simulation of Eletron and Photon Transport*, Ionizing Radiation Standards National Research Council of Canada, 2003.

[50] G. A. Wright, E. Shuttleworth, M. J. Grimstone, and A. J. Bird, “The status of the general radiation transport code MCBEND,” *Nucl. Instrum. Methods Phys. Res. B*, vol. 213, pp. 162–166, 2004.

[51] M. B. Emmett, “MORSE: present capabilities and future directions,” *Appl. Radiat. Isot.*, vol. 53, pp. 863–866, 2000.

[52] C. Inguimbert, S. Duzellier, R. Ecoffet, and J. Bourrieau, “Proton upset rate simulation by a Monte Carlo method: Importance of the elastic scattering mechanism,” *IEEE Trans. Nucl. Sci.*, vol. 44, pp. 2243–2249, 1997.

[53] K. M. Warren, R. A. Weller, M. H. Mendenhall, R. A. Reed, D. R. Ball, C. L. Howe, B. D. Olson, M. L. Alles, L. W. Massengill, R. D. Schrimpf, N. F. Haddad, S. E. Doyle, D. McMorrow, J. S. Melinger, and W. T. Lotshawand, “The contribution of nuclear reactions to single event upset cross-section measurements in a high-density SEU hardened SRAM technology,” *IEEE Trans. Nucl. Sci.*, vol. 52, pp. 2125–2131, 2005.

[54] A. S. Kobayashi, D. R. Ball, K. M. Warren, R. A. Reed, M. H. Mendenhall, R. D. Schrimpf, and R. A. Weller, “The effect of metallization layers on single event susceptibility,” *IEEE Trans. Nucl. Sci.*, vol. 52, pp. 2189–2193, 2005.

[55] D. R. Ball, K. M. Warren, R. A. Weller, R. A. Reed, A. Kobayashi, J. A. Pellish, M. H. Mendenhall, C. L. Howe, L. W. Massengill, R. D. Schrimpf, and N. F. Haddad, “Simulating nuclear events in a TCAD model of a high-density SEU

hardened SRAM technology," *IEEE Trans. Nucl. Sci.*, vol. 53, pp. 1794–1798, 2006.

[56] C. L. Howe, R. A. Weller, R. A. Reed, M. H. Mendenhall, R. D. Schrimpf, K. M. Warren, D. R. Ball, L. W. Massengill, K. A. LaBel, J. W. Howard, Jr., and N. F. Haddad, "Role of heavy-ion nuclear reactions in determining on-orbit single event error rates," *IEEE Trans. Nucl. Sci.*, vol. 52, pp. 2182–2188, 2005.

[57] M. H. Mendenhall and R. A. Weller, "An algorithm for computing screened Coulomb scattering in Geant4," *Nucl. Instrum. Methods Phys. Res. A*, vol. 227, pp. 420–430, 2005.

[58] *Physics Reference Manual*, Geant4, 2008. [Online]. Available: http://geant4.web.cern.ch/geant4/.

[59] H. Burkhardt, V. M. Grichine, P. Gumplinger, V. N. Ivanchenko, R. P. Kokoulin, M. Maire, and L. Urban, "Geant4 standard electromagnetic package for HEP applications," IEEE Nuclear Science Symposium Conference Record, pp. 1907–1910, Oct. 2004.

[60] "Penelope - a code system for Monte Carlon simulation of electron and photon transport," *Workshop Proceedings Issy-les-Moulineaux*, pp. AEN–NEA, Nov. 2001.

[61] *Geant4 User's Guide for Application Developers*, Geant4, 2008. [Online]. Available: http://geant4.web.cern.ch/geant4/.

[62] S. Agostinelli *et al.*, "Geant4-A simulation toolkit," *Nucl. Instrum. Methods Phys. Res. A*, vol. 506, pp. 250–303, 2003.

[63] (2008) The HDF Group. [Online]. Available: http://www.hdfgroup.org/HDF5/.

[64] I. I. S. E. AG, *User Guides*, 2004.

[65] J.C.Pickel, R.Reed, R.Ladbury, B.Rauscher, P.Marshall, T.Jordan, B.Fodness, and G.Gee, "Modeling radiation-induced transients in the next generation space telescope (NGST)," Mar. 2002.

[66] M. Kessler, J. Steinz, M. Anderegg, J. Clavel, G. Drechsel, P. Estaria, J. Faelker, J. Riedinger, A. Robson, B. Taylor, and S. X. de Ferran, "The infrared space observatory (ISO) mission," *Astron. Astrophys.*, vol. 315, pp. L27–L31, 1996.

[67] M. Kessler, "The infrared space observatory (ISO) mission," *Adv. Space Res.*, vol. 30, pp. 1957–1965, 2002.

[68] A. Claret and H. Dzitko, "Monte-Carlo simulations of cosmic-ray and internal radiation effects on ISOCAM on board ISO," *Expr. Astron.*, vol. 13, pp. 135–152, 2002.

[69] O. Boulade and P. Gallais, "The ISOCAM detectors: an overview," *Expr. Astron.*, vol. 10, pp. 227–239, 2000.

[70] S. Onoda, T. Hirao, J. S. Laird, T. Wakasa, T. Yamakawa, T. Okamoto, Y. Koizumi, and T. Kamiya, "Development of Monte Carlo modeling for proton induced charge in si pin photodiode," *IEEE Trans. Nucl. Sci.*, vol. 51, pp. 2270–2775, 2004.

[71] J. E. Hubbs, M. E. Gramer, D. C. Arrington, G. A. Dole, D. Maestas-Jepson, and S. E. Takeall, "Total ionizing dose and proton radiation characterization of si p-i-n visible hybrid focal plane arrays," *Proc. SPIE*, vol. 5902, pp. 128–142, 2005.

[72] J. Hubbs, "Radiometric and radiation reponse of visible FPAs," NASA Reference Publication, Tech. Rep., Apr. 2007.

[73] (2005) Crocker nuclear laboratory radiation effects facility. [Online]. Available: http://crocker.ucdavis.edu/images/operations/brochure/FacityUpdates2005.pdf.

[74] C. M. Castaneda, "Crocker nuclear laboratory (cnl) radiation effects measurement and test facility," *IEEE Radiation Effects Data Workshop*, pp. 77–81, 2001.

[75] P. W. Marshall, J. E. Hubbs, D. C. Arrington, C. J. Marshall, R. A. Reed, G. Gee, J. C. Pickel, and R. A. Ramos, "Proton-induced transients and charge collection measurements in a LWIR HgCdTe focal plane array," *IEEE Trans. Nucl. Sci.*, vol. 50, pp. 1968–1973, 2003.

[76] F. H. Tenney, "Ideal pulse pileup effects on energy spectra," *Nucl. Instrum. Methods Phys. Res. A*, vol. 219, pp. 165–172, 1984.

[77] H. L. Anderson, *A Physicist's Desk Reference.* New York: AIP, 1989.

[78] C. L. Howe, R. A. Weller, R. A. Reed, B. D. Sierawski, P. W. Marshall, C. J. Marshall, M. H. Mendenhall, R. D. Schrimpf, and J. E. Hubbs, "Distribution of proton-induced transients in silicon focal plane arrays," *IEEE Trans. Nucl. Sci.*, vol. 54, pp. 2444–2449, 2007.

[79] S. F. Fung, *Recent Development in the NASA Trapped Radiation Models.* New York: AGU Geophysical Monograph, 1996, vol. 97.

[80] R. A. Reed, R. A. Weller, M. H. Mendenhall, J. M. Lauenstein, K. M. Warren., J. A. Pellish, R. D. Schrimpf, B. Sierawski, L. W. Massengill, P. E. Dodd, N. F. Haddad, R. K. Lawrence, J. H. Bowman, and R. Conde, "Impact of ion energy and species on single event effects analysis," *IEEE Trans. Nucl. Sci.*, vol. 54, pp. 2312–2321, 2007.

[81] R. A. Weller, Vanderbilt University, Nashville, TN, 2008, personal communication.

[82] K. M. Warren, R. A. Weller, B. D. Sierawski, R. A. Reed, M. H. Mendenhall, R. D. Schrimpf, L. W. Massengill, M. E. Porter, J. D. Wilkinson, K. A. LaBel, and J. H. Adams, "Application of RADSAFE to model the single event upset response of a 0.25 μm CMOS SRAM," *IEEE Trans. Nucl. Sci.*, vol. 54, pp. 898–903, 2007.